



Model optimization and techniques for the simulation of multiphase chemical reactors

Dissertation

zur Erlangung des akademisches Grades

**Doktoringenieur
(Dr.-Ing.)**

von **M.Sc. Luís Guilherme Medeiros de Souza**

geb. am 10. November 1982 in Joaçaba, Brasilien

genehmigt durch die Fakultät für Verfahrens- und Systemtechnik
der Otto-von-Guericke-Universität Magdeburg

Gutachter: Priv.-Doz. Dr.-Ing. Gábor Janiga
Prof. Dr.-Ing. Andreas Seidel-Morgenstern
Prof. Dr. Volker John

Promotionskolloquium am: 12. August 2016

To my family...

Acknowledgements

It has been an amazing time here in Germany. I have gotten so many opportunities and I have met so many great people. I would like to express my gratitude to all of those who have helped me during this period.

Firstly, I would like to thank Prof. Dr.-Ing. Dominique Thévenin for the possibility to take part in so many interesting research projects. He has not only given creative ideas and insight to my work, but also has encouraging me a lot. Many thanks!

My special thanks to Priv.-Doz. Dr.-Ing. Gábor Janiga. His CFD lecture during my Master study motivated me to work in this department. Thanks for helping me to structure my research, specially in the beginning of my Ph.D. work. Thanks also for all the support during the development of this thesis.

I also would like to thank Prof. Dr.-Ing. Andreas Seidel-Morgenstern for the insightful discussions, which have been extremely valuable for my work.

I am grateful to Prof. Dr. Volker John for accepting to take part as reviewer of my thesis and also for all the contributions to my first scientific paper back in 2009.

Some of the results in this thesis would not have been possible without the work of Henning Haida, Erik Temmel, Patrícia Arányi, Ashraf B. Ali, Marvin Henneberg, Hossein Janbazi and Alexandra Bünger. Many thanks for let me use your experimental and simulation results.

Thanks to all my colleges in the department for creating this friendly and productive atmosphere.

Finally, I wish to thank my family in Brazil for all the support and caring.

Abstract

The accurate description of multiphase chemical reactors is essential to improve existing applications and design new configurations. Nevertheless, a detailed simulation of a full multiphase reactor is a complex problem that involves the description of distinct modeling levels. Despite of the increasing computing power and the advances in modeling, there is a need for efficient simulation techniques, robust models and practical coupling methodologies for the simulation of multiscale reactors of industrial interest.

In this thesis, techniques and methodologies that assist the simulation of multiphase chemical reactors have been developed and tested. The main results presented in this work are the following: (i) technique for the reconstruction of distribution from a finite number of moments, (ii) methodology for model parameter optimization using multi-objective optimization and (iii) methodology for the multiscale coupling of multiphase reactors.

Quadrature-based method of moments are commonly used to solve population balance equations (PBEs). With this method only a small number of moments of the underlying distribution are tracked. The developed adaptive reconstruction technique using splines allows to retrieve distributions from a finite set of moments without prior knowledge on the shape of the distribution; only the initial moments and a rough estimation of the domain are needed.

Another tool explored in this work is the multiobjective optimization, which has been used for the optimization of model parameters. It is a methodology that has not been well explored in this realm. In many practical situations, however, multiobjective optimization may deliver more robust and general applicable set of parameters compared with single objective optimization. This methodology has been applied for the optimization of the realizable $k - \epsilon$ turbulence model and for the optimization of kinetic and model parameters of a catalytic chemical reaction network.

Finally, a batch crystallization reactor has been simulated. The distinct modeling levels, e.g., fluid dynamics, population balance, growth kinetics, are coupled within the Euler-Euler framework. Nevertheless, the brute-force 3-D simulation leads to unaffordable computing time. Motivated by that, a methodology combining 3-D and 0-D simulation has been elaborated. The developed methodology considers the mixing and the crystal growth separately but uses the local information of the flow for a detailed description of the crystal growth.

Kurzfassung

Die genaue Beschreibung von mehrphasigen, chemischen Reaktoren ist von wesentlicher Bedeutung für die Optimierung von bestehenden Anwendungen und für den Entwurf von neuen Konfigurationen. Dennoch ist eine detaillierte Simulation des gesamten Reaktors ein komplexes Problem, das die Beschreibung verschiedener Modellierungsebenen beinhaltet. Trotz der zunehmenden Rechenleistung und der Fortschritte in der Modellierung besteht weiterhin ein Bedarf an effizienten Simulationstechniken, robusten Modellen und praxistauglichen Kopplungsmethoden für die Simulation von industriellen Reaktoren.

In dieser Arbeit wurden Techniken und Methoden entwickelt und getestet, die die Simulationen von mehrphasigen, chemischen Reaktoren unterstützen. Die wichtigsten Ergebnisse in dieser Arbeit betreffen folgende Gebiete: (i) Rekonstruktion der Verteilung aus einer finiten Anzahl von Momenten, (ii) Anpassung der Modellparameter mit Mehrzielfunktion Optimierung und (iii) mehrskalige Kopplung von mehrphasigen Reaktoren.

Quadratur-basierte Momente Methoden werden häufig verwendet, um Populationsbilanzgleichungen (PBs) zu lösen. Mit dieser Methode werden nur eine kleine Anzahl von Momenten der zugrundeliegenden Verteilung verfolgt. Die entwickelte adaptive Rekonstruktionstechnik erlaubt es, mittels Splines, Verteilungen aus einer endlichen Menge von Momenten abzurufen, ohne vorherige Kenntnisse über die Form der Verteilung. Lediglich die anfänglichen Momente und eine grobe Schätzung des Wertbereiches werden benötigt.

Ein weiteres Werkzeug, das in dieser Arbeit untersucht wurde, ist die Optimierung von Mehrzielfunktionen. Dies wurde für einzelne Modellparameter angewendet. Es handelt sich dabei um eine Methode, die in diesem Bereich noch nicht gut untersucht wurde. In vielen praktischen Anwendungsfällen liefert die Mehrzielfunktion Optimierung jedoch robustere und besser verallgemeinerbare Sätze von Parametern im Vergleich zu der Einzielfunktion Optimierung. Diese Methodik wurde für die Optimierung des *realizable* $k - \epsilon$ Turbulenzmodells und für die Optimierung der Modell- und Kinetikparameter eines katalytischen, chemischen Reaktionsnetzwerkes angewandt.

Schließlich wurde ein diskontinuierlicher Kristallisationsreaktor simuliert. Die unterschiedlichen Modellierungsebenen (z.B. Fluidodynamik, Populationsbilanzgleichungen, Wachstumskinetiken) wurden im Euler-Euler-Rahmen gekoppelt. Dennoch führten reine 3-D-Simulationen zu unerschwinglichen Rechenzeiten. Dadurch motiviert, wurde eine Methodik erarbeitet, die die 3-D und die 0-D-Simulation

kombiniert. Die entwickelte Methodik, betrachtet das Mischen und das Kristallwachstum separat, nutzt aber die lokalen Informationen der Strömung für eine detaillierte Beschreibung des Kristallwachstums.

Contents

1	Introduction	1
1.1	Thesis outline	2
2	Methods to simulate polydisperse multiphase flows	5
2.1	Introduction	5
2.2	Eulerian multiphase model	6
2.3	Population balance equation and quadrature-based method of moments	8
2.3.1	Population balance equation (PBE)	8
2.3.2	Quadrature-based method of moments	9
2.3.3	CFD-PBE coupling	11
2.3.4	Solution algorithm for CFD-PBE (QMOM)	11
2.4	Reconstruction of a distribution from a finite set of moments	12
2.4.1	Techniques to reconstruct a distribution from a finite set of its moments	13
2.4.2	The adaptive spline-based reconstruction algorithm	15
2.4.3	Results and discussion	19
2.4.4	Conclusions	25
2.5	Summary	26
3	Methodology for model parameter optimization using multi-objective genetic algorithm	29
3.1	Introduction	29
3.2	Multi-objective optimization	30
3.3	Basic concepts	31
3.3.1	Pareto optimality	31
3.3.2	Decision making	32
3.4	Coupling simulation software with optimization algorithm	33
3.5	Summary	35

4	Model optimization for turbulent flows	37
4.1	Introduction	37
4.2	The closure problem	39
4.3	Two-equation RANS models	39
4.4	The realizable $k - \epsilon$ turbulence model	41
4.4.1	Determination of the model parameters	43
4.4.2	Overall values in literature	47
4.5	Selected test cases	48
4.5.1	Channel flow	48
4.5.2	Backward-facing step	49
4.5.3	Free jet	50
4.5.4	Flow over periodic hill	51
4.6	Details of the CFD simulations	52
4.7	Multi-objective optimization	53
4.8	Independent configurations	54
4.8.1	Savonius turbine	54
4.8.2	Airfoil wake	55
4.8.3	Flow around building	56
4.8.4	Square duct with 180° bend	57
4.9	Results and discussion	58
4.10	Conclusions	65
5	Model optimization for chemical reactions using global model structure	67
5.1	Introduction	67
5.2	Generalized kinetic model for heterogeneous catalytic reactions	69
5.3	System under investigation	71
5.3.1	Modeling	72
5.4	Reparametrization	73
5.5	Optimization methodology	73
5.6	Results and discussions	76
5.7	Conclusions	82
6	Simulation of a multiphase chemical reactor	83
6.1	Crystallization: a multiscale problem	83
6.2	Crystal growth kinetics and interplay with fluid dynamics	85
6.2.1	Slip velocity and the diffusive mass transfer coefficient (k_d)	86
6.3	Studied system: batch cooling crystallization reactor	87
6.3.1	Experimental details	87

6.3.2	Physical properties and measured data	88
6.4	Reactor geometry	90
6.5	Reactor mesh and boundary conditions	91
6.6	CFD simulation: hydrodynamics (single phase)	92
6.7	QMOM (0-D approach)	93
6.7.1	Initial distribution	93
6.7.2	Modeling	95
6.7.3	Results	95
6.8	CFD-QMOM (3-D brute-force approach)	96
6.8.1	CFD-QMOM (mixing dynamics)	96
6.8.2	Models used in ANSYS Fluent	98
6.8.3	Results	99
6.9	Coupled 3-D/0-D simulation	100
6.9.1	Methodology	101
6.9.2	Mixing time	101
6.9.3	Results	103
6.10	Conclusions	113
7	Conclusions and outlook	115
A	Appendix	119
A.1	Two-equation RANS models	119
A.2	Reactor volume variation	120
	References	123

Nomenclature

A list with the most relevant symbols is included here. In order to follow standard notations, a few symbols may represent more than one quantity.

Latin symbols

d_{10}	median mean diameter	[m]
d_{32}	Sauter mean diameter	[m]
D	diffusion coefficient	[m ⁻² s]
E_A	activation energy	[kJ/mol]
\mathbf{g}	gravity	[m s ⁻²]
G	particle growth rate	[m s ⁻¹]
h	characteristic length	[m]
k_d	diffusive mass transfer coefficient	[m s ⁻¹]
k_s	surface integration coefficient	[m s ⁻¹]
k_V	volume shape factor	[-]
L	abscissas of the quadrature approximation	[m]
$n(\xi, \mathbf{x}, t)$	number-based density function	[s ⁻¹]
n_p	number of phases	[-]
N	number of quadrature points	[-]
N_{obj}	number of objective functions	[-]
N_{param}	number of parameters	[-]
p	pressure	[Pa]
Re	Reynolds number	[-]
Sc	Schmidt number	[-]
Sh	Sherwood number	[-]
S_k	source term	[-]
t	time	[s]
T	temperature	[K]
r_j	reaction rate	[mol s ⁻¹]
u_i	instantaneous velocity	[m s ⁻¹]

u'_i	fluctuation velocity	[m s ⁻¹]
U_i	mean velocity	[m s ⁻¹]
\mathbf{u}_q	mean velocity vector of the q th phase	[m s ⁻¹]
u_{slip}	slip velocity	[m s ⁻¹]
x_i	space coordinate	[m]

Greek symbols

α	volume fraction	[-]
ϵ	turbulent dissipation rate	[m ² s ⁻³]
μ	dynamic viscosity	[kg m ⁻¹ s ⁻¹]
μ_k	k th moment of a distribution	
ν	kinematic viscosity	[m ² s ⁻¹]
ν_T	turbulent eddy viscosity	[m ² s ⁻¹]
ξ	internal coordinate vector	
ρ	density	[kg m ⁻³]
τ	Reynolds stress tensor	[Pa]
ω	weight of the quadrature approximation	[-]

Abbreviations

CFD	Computational Fluid Dynamics
DQMOM	Direct Quadrature Method of Moments
GA	Genetic Algorithm
NDF	Number-based Density Function
NSGA-II	Non-dominated Sorting Genetic Algorithm-2
PBE	Population Balance Equation
PSD	Particle Size Distribution
QBMM	Quadrature-based Method of Moments
QMOM	Quadrature Method of Moments
RANS	Reynolds-averaged Navier–Stokes
UDF	User-defined function

Chapter 1

Introduction

A chemical reactor is a very complex system where phenomena with distinct time and length scales coexist and influence each other. The accurate description of this complex system requires different modeling levels. For instance, the simulation of a crystallization reactor involves the fluid dynamics modeling, the particle properties evolution modeling and the crystallization kinetics modeling (see Fig. 1.1). For the description of each of these modeling levels, specialized submodels are required.

There is a need for better models and techniques that support the simulation of complex chemical reactors. This thesis tackles some of these issues, providing methodologies and techniques that assist the simulation of chemical reactors and testing it in applications of industrial interest. Considering the modeling levels involved in the description of chemical reactors, the methodologies and techniques developed in this work have the following applications:

- Fluid dynamics modeling: the accurate prediction of turbulent flows is a fundamental issue to improve existing applications and develop new configurations. Numerical simulations based on Reynolds Averaged Navier-Stokes (RANS) models are still widely used today for practical engineering problems. RANS models have been usually calibrated based on simple flows but are applied in far more complex geometry. For a particular flow, it is known that the prediction can usually be improved by adjusting the model parameters. A methodology for the determination of optimal and generally applicable parameters would be a valuable tool.
- Particle properties evolution modeling: moment-based quadrature method of moments are a popular approach to solve the population balance equations (PBE). Nevertheless, with such methods only the moments are tracked and no information about the shape of the distribution can be derived. A technique that supports the reconstruction of distributions considering only a finite set

of moments would find applications in many fields.

- Kinetics modeling: in many practical situations a single set of parameters should fit a model to different experimental conditions or fit different models simultaneously. In such cases, a multi-objective optimization would be a far more valuable tool for the determination of optimal model parameters.

Within the framework of the computational fluid dynamics (CFD) it is possible to use specialized models at distinct modeling levels and exchange information between the different scales. For instance, in crystallization the local conditions of the flow influences the evolution of the particles properties which in turn affects the spatial distribution of the particles in the reactor, creating a complex network. Nevertheless, the simulation of phenomena with very different temporal and spatial scales leads to further complexities. Therefore, a methodology to track the particle properties evolution while considering a detailed fluid dynamics description is needed.

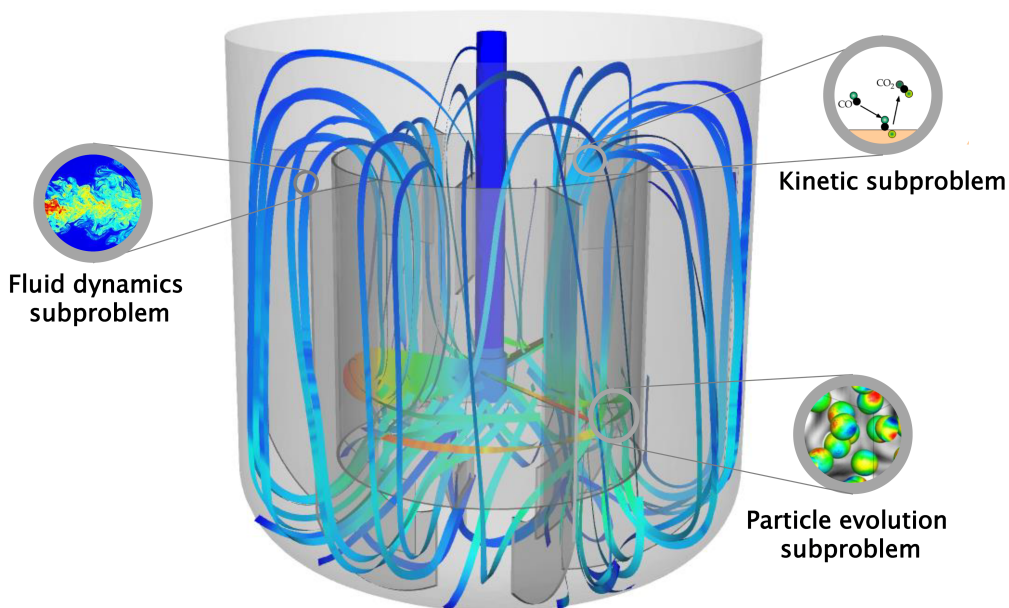


Figure 1.1: Multiphase chemical reactor, showing the distinct modeling levels.

1.1 Thesis outline

Distinct topics have been addressed in this thesis and some chapters can be seen as a topic on their own. A mind map of the topics addressed in this thesis is showed in Fig. 1.2.

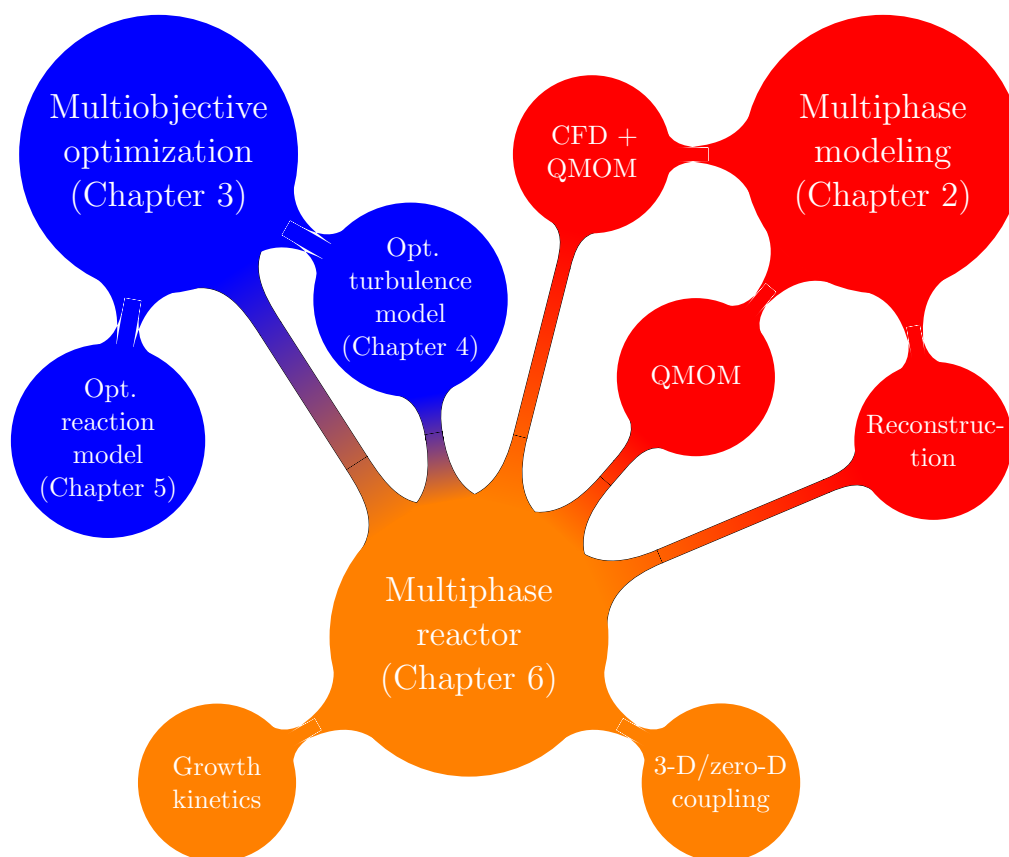


Figure 1.2: Mind map of the topics addressed in this thesis.

The thesis is structured as follows:

Chapter 2 (Methods to simulate polydisperse multiphase flows): describes the methodology for the simulation of multiphase flows using the Euler-Euler multifluid framework. The quadrature method of moments (QMOM), as well as its coupling with CFD is discussed. Finally, a novel technique for the reconstruction of distributions based on a finite set of moments is discussed.

Chapter 3 (Methodology for model parameter optimization using multi-objective genetic algorithm): describes a methodology for the optimization of model parameters using multi-objective optimization. The advantages of multi-objective optimization, basic concepts and the coupling between simulation software and optimization algorithm are discussed. The presented methodology is employed for the model optimization of a turbulence RANS model (Chapter 4) and for the model optimization of a chemical catalytic reaction network (Chapter 5).

Chapter 4 (Model Optimization for Turbulent Flows): describes the optimization of the realizable $k - \epsilon$ turbulence model parameters using multi-objective optimization. The optimized model is also tested in four independent configurations.

Chapter 5 (Model Optimization for Chemical Reactions using Global Model Structure): describes the optimization of mechanism and parameters of catalytic reactions

using multi-objective optimization

Chapter 6 (Simulation of a Multiphase Chemical Reactor): investigates a full multiphase crystallization reactor involving distinct modeling levels. The methodology to simulate polydisperse multiphase flows described in Chapter 2, as well as the developed distribution reconstruction technique are applied. Furthermore, the optimized RANS turbulence model (see Chapter 3 and Chapter 4) is employed. Details on the growth kinetics are elaborated in this chapter. A methodology to track the particle properties evolution while considering a detailed fluid dynamics description is also discussed in this chapter.

Chapter 7 (Conclusions and Outlook): finalizes the thesis with a discussion on the topics developed and discusses perspectives to further works.

Chapter 2

Methods to simulate polydisperse multiphase flows

2.1 Introduction

Polydisperse multiphase flows are characterized by a disperse phase distributed as small discrete elements in a continuous phase. Such flows are present in many environmental and industrial applications, being often realized in chemical reactors (e.g., crystallizers, fluidized beds, emulsions).

The discrete elements in the disperse phase (or phases) can be solid particles, drops or bubbles — note that the term “particles” is used in this work as a general reference to solid particles, drops or bubbles. These particles are mostly not identical, they may differ due to several properties, e.g., size, shape, temperature, composition, leading to polydisperse multiphase flows.

In multiphase flows, particle-particle interactions and also interactions with the continuous phase occur. A modeling framework that accurately describe polydisperse multiphase flows should consider the modeling of the multiphase flow and the evolution of the properties of the dispersed phase.

In practical engineering applications, a microscopic detailed description of the interfaces between the disperse and the continuous phase is not required. Thus, the macroscopic continuum description provided by the Eulerian multiphase model is suitable for most practical cases. In the Eulerian multiphase model, averaged mass and momentum equations are derived for each phase (more details are given in Section 2.2). The averaging procedure introduces interphase exchange terms, which need to be modeled bringing the microscale and mesoscale physics into account. Nevertheless, particle-particle interactions are not considered in the Eulerian multiphase model. A detailed description on the derivation of the Eulerian multiphase model can be found in [Ishii and Hibiki \(2006\)](#).

The models that describe the disperse phase are based on the solution of the population balance equations (PBE), see [Ramkrishna \(2000\)](#). The PBE describes in terms of number-based density function (NDF) information about the properties of the disperse phase. For instance, the evolution of particle size in crystallization processes accounting for all the physical phenomena that may occur, e.g., nucleation, growth, aggregation, breakage. As it is discussed in Chapter 6, the description of the particle size distribution (PSD) in crystallization processes is fundamental to determine the quality of the process. In order to describe spatial gradients and account for the influence of local conditions of the flow in the properties of the particles, the CFD model and the PBE should be coupled. However, classical numerical methods to solve the PBE, such as Monte Carlo methods ([Gillespie \(1972\)](#); [Shah et al. \(1977\)](#)) and sectional or class methods ([Geldard and Seinfeld \(1980\)](#); [Hounslow et al. \(1988\)](#)) are computationally very intensive to be coupled with CFD for solving engineering problems of practical interest.

Quadrature-based method of moments (QBMM) has gained popularity as an efficient technique to solve population balance equations. Following the quadrature method of moments (QMOM) of [McGraw \(1997\)](#), numerous similar methods have been published, e.g., direct quadrature method of moments (DQMOM), conditional quadrature method of moments (CQMOM), sectional quadrature method of moments (SQMOM), adaptive direct quadrature method of moments (ADQMOM).

In quadrature-based methods, the PBE problem is written in terms of the moments of density functions and it is approximated by a set of Dirac delta functions. The quadrature method of moments (QMOM) ([McGraw \(1997\)](#)) is employed in this work; QMOM and its coupling with CFD is explained with details in Section 2.3.3.

The main drawback of QBMM, comparing with classical numerical methods to solve the PBE, is that the quadrature method does not preserve the shape of the number-based density function (NDF); nevertheless, the NDF can be approximated based on the information of the first moments. A review on techniques to reconstruct distributions from a finite set of its moments are discussed with details in Section 2.4, along with a novel method introduced by the author in [de Souza et al. \(2010\)](#).

2.2 Eulerian multiphase model

The Eulerian multiphase model describes the flow as an interpenetrating continua. It is defined by the averaged conservation equations for mass and momentum; these averaged equations are solved for each phase at every point in space and time during the simulation. The Eulerian multifluid model implemented in the commercial software ANSYS Fluent 14.0 is used in this work. The formulation of the model

includes the concept of volume fraction of phase q , given by:

$$\alpha_q = \frac{V_q}{\sum_{q=1}^{n_p} V_q}, \text{ s.t. } \sum_{q=1}^{n_p} \alpha_q = 1 \quad (2.1)$$

with V_q being the volume of phase q in each grid cell. The continuous phase is referred by the index $q = 0$ and the disperse phases are denoted by $q = 1, \dots, n_p$.

The averaged conservation equations of mass and momentum read as follows:

$$\underbrace{\frac{\partial \alpha_q \rho_q}{\partial t}}_{\text{transient}} + \underbrace{\nabla \cdot \alpha_q \rho_q u_q}_{\text{convective}} = \underbrace{\sum_{p=1}^{n_p} \dot{m}_{pq}}_{\substack{\text{interphase} \\ \text{mass} \\ \text{exchange}}} \quad (2.2)$$

and

$$\underbrace{\frac{\partial \alpha_q \rho_q u_q}{\partial t}}_{\text{transient}} + \underbrace{\nabla \cdot \alpha_q \rho_q u_q u_q}_{\text{convective}} = \underbrace{-\alpha_q \nabla p}_{\text{pressure}} + \underbrace{\alpha_q \rho_q g}_{\text{body}} - \underbrace{\nabla \cdot (\bar{\bar{\tau}}_q)}_{\text{shear}} + \sum_{p=1}^{n_p} \left(\underbrace{R_{pq}}_{\substack{\text{interphase} \\ \text{force} \\ \text{exchange}}} + \underbrace{\dot{m}_{pq} u_q}_{\substack{\text{interphase} \\ \text{force} \\ \text{exchange}}} \right) + \alpha_q \rho_q \underbrace{(F_{lift,q} + F_{vm,q})}_{\substack{\text{lift and} \\ \text{virtual mass force}}} \quad (2.3)$$

where ρ_q and u_q represents the density and velocity of phase q , respectively. The term \dot{m}_{pq} describes the mass exchange between phase q and the other phases p . In Eq. (2.3), $\bar{\bar{\tau}}_q$ is the stress-strain tensor. The pressure field p is assumed to be the same for all the phases.

The Eq. (2.3) must be closed with appropriate expressions for the interphase force R_{pq} , with $R_{pq} = -R_{qp}$ and $R_{qq} = 0$. In ANSYS Fluent 14.0 the interphase momentum exchange is expressed as:

$$\sum_{p=1}^{n_p} R_{pq} = \sum_{p=1}^{n_p} K_{pq} (u_p - u_q) \quad (2.4)$$

where K_{pq} ($= K_{qp}$) is the interphase momentum exchange coefficient.

The momentum exchange between the phases is based on the value of the exchange coefficient K_{pq} , which can be written in the following general form:

$$K_{pq} = \frac{\alpha_q \alpha_p \rho_p f}{\tau_p} \quad (2.5)$$

where f is the drag function, defined differently for the different exchange coefficient models and τ_p , the ‘‘particulate relaxation time’’, is defined as

$$\tau_p = \frac{\rho_p d_p^2}{18\mu_q} \quad (2.6)$$

where d_p is the characteristic diameter of the disperse phase p .

The well-established drag model of Schiller and Naumann is employed in this work, see [Schiller and Naumann \(1935\)](#):

$$f = \frac{C_D \text{Re}}{24} \quad (2.7)$$

where

$$C_D = \begin{cases} 24(1 + 0.15 \text{Re}^{0.687})/\text{Re} & \text{Re} \leq 1000 \\ 0.44 & \text{Re} > 1000 \end{cases} \quad (2.8)$$

and Re is the Reynolds number calculated based on the relative velocities between the phases.

2.3 Population balance equation and quadrature-based method of moments

2.3.1 Population balance equation (PBE)

The evolution of the properties of the disperse phase is obtained using population balance equations (PBE). The PBE describes in terms of number-based density function (NDF) information about the properties of the dispersed phase. The NDF $n(\xi, x, t)$ is a function of internal and external coordinates. The internal coordinates ξ refer to intrinsic properties of the disperse phase, e.g., particle size, surface, volume. The external coordinates refer to the spatial location x and time t . The PBE can be formulated as a transport equation of the NDF, as given by Eq. (2.9):

$$\frac{\partial n(\xi, x, t)}{\partial t} + \frac{\partial u_i n(\xi, x, t)}{\partial x_i} + \frac{\partial \dot{\xi} n(\xi, x, t)}{\partial \xi} = S_\xi \quad (2.9)$$

The PBE thus contains a transient term; a convection term, with u_i being the velocity vector of the particulate system; a term that accounts for continuous changes (e.g., growth), with $\dot{\xi}$ being the continuous rate of change of the internal coordinate ξ ; and a discontinuous jump function S_ξ (e.g., breakage, aggregation). An additional diffusive-flux should be added in the cases of very small particles (less than one micron) to account for the Brownian motion.

In this work only univariate cases are considered, with $\xi = L$ referring to the particle length. It is also useful to define here $\dot{\xi} = G_L$ as the continuous rate of

change of particle length.

2.3.2 Quadrature-based method of moments

Before we discuss with further details about quadrature-based method of moments, let us derive an integral quantity for the NDF known as moments, as well as their transport equations.

The definition of the k -th moment $\mu_k(\xi)$ of the function $n(\xi, x, t)$ is given by:

$$\mu_k(\xi) = \int_0^\infty \xi^k n(\xi, x, t) d\xi, \quad k = 0, 1, 2, \dots \quad (2.10)$$

Applying the moment transformation, Eq. (2.16) to Eq. (2.9), the moment-transport equation is obtained:

$$\frac{\partial \mu_{L,k}}{\partial t} + \frac{\partial u_i \mu_{L,k}}{\partial x_i} = k G_{k-1} \mu_{k-1} + S_k \quad (2.11)$$

where the particle-growth rate can be defined as:

$$G_{L,k} = \frac{\int_0^\infty G_L n_L L^k dL}{\int_0^\infty n_L(L) L^k dL} \quad (2.12)$$

and applying moment transformation to the source term S_k gives:

$$S_k = \int_0^\infty S_L L^k dL \quad (2.13)$$

Note that Eq. (2.11) is closed only in very particular cases, for instance, when the particle-growth rate (G_L) is size-independent. In most applications, an accurate description would require more complex kernels (e.g., size-dependent particle-growth rate); in this case the moment-transport equation of order k would involve moments of order higher than k , creating a closure problem.

A solution for the closure is obtained approximating the NDF by an N -point Gaussian quadrature as given by the following equation:

$$n(\xi, x, t) \approx \sum_{q=1}^N \omega_q(x, t) \xi(x, t) \quad (2.14)$$

where N is the number of delta functions, $\omega_q(x, t)$ and $\xi(x, t)$ correspond to the quadrature weights and the abscissas, respectively. Usually, just a few number of moments need to be tracked. In most cases 4 to 6 moments are sufficient to estimate physical properties of interest and get a good approximation of the shape of the distribution, as illustrated in Fig. (2.1). From the quadrature theory it is implied that if $2N$ moments are given, the calculated N -point quadrature (N -weights and

N -abscissas) delivers the exact moments up to degree $2N - 1$ (first $2N$ moments).

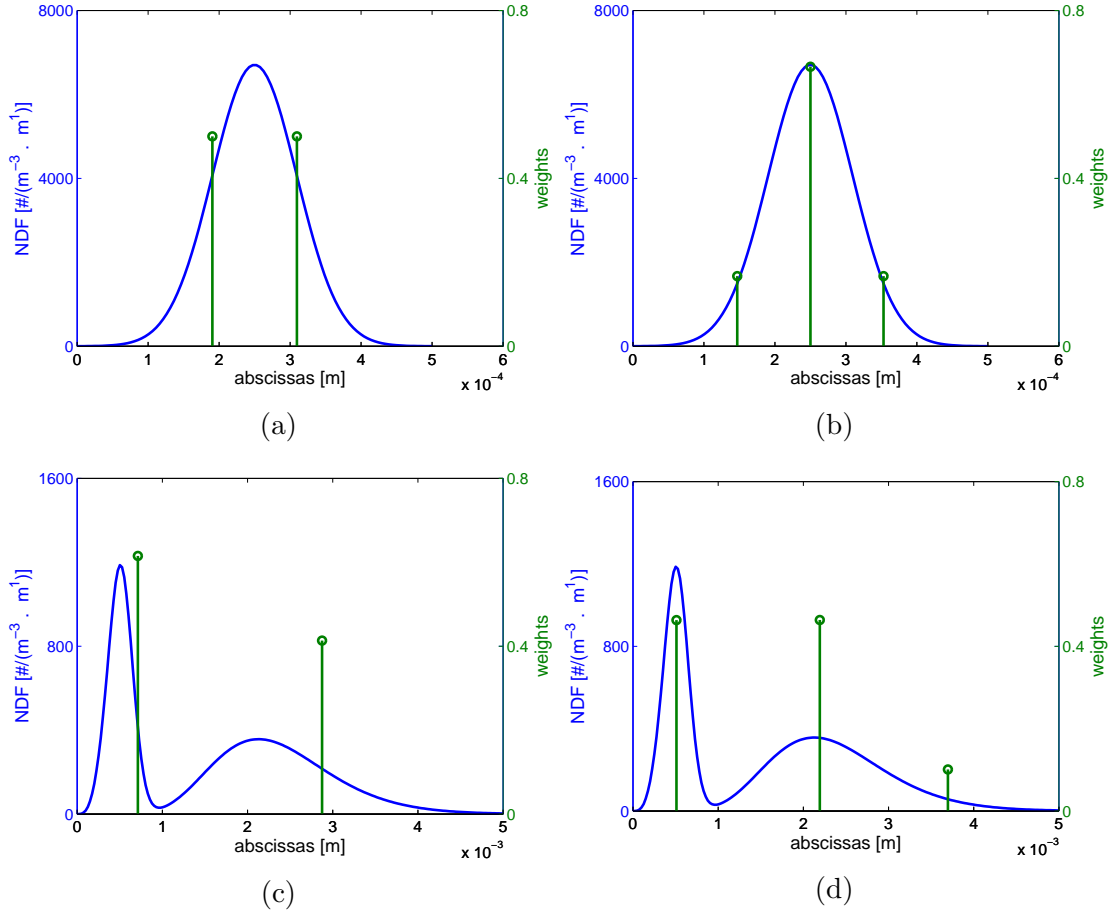


Figure 2.1: PDF with respective weights and abscissa (a) Gauss distribution, 2-point quadrature (b) Gauss distribution, 3-point quadrature (c) Two-peak distribution, 2-point quadrature (d) Two-peak distribution, 3-point quadrature.

There are several algorithm that can be used for the calculation of weights and abscissas; as listed by [Thein \(2012\)](#) the product-difference algorithm (PDA) ([Gordon \(1968\)](#)), the long quotient-modified difference algorithm ([Wheeler \(1974\)](#)), Golub-Welsch algorithm ([Golub and Welsch \(1969\)](#)) and the Newton method. [McGraw \(1997\)](#) suggested the PDA as a suitable moment-inversion algorithm to be used with QMOM. However, [Marchisio and Fox \(2013\)](#) pointed that the Wheeler is more stable when calculating high-order quadrature approximations comparing with the PD algorithm and it also has the advantage to be able to calculate weights and abscissa for distribution with zero mean (a case where the PDA algorithm is known to fail).

The Gaussian quadrature is the core of quadrature-based method of moments, firstly used in the quadrature method of moments (QMOM) introduced by [McGraw \(1997\)](#). Along with the QMOM, the direct quadrature method of moments (DQMOM) ([Marchisio and Fox \(2005\)](#)) is the most prominent and well tested quadrature-

based method. QMOM is used in this work and its coupling with CFD is discussed in more detail in the next subsection.

2.3.3 CFD-PBE coupling

The coupling between the CFD code and the PBE (QMOM) solution is accomplished by relating the results of QMOM with the Eulerian multifluid model. An important result from QMOM is the characteristic Sauter mean diameter ($d_{32} = \mu_3/\mu_2$), which is used in the multifluid model for the calculation of interfacial properties (e.g., drag force).

Another important result from QMOM is the third-order moment, which is related to the volume fraction occupied by the disperse phase as given in Eq. (2.15):

$$\alpha_{disperse} = k_V \sum_{q=1}^N w_q L_q^3 \quad (2.15)$$

where k_V is the volumetric shape factor (for spherical particles $k_V = \frac{\pi}{6}$).

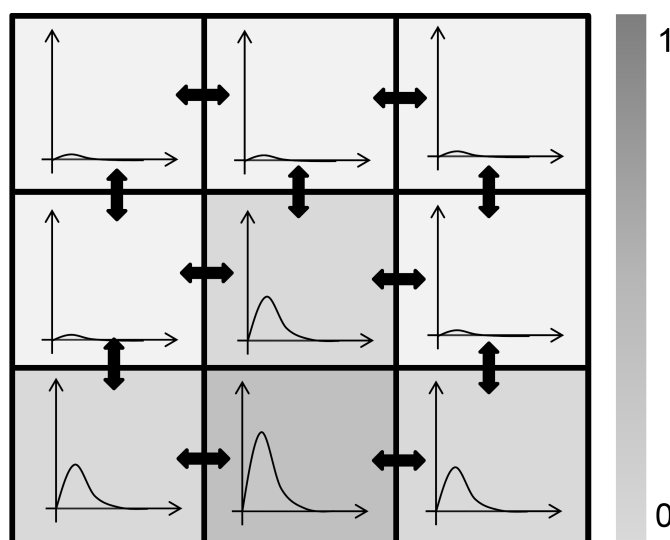


Figure 2.2: CFD-PBE scheme.

The scheme in Fig. 2.2 shows that at each grid cell there is a volume fraction of the disperse phase, which is correlated to a certain distribution. These distributions are transported in the domain with the velocities calculated by the multifluid model. In the current QMOM implementation all the particles share the same velocity field.

2.3.4 Solution algorithm for CFD-PBE (QMOM)

The built-in implementation of QMOM in the commercial software ANSYS Fluent 14.0 is used in this work. The algorithm for the solution of QMOM-multifluid

(two-fluid) is described in the following sequence of steps:

1. Input of initial values: moments, volume fraction of the disperse phase
2. Solution of the multifluid equations, using d_{32} obtained from the moments
3. Solution of the moment-inversion algorithm PDA to generate QMOM values: weights and abscissas
4. Evaluation of source terms S_k and growth rate G_k .
5. Solution of the moment transport equations, using velocity field obtained from the multifluid model
6. Loop over steps 2 to 5 for each time step

2.4 Reconstruction of a distribution from a finite set of moments

This section is written based on the following paper:

L. G. M. de Souza, G. Janiga, V. John, D. Thevenin. Reconstruction of a distribution from a finite number of moments with an adaptive spline-based algorithm, (2010). *Chemical Engineering Science* (65), 269-277.

Moment-based methods to solve population balance equation directly deliver information about the moments of a distribution, nevertheless, in many cases it would be useful to have information about the shape of the underlying distribution. In fact, the problem of reconstructing a scalar-valued function $f(t, \xi)$ from a finite number of its moments, the so-called “finite moment problem”, arises in many scientific and technical applications, e.g., image processing, magnetic imaging, molecular physics or chemical engineering.

The i -th moment $\mu_k(t)$ of the function $f(t, \xi) : [0, \infty) \rightarrow \mathbb{R}$ depending on time and on a one-dimensional, so-called internal coordinate ξ (typically, a length scale) is classically defined by

$$\mu_k(t) = \int_0^\infty \xi^k f(t, \xi) d\xi, \quad k = 0, 1, 2, \dots \quad (2.16)$$

Since a majority of practical applications still only consider mono-variate problems at present, the developed formulation will be restricted to such cases, involving a single internal coordinate (ξ).

From the mathematical point of view, the finite moment problem is a severely ill-posed problem. It has been studied in the mathematical literature almost exclusively from the theoretical point of view (see [John et al. \(2007\)](#) for a review of the most important results). In principle, there is no unique solution for this problem and all moments up to infinity should be known to reconstruct the function.

Nevertheless, there are usually constraints on the domain and on the range of $f(t, \xi)$ due to the underlying physics of the application. A typical example is the reconstruction of Particle Size Distributions (PSD) when considering particulate processes like crystallization, precipitation, etc. The particle size (ξ coordinate) is always positive, and there is always a maximal possible size, at most the reactor size, usually even much smaller. Thus, the domain spanned in the ξ -direction by $f(t, \xi)$ is only an interval within the positive real numbers. Furthermore, a PSD should have only non-negative values, hence the range of $f(t, \xi)$ is only a subset of the non-negative real numbers. Even if these limitations sound trivial from an engineering point of view, they are indeed sufficient from a mathematical point of view to simplify tremendously the complexity of the finite moment problem as recognized also for instance by [Strumendo and Arastoopour \(2008\)](#).

Usually, the moments μ_k associated with the distribution are determined using numerical simulations or advanced experimental techniques. Note, however, that corresponding measurements are extremely difficult, in particular if a high accuracy is required, as documented for example in [Allen \(1997\)](#). As a consequence, only very few moments are usually determined experimentally, mostly in an indirect manner. In practice, only the mean particle size and the particle number concentration can be measured with a relatively high accuracy, even if some set-ups deliver an estimation of the complete PSD (e.g., [Baldyga and Orciuch \(2001\)](#); [Marchisio et al. \(2002\)](#)). This demonstrates the importance of a robust reconstruction method that is able to deliver a good approximation of the underlying distribution with only limited information input.

The situation is not quite as difficult when the moments are determined from numerical simulations. Indeed, very popular numerical techniques like Method of Moments (MOM), Quadrature Method of Moments (QMOM) and Direct Quadrature Method of Moments (DQMOM) directly deliver the moment values. In principle, it is possible to consider as many moments as the user wishes. But the cost of the numerical simulation of course increases rapidly when considering more moments. Furthermore, the mathematical system becomes very badly conditioned for higher-order moments. As a consequence, results found in recent publications deliver a larger but still limited number of moments. For instance, two ([Schwarzer et al. \(2006\)](#)), three ([Diemer and Olson \(2002\)](#)), four ([Wei et al. \(2001\)](#)), five ([Öncül et al.](#)

(2009)) or even for test purposes up to eight moments (Fan et al. (2004)) have been considered for coupled simulations involving particles in a turbulent flow.

2.4.1 Techniques to reconstruct a distribution from a finite set of its moments

For practical engineering purposes, the usual method for reconstructing a function from a small number of its moments is based on an a priori knowledge of the solution. Using this information (e.g., a Gauss shape, or a Poisson distribution), a strong ansatz is made for the shape of $f(t, \xi)$ and the known moments are just used to fit parameters in this ansatz. This fitting is a fast and very easy computation. Nevertheless, this approach is restricted to functions with simple shapes. Even more troublesome is the fact that you need in principle to know the solution before you can get it back, which is obviously not very satisfactory in general (see John et al. (2007) for a more detailed discussion of the advantages and drawbacks of this approach). A direct reconstruction is only possible if the number of known moments is equal to the number of parameters in the ansatz. As an additional difficulty, the shape of the function needed to reconstruct is often time-dependent in practical applications, $f(t, \xi)$. It is then not clear if the presumed shape is suitable for all times.

One very known method to reconstruct distributions from a finite set of moments is the maximum entropy method (MEM). The MEM provides, indeed, an elegant means to solve the finite moment problem. Although a considerable amount of information on this method can be found in literature, the MEM has been rarely applied in the context of chemical engineering to reconstruct PSD.

In order to compute a reconstruction, MEM starts from a so-called prior distribution chosen by the user and applies a finite number of explicit constraints. As a consequence, the shape of the reconstruction is not completely prescribed, but the results still depend on the choice of the prior distribution. Theoretically, as the number of available moments increases, the results of MEM should become more and more independent from the prior distribution. Nevertheless, the limited number of moments usually tracked in moment-based methods may not be enough for a satisfactory reconstruction using MEM.

Further possible techniques to reconstruct a distribution from a finite set of moments include also discrete methods based on a time-dependent update of the distribution (e.g., Giaya and Thompson (2004)). Basically, in this method the form of the PSD can be recovered using information about the growth and nucleation time trajectories. Obviously, the method requests a number of assumptions and can only be applied considering a very simple growth and nucleation kinetics.

In [John et al. \(2007\)](#), a reconstruction approach was presented, which does not require any information on the shape to be reconstructed nor on the spatial extent (ξ coordinate) of the function $f(t, \xi)$. The unknown function is represented by a spline defined on an underlying grid. An arbitrary number of moments can be used for the reconstruction, and the real ξ -domain is identified iteratively during the reconstruction.

The standard approach presented in [John et al. \(2007\)](#) was very successful for many different distributions, but suffered from major drawbacks:

1. it cannot really reconstruct non-smooth distributions;
2. even smooth functions are not always well reconstructed, in particular when they involve several peaks (lack of generality).

As a whole, this means that the original procedure is not general enough. An in-depth analysis of the spline-based reconstruction process has shown that a tremendous progress could be obtained by placing the underlying grid points in an optimal manner. The main issue consists in finding appropriate criteria for an optimal distribution of the grid points. This issue has been addressed by the author in [de Souza et al. \(2010\)](#); the most prominent numerical results are discussed in the next subsections.

2.4.2 The adaptive spline-based reconstruction algorithm

The reconstruction of particle size distributions (PSD) as found in process engineering is our major purpose, in particular for non-homogeneous conditions in space. Thus, the usual constraints on the domain (internal coordinate ξ) and the range of the function $f(t, \xi)$ to be reconstructed apply as described in the introduction: the particle size is positive and bounded; the PSD f is nonnegative everywhere.

Let the first L moments of $f(t, \xi)$ be given at some time. An initial interval $[a, b]$, which should contain the real range of $f(t, \xi)$, is divided into n sub-intervals $[\xi_i, \xi_{i+1}]$, $i = 1, \dots, n$, with $a = \xi_1 < \xi_2 < \dots < \xi_{n+1} = b$. As in [John et al. \(2007\)](#), splines (piecewise polynomials with compatibility conditions at the nodes ξ_i , $i = 2, \dots, n$) of order 3 are used in the reconstruction. For such a cubic spline, there are in each interval 4 unknown coefficients of the cubic polynomial leading altogether to $4n$ unknowns. From the boundary conditions at x_1 and x_{n+1} and the compatibility conditions at ξ_i , $i = 2, \dots, n$, one obtains $3n + 3$ equations. The missing $L = n - 3$ equations come from the known moments of $f(t, \xi)$. Altogether, one has to solve in the spline-based reconstruction with cubic splines linear systems of equations of size $4n \times 4n$.

The spline-based reconstruction algorithm from [John et al. \(2007\)](#) is an iterative process. Given a mesh $\xi_1 < \xi_2 < \dots < \xi_{n+1}$, one iteration looks as follows:

1. *Solve the resulting linear system of equations.*
2. *Check if the interval $[\xi_1, \xi_{n+1}]$ for computing the reconstruction can be reduced.* This step is crucial for finding a good interval, which contains the real domain of $f(t, \xi)$. In this step, the absolute values of the current reconstruction in the sub-intervals at the boundaries $[\xi_1, \xi_2]$, $[\xi_n, \xi_{n+1}]$, are compared with the maximal value of the current reconstruction. If, for instance, the values in $[\xi_1, \xi_2]$ are negligibly small compared to the maximal value, the new left boundary for the reconstruction is set to be $\xi_1 := (\xi_1 + \xi_2)/2$. The same procedure is performed for the right boundary. If the interval has changed, the nodes are redistributed in an equidistant manner. Go to step 1.
3. *Regularize the solution of the linear system of equations.* If there is no recommendation to reduce the interval in step 2, but the reconstruction has local values which are exceedingly negative, the solution of the linear system will be regularized. This is done by removing subsequently the smallest singular values of the system matrix. After each such removal, it is checked again if the interval for the reconstruction can be reduced, i.e., step 2 is performed.

The algorithm stops if all values in the nodes and in the midpoints of the sub-intervals are almost non-negative and if no reduction of the interval for the reconstruction is recommended.

The regularization of the linear system removes first the smoothness of the second derivative in the nodes. Thus, the recommended reconstruction will be often not twice differentiable (the second order derivative of the PSD is a piecewise linear but discontinuous function). This is not an issue for engineering purposes.

The procedure for an adaptive redistribution of the nodes needs some starting guess about the shape of the expected solution. This is a classical requirement for adaptive methods, e.g., for the solution of partial differential equations. For this reason, the adaptive procedure starts only after the spline-based reconstruction has finished computing a first approximation of the solution on an equidistant grid using the original algorithm of [John et al. \(2007\)](#), which does not require any starting guess. The adaptive algorithm developed in [de Souza et al. \(2010\)](#) consists of the following steps:

1. *Compute the second-order derivative of the current approximation.* The key observation for choosing the initial nodes of the adaptive grid is that, if $f(t, \xi)$ changes the sign of its curvature quickly, as at narrow peaks, then it is not

possible to represent this region with a cubic function in one interval. This is because a cubic function can lead only to one single change of the sign of the curvature in one interval. In fact, the original algorithm always leads to very bad results if more than one change of the sign of the curvature of $f(t, \xi)$ occurs in one sub-interval (see for instance later Fig. 2.5). For this reason, we decided to place nodes at all points where the second-order derivative of the current reconstruction either changes its sign from a positive to a negative value, or vice versa.

2. *Compute the first-order and derivative of the current approximation.* Nodes are also placed in those sub-regions where the absolute value of the first-order derivative is large, i.e., where the solution is steep. This idea resembles the well-known gradient indicator in adaptive methods for partial differential equations. For choosing the next nodes of the adaptive grid, the first-order derivatives of the spline at the points of the current grid are thus evaluated. The obtained values are ordered with respect to their size (absolute value) and then grouped into so-called windows. The default number of windows is set to be equal to the number of nodes that still need to be chosen. In the first window all the points with the largest derivative values are gathered, but only those that have a minimal prescribed distance from the nearest node are finally accepted within the new list of nodes. Excessive clustering of nodes is avoided in this way. This procedure is applied until the appropriate total number of nodes has been obtained, which is given by the order of the spline and the number of known moments.
3. *Enlarge the domain.* Numerical tests have shown that it is useful to slightly enlarge at first the range identified by the original, equidistant algorithm of [John et al. \(2007\)](#) and to compute iteratively a new domain with the adaptively distributed nodes. For this purpose, the coordinate of the node ξ_{n+1} is multiplied in practice by 1.2 (20% increase).
4. Go to step 1 of the original algorithm using the new distribution of the nodes.

Now, the original algorithm of [John et al. \(2007\)](#) is performed again. After this, a new distribution of the nodes is computed with the adaptive procedure, and so on. For all the cases presented in this paper, three node redistributions have been required at most before finding the final solution.

An approximation $f^{(k-1)}$ is considered to be the final approximation of $f(t, \xi)$ if:

-
- the error associated with all moments is sufficiently small

$$\max_{i=0,\dots,L-1} |\text{relative error in } i\text{th moment of } f^{(k-1)}| < tol,$$

- and the approximation on the next adaptive grid leads to a growing mean error

$$\begin{aligned} & \sum_{i=0}^{L-1} |\text{relative error in } i\text{th moment of } f^{(k-1)}| \\ & \leq \sum_{i=0}^{L-1} |\text{relative error in } i\text{th moment of } f^{(k)}|. \end{aligned}$$

The workflow of the adaptive spline-based reconstruction algorithm is presented in Fig. 2.3.

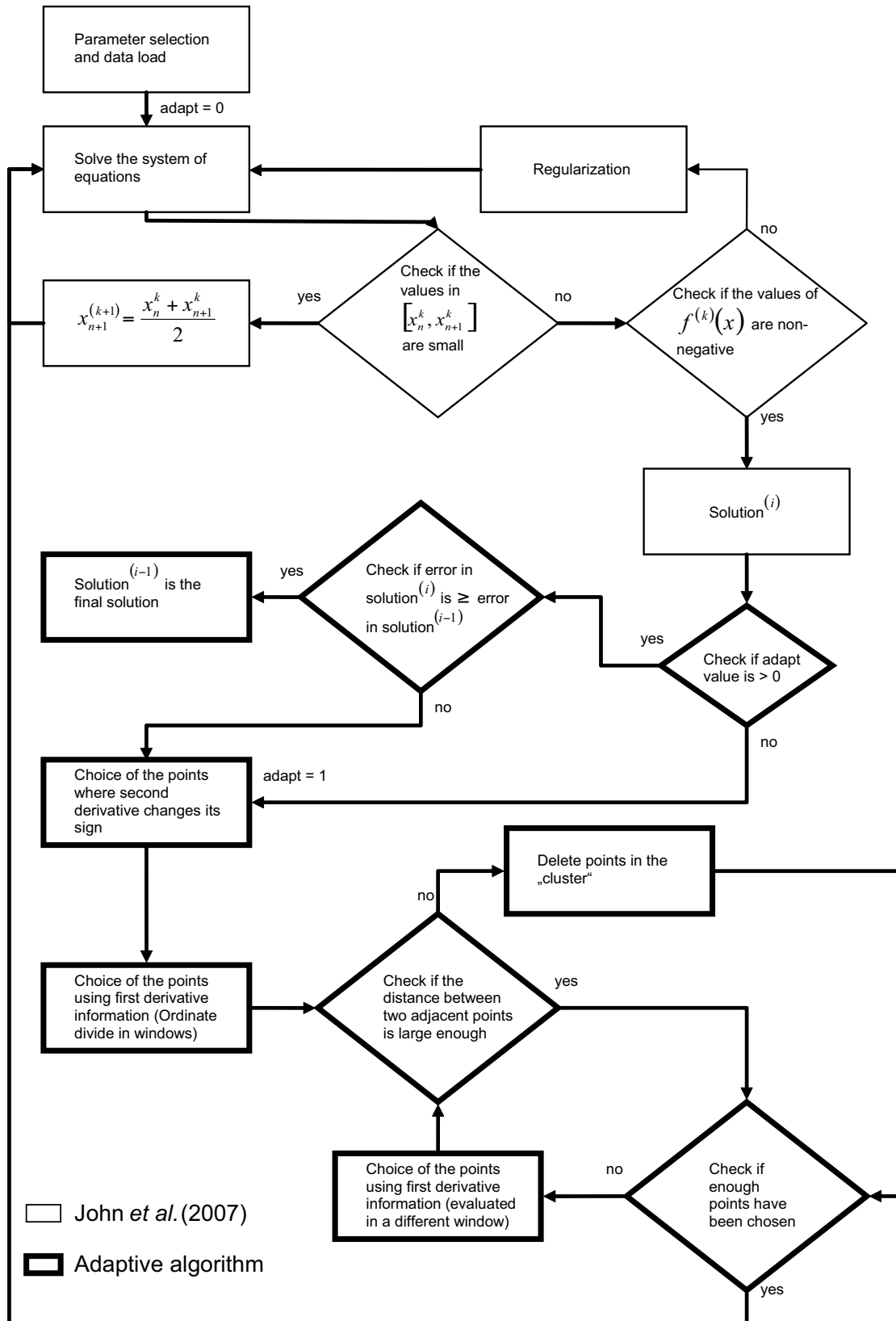


Figure 2.3: Workflow of the adaptive spline-based reconstruction algorithm.

2.4.3 Results and discussion

The spline-based reconstruction algorithm using equidistant grids has already shown excellent results for smooth distributions with a slowly changing sign of the PSD curvature ([John et al. \(2007\)](#)). Therefore, we concentrate here on the cases where the reconstruction was not really successful.

The chosen examples (values of all moments) come from crystallization applications, the data for all these test cases can be found in [John et al. \(2007\)](#). The adaptive algorithm has been implemented as a MATLAB script. The number of iterations needed to get the final distribution depends of course on the example considered and on the number of known moments. However, the computation time was less than 120 s on a standard PC for all simulations carried out up to now, including a graphical representation of all intermediate solutions. If necessary, this duration could be tremendously reduced by suppressing graphical outputs, writing a dedicated code instead of using MATLAB, optimizing further the algorithm and using a faster computer.

Multi-peak, smooth distributions

Figures [2.4\(a\)-\(f\)](#) present a comparison of the results obtained with the original (equidistant) and the adaptive algorithm for the smooth distribution with two peaks, one of them being considerably narrower than the other one. The reference distribution has been obtained numerically by solving directly the full population balance equations. Such a distribution with two peaks is typical of crystallization applications, for which seeds are employed initially, so that finally both seed crystals and newly nucleated crystals will be found at different sizes. More information on that topic can be found for example in [Qamar et al. \(2006\)](#), or for a more general picture in [Lorenz et al. \(2006\)](#).

As already shown in [John et al. \(2007\)](#), the original approach is not able to resolve the changing sign of the curvature for the first, narrow peak and thus leads globally to a poor result. The adaptive algorithm is in most cases able to find suitable positions for the nodes, leading to an excellent reconstruction of the reference distribution.

As explained in the introduction, only a limited number of moments are usually known. It is therefore important to check how many moments are really needed for a good reconstruction of the PSD. For this purpose, a systematic study showing the results for three up to eight moments is presented.

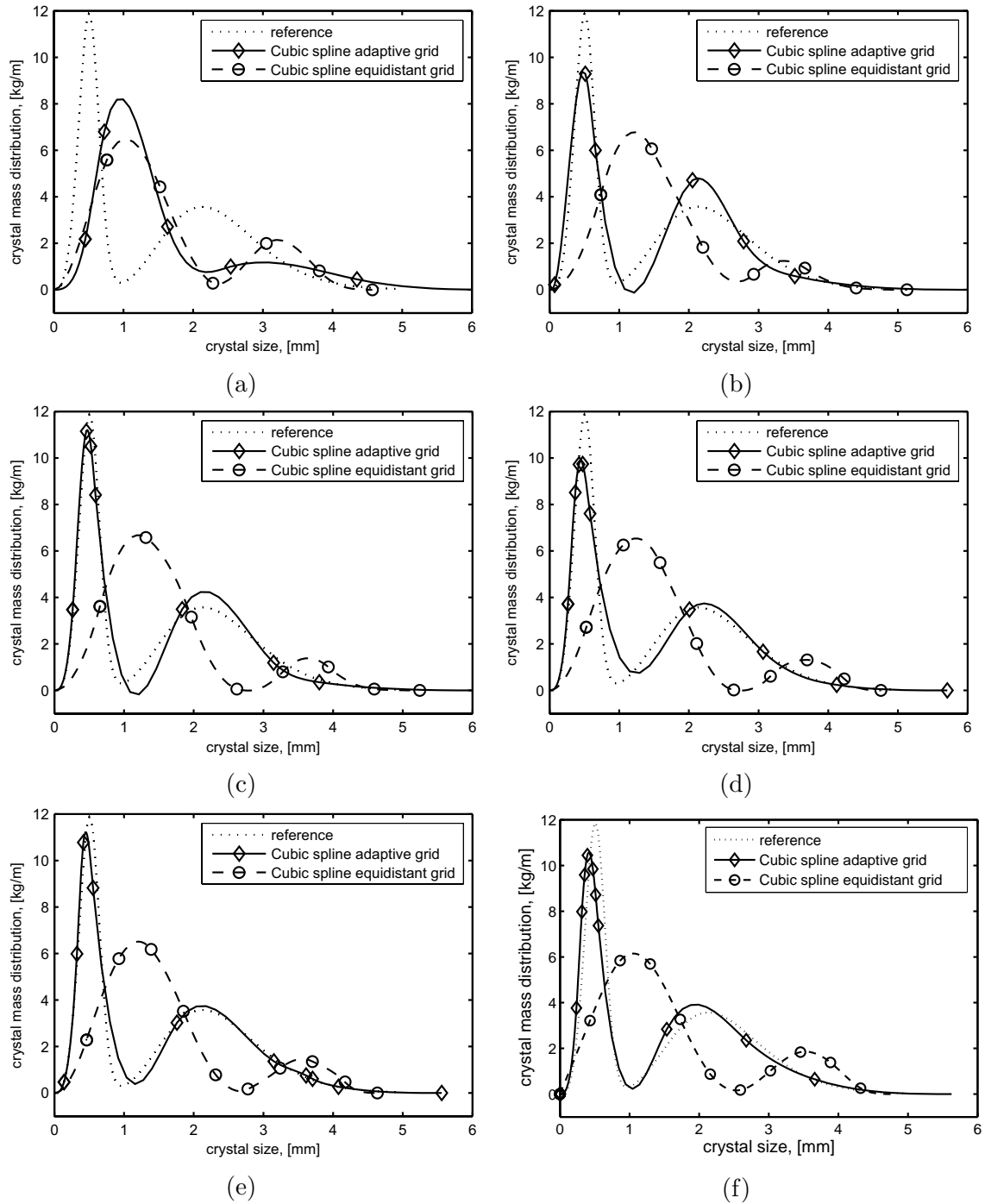


Figure 2.4: Reconstruction of a two-peak distribution, comparison of equidistant and adaptive algorithm using (a) three moments (b) four moments (c) five moments (d) six moments (e) seven moments (f) eight moments.

Visually, results obtained with four to eight moments (documented respectively in Fig. 2.4(b)-(f)) can be considered as good to very good. On the other hand, the reconstruction using just three moments does not resolve the peaks with high precision. This is due to the lack of information when using such a small number of moments.

A quantitative evaluation of the reconstruction quality is presented in Table 2.1 (standard algorithm) and Table 2.2 (adaptive algorithm). Different methods and parameters have been used in order to quantify precisely the quality of the reconstruction. First, the norm of the global error is defined as:

$$\text{Norm} = \frac{\sum_0^{x_{max}} |f_{rec}(x) - f_{ref}(x)|}{\sum_0^{x_{max}} |f_{ref}(x)|}$$

The correlation coefficient (Corr) between the reconstructed and the reference curve is furthermore computed using the built-in MATLAB function *corrcoef*.

For many practical purposes, the position and the height of the peaks observed in the PSD are essential pieces of information. Consequently, measuring the accuracy of the procedure for both quantities is also interesting, even if they do not describe the quality of the whole reconstruction. The corresponding errors are defined in the following equations:

Relative height difference (ΔH_{rel}):

$$\Delta H_{rel} = \frac{|f_{rec}(x_{rec,peak}) - f_{ref}(x_{ref,peak})|}{|f_{ref}(x_{ref,peak})|}$$

Relative position difference (ΔL_{rel}):

$$\Delta L_{rel} = \frac{|x_{rec,peak} - x_{ref,peak}|}{x_{ref,domain}}$$

The relative negativity

$$\text{Neg} = \frac{\min(f_{rec})}{\max(f_{rec})}$$

has also been quantified, since in some cases slightly negative values allow to obtain much better reconstructions. It is interesting to know how much this will affect the results.

Table 2.1: Quantitative evaluation of the smooth distribution reconstruction using the standard algorithm.

Case	Norm [%]	Corr [%]	Neg [%]		ΔH_{rel} [%]	ΔL_{rel} [%]
3 mom	95.8	17.8	0	left peak	43.8	11.6
				right peak	38.2	21.2
4 mom	98.8	9.3	0	left peak	41.3	14.8
				right peak	64.3	24.8
5 mom	107.6	9.5	0.14	left peak	42.1	14.8
				right peak	60.4	29.4
6 mom	104.9	12.1	0	left peak	43.4	14.2
				right peak	62.3	31.4
7 mom	102.5	13.2	0	left peak	43.5	14.0
				right peak	58.1	27.8
8 mom	101.9	12.2	0	left peak	41.5	13.2
				right peak	59.0	26.7

It can be seen clearly in Table 2.1 that the original algorithm of [John et al. \(2007\)](#) using an equidistant grid cannot produce the right solution. Even when considering more and more moments, the reconstruction quality does not increase measurably.

On the other hand, the adaptive algorithm (Table 2.2) fully exploits the supplementary information. With only three moments, the reconstruction is inaccurate. But, for four and more moments, the reconstruction quality is good up to excellent. Using more moments, the reconstruction quality increases further, but only slightly since the solution obtained with four moments is already good.

Table 2.2: Quantitative evaluation of the smooth distribution reconstruction using the adaptive algorithm.

Case	Norm [%]	Corr [%]	Neg [%]		ΔH_{rel} [%]	ΔL_{rel} [%]
3 mom	107.1	5.0	0	left peak	27.6	9.9
				right peak	67.3	19.0
4 mom	19.0	96.9	0.52	left peak	5.3	2.2
				right peak	21.9	1.4
5 mom	17.2	97.8	0.73	left peak	12.9	1.8
				right peak	11.2	1.8
6 mom	16.2	96.5	0	left peak	5.6	1.0
				right peak	4.8	1.8
7 mom	12.8	97.2	0	left peak	1.3	1.3
				right peak	3.9	0.8
8 mom	15.8	95.4	0	left peak	9.1	1.7
				right peak	4.5	1.8

Multi-peak, non-smooth distributions

The second example considers a non-smooth distribution with two peaks. The first peak is extremely narrow and drops suddenly from its maximal value to zero. This distribution corresponds again to a preferential crystallization process, described in more details in [Elsner et al. \(2005\)](#).

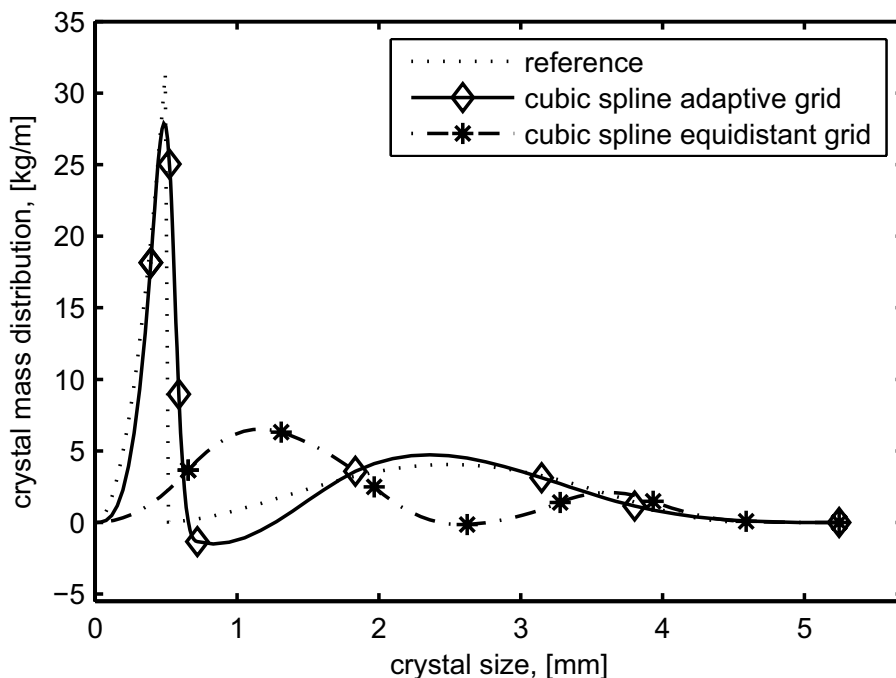


Figure 2.5: Reconstruction of a two-peak distribution with steep gradient using five moments, comparison of equidistant and adaptive algorithm.

The original algorithm on an equidistant grid completely fails for this application, as already shown in [John et al. \(2007\)](#). On the other hand, Fig. 2.5 demonstrates that the adaptive algorithm is able to give a rather good reconstruction for this very difficult case. The height and the position of both peaks are reproduced with good precision and even the steep gradient at the end of the first peak is relatively well resolved. The price to pay for this good resolution is a slightly negative value of the PSD for a short range behind the sharp peak. Since splines are intrinsically smooth functions, it cannot be expected that they will allow directly an exact description of a non-smooth PSD. This drawback is however in practice of minor importance compared to a correct estimation of the peak magnitudes and positions.

The quality of the reconstruction is quantified in Table 2.3. The comparison shows again the clear improvement of all indicators when using the adaptive algorithm. This shows that the adaptive spline-based reconstruction algorithm described in Section 2.4.2 is also able to automatically take into account a local non-smooth

behavior of the distribution to reconstruct.

Table 2.3: Quantitative evaluation of the non-smooth distribution reconstruction using five moments.

Case	Norm [%]	Corr [%]	Neg [%]		ΔH_{rel} [%]	ΔL_{rel} [%]
standard	135.3	19.1	9.5	left peak	69.4	16.9
				right peak	35.4	31.5
adaptive	35.7	80.2	5.3	left peak	11.0	0.2
				right peak	16.8	2.9

Robustness of the reconstruction

As already explained in the introduction, the developed reconstruction process must be as robust as possible. When considering experimental measurements, the uncertainty is not negligible. It must be checked that the predicted distribution is not impacted too strongly by such inaccurate inputs.

Even when considering results of numerical simulations, the shape and extent of the distribution are usually very poorly known at first. Therefore, the reconstruction must be able to work efficiently with a very low level of starting information.

Both issues have been checked separately, first by modifying the input moments by a certain percentage, thus mimicking a possible (measurement) error. In a second step, the size of the (guessed) initial domain has been varied over an order of magnitude, in order to quantify its impact.

The effect of an error in the moments has been first investigated. Systematic as well as random errors have been introduced in the original moments and the final distribution obtained can be seen in Fig. 2.6(a)-(b) respectively.

When considering systematic errors, all moments are modified by multiplying or dividing them with the same factor, e.g. 1.3 for 30% relative error. As demonstrated in Fig. 2.6(a), such systematic errors fortunately do not have a very large impact on the reconstruction. Even when a large relative error of 30% is applied, the shape of the distribution remains very similar and the position of the peaks is still very well predicted. This is undoubtedly related to the fact that the coupling between function and moments (Eq. 2.16) is linear.

Random errors have a larger impact on the shape of the distribution (Fig. 2.6(b)). For random errors, each moment is again multiplied or divided by the same factor (e.g. 1.1 for 10% relative error), but a random process is called to decide for each moment individually if a multiplication or a division should take place. As a consequence, some moments will be increased while some others reduced in a random manner.

Here also, the adaptive algorithm has been able to deliver a reconstruction of acceptable quality. In fact, the algorithm works indeed very well and delivers the correct moments with a very high accuracy. The observed discrepancies are directly connected to the random modification of the moments. Even a small change in the moments leads to a considerably different distribution. This illustrates the need for an accurate determination of the moments. The needed level of accuracy certainly constitutes a real challenge, in particular for experimental measurements.

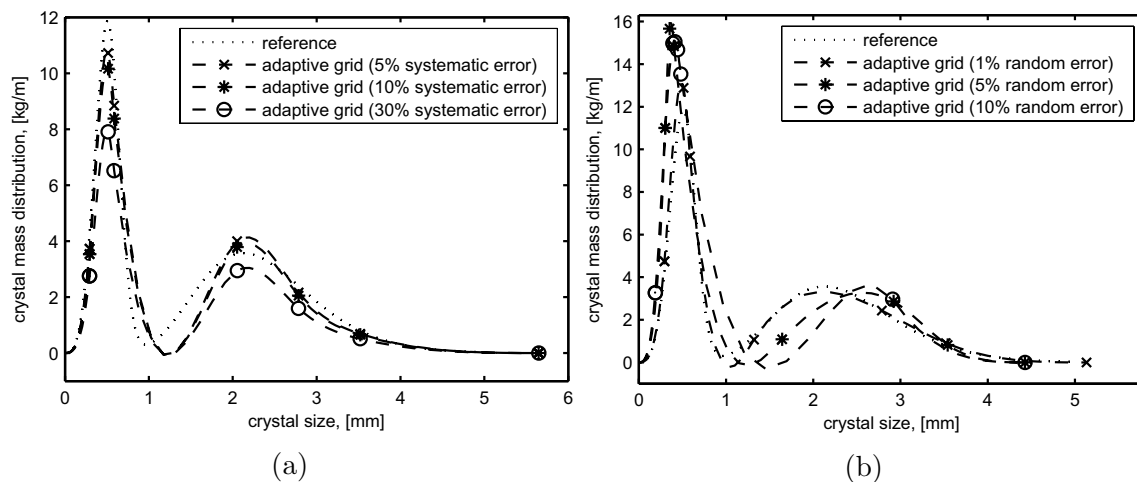


Figure 2.6: Reconstruction of a two-peak distribution using four moments (a) with systematic error (b) with random error.

Altogether, the reconstructions obtained with the adaptive algorithm are of a much better quality and considerably more robust than the original results using an equidistant grid for all configurations tested up to now, without any exception.

2.4.4 Conclusions

In this section, the adaptive spline-based algorithm for the reconstruction of distributions from a finite set of moments introduced by the author in [de Souza et al. \(2010\)](#) has been presented. The algorithm shows a considerable improvement comparing with the original equidistant-grid algorithm ([John et al. \(2007\)](#)), which failed to reconstruct distributions with a quickly changing curvature or with local non-smooth behavior. The needed computing time is still very small (expressed in seconds, without optimizing the process), so that it would be probably possible to use this algorithm for process control.

The numerous tests carried out during the development of this procedure reveal following features:

- For a really accurate reconstruction of a two-peak, smooth distribution, four

moments should be known. A reconstruction with only three moments is already possible, but will lead only to a semi-quantitative description.

- It is not necessary to know the domain of the function to reconstruct with a high precision. A first guess with only the right order of magnitude (i.e., knowing only the typical size of the largest particles) is fully sufficient to start the process. A good initial guess is twice the real domain of interest, if known in advance.
- When more moments are known, the accuracy of the reconstruction increases as expected.
- To reconstruct accurately a non-smooth distribution, more moments are needed than for a smooth distribution. As a rough recommendation, one moment more should be known for each non-smooth event compared to a smooth distribution with the same number of peaks.
- The reconstruction process is robust enough to tolerate some error in the moment values. Nevertheless, these errors must of course be minimized, since a random error of 10% might already lead in reality to a considerably different distribution.

Since its publishing, the developed algorithm has been successfully applied to reconstruct distributions in different scientific applications, for instance, quantum physics (Slater (2011)), process control (Soltanzadeh and Dumont (2012)) and pharmaceutical process (Mortier et al. (2014)).

2.5 Summary

In this chapter, the methods to simulate polydisperse multiphase flows have been presented. The described methods are later employed for the simulation of a full multiphase chemical reactor.

The Eulerian-Eulerian approach has been chosen as it is the most appropriate framework for the computation of dense flow, which is common in practical industrial applications. Thus, the continuous and disperse phase are described using the Eulerian approach. The model to simulate the multiphase flow, as well as the model to describe the evolution of the particles properties have been discussed. As such, the Eulerian multifluid model together with the required constitutive relations are outlined. In order to get a correct description of the disperse phase the quadrature

method of moments (QMOM) is applied to solve the population balance equation; the coupling between CFD and QMOM is explained with details.

Finally, a reconstruction technique was presented, which allows to recover the shape of a distribution from a finite set of moments; this technique can be used as a tool to analyse the information obtained with the moment-based methods.

Chapter 3

Methodology for model parameter optimization using multi-objective genetic algorithm

In this short chapter, a methodology for the optimization of model parameters using multi-objective optimization is described. The advantages of multi-objective optimization, basic concepts and the coupling between simulation software and optimization algorithm are discussed. The presented methodology is later on employed for the model optimization of a turbulence RANS model (Chapter 4) and for the model optimization of a chemical catalytic reaction network (Chapter 5).

3.1 Introduction

A mathematical model often requires calibration to fit a particular condition. Even when very complex physical and chemical models are employed, there are usually empirical, semi-empirical or pure numerical parameters that need to be tuned.

The optimal parameter set should minimize the difference between experimental data and simulation results. In principle, many algorithms could be applied to solve this optimization problem. Gradient-based algorithms, e.g., Newton's method, Steepest-Descent, Levenberg-Maquardt, yield an accurate local minima or maxima, but depend strongly on the starting values of the parameters. Metaheuristic optimization algorithms, e.g., Genetic Algorithms (GA), Simulated Annealing (SA), Particle Swarm Optimization (PSO), provide an effective global search, but do not guarantee finding the global minima or maxima.

In multi-variable and non-linear optimization problems, which is often the case in complex systems, an effective global search is needed. Metaheuristic algorithms have become a popular approach to solve this class of optimization problems as they

provide an effective search in the variable space and are less prone to premature convergence to a suboptimal solution.

There are numerous articles applying metaheuristic algorithms for model parameter optimization, e.g., reaction kinetics parameters (Polifke et al. (1998), Elliott et al. (2005), Park et al. (2010)), coalescence model parameters (Hasseine et al. (2006)), heat transfer coefficient (Tesch et al. (2009)). However, most of them consider only a single objective function.

In most practical situations, a multi-objective optimization would be a far more valuable tool for the determination of optimal model parameters. For instance: when the same set of parameters should be used to fit a model to different experimental conditions or configurations; when the same set of parameters should be used to fit different models and give optimal prediction for distinct quantities. Multi-objective optimization accounts for a trade-off between concurrent objectives, increasing the robustness of the model and reducing ad hoc fitting.

Multi-objective optimization has gained popularity in engineering optimization problems, see Rangaiah and Pandu (2008) and Janiga (2011) for a broad range of applications in chemical engineering and computational fluid dynamics, respectively. Nevertheless, its use in model parameter optimization has remained relatively poorly explored, being only recently addressed with more details in Rangaiah and Bonilla-Petriciolet (2013).

3.2 Multi-objective optimization

Multi-objective optimization deals with the problem of optimizing (i.e., maximizing or minimizing) more than one objective function simultaneously. The optimization problem can be stated as follows:

$$\min f_i(\theta) \quad \forall i = 1, 2, \dots, N_{obj}$$

subjected to:

$$\theta_j \in [\theta_{j,min}; \theta_{j,max}] \quad j = 1, 2, \dots, N_{param}$$

where N_{obj} is the number of objectives and N_{param} is the number of parameters. The objective functions are given by f_i and the parameter vector is given by θ_j . The constraint $[\theta_{j,min}; \theta_{j,max}]$ defines a feasible set of parameters.

The objective functions are usually conflicting, and in most cases there is not a single solution that optimizes all the objectives simultaneously. There are different

approaches to solve multi-objective problems. A common practice is to weight the objectives and combine them together into a single objective function. In this manner the problem is reduced to a single objective optimization. This approach, however, introduces an artificial ordering in the objectives and leads to suboptimal results.

A more elaborated approach is based on the Pareto concept, which formalizes the trade-off between concurrent objectives; no artificial weight or combination into a mono-objective function is needed. Genetic algorithms are well suited to solve multi-objective problems since the Pareto strategy can be easily integrated in the optimization algorithm loop. In genetic algorithms (Goldberg (1989)), a randomly generated population of solutions (also called individuals) evolves towards better solutions. It uses mechanisms inspired by genetics and evolution theory, such as inheritance, mutation and crossover to obtain the solutions along the generations. As in evolution theory, the fittest individuals are favored in the selection procedure. Most of the multi-objective GAs consider the Pareto dominance criterion for the classification of the individual fitness. Nevertheless, there are considerable differences on the fitness assignment depending on the algorithm. A comprehensive overview on the most popular multi-objective GA is given by Konak et al. (2006).

3.3 Basic concepts

In order to better understand multi-objective optimization problems using genetic algorithms and its applications in model parameter optimization, some basic concepts are first explained.

3.3.1 Pareto optimality

Considering the scenario involving the simultaneous optimization of N_{obj} , possibly contradicting objectives, the determination of an optimal solution is not a trivial task. Usually it is not possible to find a solution that optimizes all the objectives simultaneously. When dealing with two or more objectives, a given solution may perform optimally for one objective, but poorly for another. Therefore, a compromise should be found.

The Pareto concept formalizes the trade-off between concurrent objectives. The rank between all the individuals is established based on the number of solutions that each individual dominates. In Pareto-based approaches (Goldberg (1989)), the solution A is said to dominate solution B if and only if for all the objectives, the solution A is at least in one objective better than B and not worse in any objective function.

A solution is Pareto-optimal if it is not dominated by any other solution. The Pareto-optimal solution cannot be improved in any of the objectives without worsening at least one of the other objectives. A set of Pareto solutions constitutes the Pareto front and may contain infinite number of solutions, see Fig. 3.1.

The challenge of multi-objective algorithms is to describe well-distributed solutions close to the true Pareto, within the region of interest.

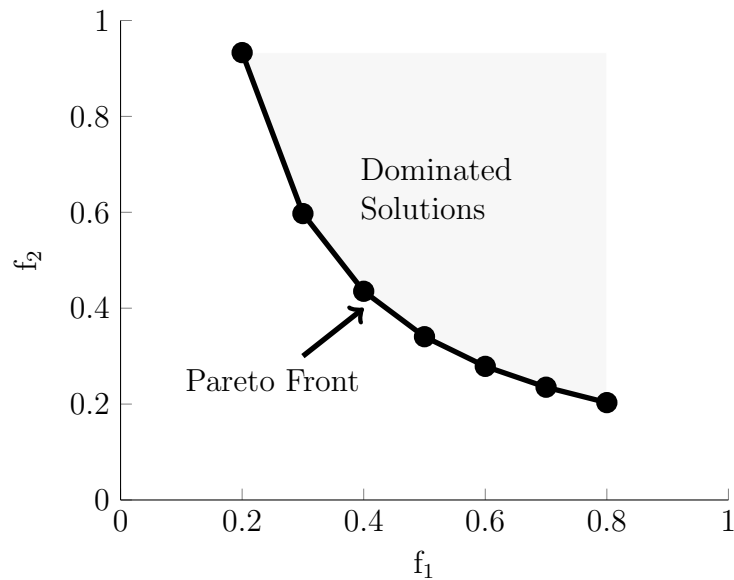


Figure 3.1: Pareto front for two contradicting objective functions.

3.3.2 Decision making

From the mathematic point of view, all solutions in the Pareto are of the same quality. The process of choosing between one of the optimal solutions usually requires preferential information of the decision maker; this process is called decision making.

In engineering applications, the decision-making criterion is normally based on an economic decision. In the case of model parameter optimization of physical or chemical models, the most important aspects are the fitting quality and statistical properties of the model.

Nevertheless, the choice of the final solution generally involves the trade-off of certain criteria (objectives) for others. Mathematical tools that help in the decision making process are investigated in the field of multi-criteria decision-making (MCDM), see [Sean and Yang \(1998\)](#).

The following MCDM methods have used in this work:

1. *Weighted sum method.* It is the simplest and most known MCDM. In this

method, the objectives are linearly combined using some prescribed weights. Thus, the final problem reduces to a single objective optimization within the Pareto optimal solutions.

2. *Aspiration levels method.* In this case each objective is compared to a threshold. The solutions that perform worse than a given threshold are filtered out reducing the subset of interesting Pareto solutions. This threshold can be made tighter until only very few solutions (or only one solution) remain, see [Lotfi et al. \(1992\)](#).
3. *“Best of the worst” or Maximin/Minimax strategy.* For each Pareto solution, the worst objective is determined. Then, the best within the worst objectives is selected. As the objectives usually have different unities and scales, the normalization of the objectives is needed in order to obtain comparable values.

3.4 Coupling simulation software with optimization algorithm

The calculation of the mathematical functions is usually done in specialized simulation softwares, e.g., ANSYS Fluent, OpenFOAM, Matlab. To couple simulation softwares with optimization algorithm implies building an interface to control and exchange data between the softwares in an automatic manner.

There exist a few optimization softwares that provide a flexible interface, state-of-art optimization algorithms libraries, fast communication between the softwares and offer the possibility for parallelization of the simulations. In this work, we have used the in-house software OPTimization ALgorithm (OPAL) and the commercial software ModeFRONTIER for the optimizations. Although there are significative differences between the softwares, a general optimization loop is proposed in [Fig. 3.2](#).

A general optimization loop can be described in three main steps:

1. *Optimization strategy:* In this step the optimization algorithm is set up, e.g., MOGA, NSGA-II. The main parameters to be defined are: initial population size, number of generations, number of objective functions, number of design variables (parameters), design variable constraints (parameter range). In model optimization the parameter range can be defined based on the values usually adopted in literature. Other important multi-objective GA settings include: mutation probability, mutation magnitude and crossover probability.
2. *Computation of mathematical functions:* Depending on the complexity of the problem this step may require several simulation softwares. For the cases

considered in this work the commercial software ANSYS Fluent and MATLAB have been used for the simulation and evaluation of the objective functions.

The model is treated as a “black box” by the optimizer. The model parameter input is generated by the optimization algorithm. The output of the model is an integral quantity or a profile that should be compared with the experimental data for the calculation of the objective function.

3. *Analysis of the results:* As already mentioned, the result of a multi-objective optimization is usually not a single optimum, but a set of optimal solutions. In this last step, a decision-making process is needed in order to choose a final solution within the Pareto optimal set.

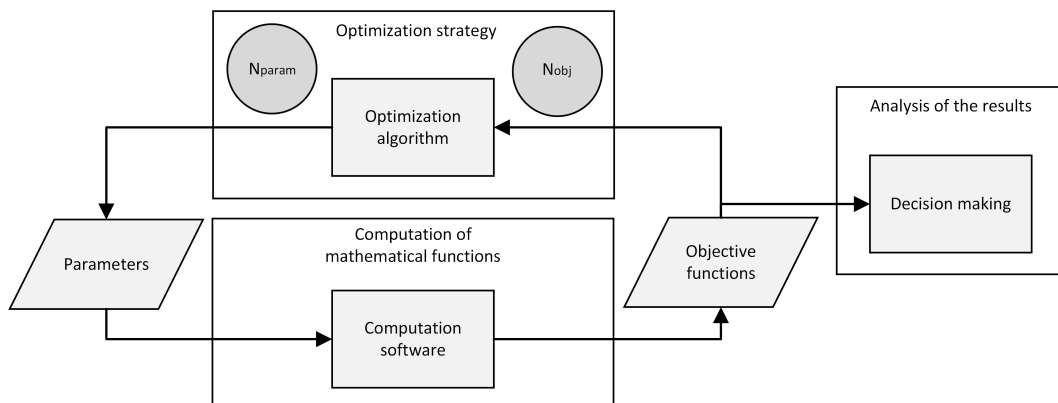


Figure 3.2: Diagram showing a general optimization loop.

3.5 Summary

In this chapter, a methodology for model parameter optimization has been described. The advantages of multi-objective optimization, basic concepts and the coupling between simulation software and optimization algorithm have been discussed.

Multi-objective optimization is clearly a valuable tool for the determination of optimal model parameters, as it accounts for a trade-off between concurrent objectives, increasing the generality of the model and reducing ad hoc fitting.

The presented methodology is employed for the model optimization of a turbulence RANS model and for the model optimization of a chemical catalytic reaction network in Chapter 4 and Chapter 5, respectively.

In model parameter optimization the decision-making criterion is not based on economic decisions, as it is usually the case in engineering application. The fitting quality has been used in the decision making-process. Nevertheless, in future works, more advanced statistical analysis could be integrated.

Chapter 4

Model optimization for turbulent flows

This chapter is written based on the following paper:

L. M. de Souza, G. Janiga, D. Thévenin. Multi-objective optimisation of the Model Parameters for the Realizable $k - \epsilon$ Turbulence Model, (2015). Progress in Computational Fluid Dynamics, in press.

4.1 Introduction

The accurate prediction of turbulent flows is a fundamental issue to improve existing applications and develop new configurations. A detailed level of prediction can in principle be obtained with Direct Numerical Simulation (DNS), but limitations in computer power restrict its application to simple configurations and low Reynolds numbers. Large Eddy Simulation (LES) is now applicable for many research problems but simulation times are still prohibitive for many industrial applications, [Fröhlich \(2006\)](#). Therefore, numerical simulations based on Reynolds Averaged Navier-Stokes (RANS) models are still widely used today for practical engineering problems ([Spalart \(2000, 2010\)](#)), see also [Spalart \(2009\)](#) for an interesting text on “RANS modelling into a second century”.

In RANS models, closure parameters (sometimes misleadingly called “constants”) are introduced in order to replace unknown correlations appearing during the averaging process. These parameters are usually determined in a semi-empirical manner based on basic flow configurations and on simplifying assumptions, for instance by considering the properties of homogeneous isotropic turbulence. Afterwards, these models are applied for quite different and far more complex configurations. For a particular flow, it is known that the prediction can usually be improved by adjusting the model parameters, at the cost of generality. Consequently, a large span of model

parameter values have been tested in the scientific literature, derived from the own experience of the user on a trial-and-error basis, from values measured in a particular experiment or, less often, obtained by single-objective numerical optimization, as discussed later.

The determination of suitable model parameters for engineering turbulence is indeed a formidable task. It is easy to change one parameter in order to observe consequences concerning some specific turbulent quantity of the flow. But the simultaneous modification of several parameters of a turbulence model in order to increase accuracy for a variety of configurations rapidly becomes an intractable issue. If all the model parameters are changed in a systematic manner, then the number of possible combinations would yield an enormous and unnecessary computational effort when attempting to explore the model parameter space. In that case, numerical optimization techniques may help speeding up the search procedure in order to find the best possible combination of model parameters with a minimum computational load.

In this chapter, the objective is to determine optimized but generally applicable model parameters for the prediction of turbulent quantities. In order to ensure generality, four widely-used canonic flow configurations are considered simultaneously in the optimization: channel, backward facing step, jet and flow over a periodic hill. High-quality experimental data available from scientific articles, ERCOFTAC (<http://cfm.mace.manchester.ac.uk/ercoftac/>) and QNET (<http://qnet-ercoftac.cfms.org.uk/>) databases are available as reference. The test cases considered are classically retained as benchmark for development and validation of turbulence models. The underlying characteristics allow to investigate the behavior of the model under very different conditions. The optimization problem thus involves several concurrent objectives that must be fulfilled simultaneously. The multi-objective genetic algorithm implemented in the in-house computer package OPAL (Thévenin and Janiga (2008)) has been used for optimization.

The present study considers only the realizable $k - \epsilon$ turbulence model. The four adjustable parameters of this model have been therefore selected as the four design parameters of the optimization procedure, as described in what follows. The initial range for each parameter spans the corresponding values published in the literature. The differences between selected quantities obtained with this model and those measured experimentally are quantified using the Euclidian norm. The objective of the optimization is to minimize simultaneously all these differences.

4.2 The closure problem

The closure problem arises from the averaging procedure of the Navier-Stokes equation. In the conservative form the Navier-Stokes equation is written as follows:

$$\rho \frac{\partial u_i}{\partial t} + \rho \frac{\partial u_j u_i}{\partial x_j} = -\frac{\partial p}{\partial x_i} + \frac{\partial(2\mu s_{ij})}{\partial x_j} \quad (4.1)$$

being the strain rate tensor s_{ij} given by,

$$s_{ij} = \frac{1}{2} \left(\frac{\partial u_i}{\partial x_j} + \frac{\partial u_j}{\partial x_i} \right) \quad (4.2)$$

Considering that the instantaneous velocity is expressed by $u_i(x, t) = U_i(x, t) + u'_i(x, t)$, where $u'_i(x, t)$ is the fluctuating velocity and $U_i(x, t)$ the mean velocity. The time-averaged Navier-Stokes equations reads:

$$\rho \frac{\partial U_i}{\partial t} + \rho \frac{\partial (U_j U_i + \overline{u'_j u'_i})}{\partial x_j} = -\frac{\partial P}{\partial x_i} + \frac{\partial(2\mu s_{ij})}{\partial x_j} \quad (4.3)$$

The instantaneous and the time-averaged equations, respectively Eq. (4.1) and Eq. (4.3), are very similar; with the instantaneous quantities being substituted by mean quantities in the time-averaged equation. Another difference is the correlation $\overline{u'_j u'_i}$, which appears in Eq. (4.3).

The fundamental problem in RANS modeling is the description of $\tau_{ij} = \overline{u'_j u'_i}$, which is referred as the Reynolds stress tensor. The averaging process has produced new unknowns, but has not generated new equations. There are at this point more variables than equations; therefore, the system is not closed. The task in turbulence modeling is to find approximations to describe the Reynolds stress tensor τ_{ij} .

It is possible to derive equations for the Reynolds stress tensor or other turbulent quantities, for example, the turbulent kinetic energy k . This can be done after a large number of algebraic manipulation of the Navier-Stokes equation. However, such procedures generate new unknown correlations and can not balance the number of unknowns and equations.

4.3 Two-equation RANS models

The Boussinesq assumption serves as basis for the RANS modeling. Boussinesq postulated that the Reynolds stress tensor in turbulent flows τ_{ij} could be described analogously to the viscous stress in laminar flows. The equation of τ_{ij} for incompressible flows is given by:

$$\tau_{ij} = -2\nu_T S_{ij} - \frac{2}{3}k\delta_{ij} \quad (4.4)$$

The second term on the right-hand side has been introduced in order to avoid unphysical results; δ_{ij} is the so-called Kronecker delta, which is 1 if $i = j$ and 0 otherwise. The mean stress rate S_{ij} reads:

$$S_{ij} = \frac{1}{2} \left(\frac{\partial U_i}{\partial x_j} + \frac{\partial U_j}{\partial x_i} \right) \quad (4.5)$$

Note that the turbulent eddy viscosity ν_T , different from the molecular viscosity, is not a property of the fluid. It changes from point to point depending of the state of turbulence in a specific point. The question is how to determine the turbulent eddy viscosity ν_T .

Perhaps the most controversial aspect in RANS modelling is the description of the turbulent eddy viscosity. One can argue that the closure relation of this term is based just on dimensional analysis and not on fundamental physics. Nonetheless, dimension analysis has been historically a powerful tool for deducing properties of turbulent flows.

There is no fundamental reason for ν_T to depend only upon a particular turbulence quantity or quantities. Distinct approaches have proven their applicabilities, e.g., zero-equation model (e.g., Mixing length), one-equation model (e.g., Spalart-Allmaras), two-equation models (e.g., $k - \epsilon$, $k - \omega$). The two-equation models are the most successful. While algebraic models and most one-equation models need to prescribe the turbulence length scale based on some flow dimension, two-equation models automatically provide the turbulence length scale or equivalent being therefore called “complete” models.

The turbulent eddy viscosity ν_T can be regard as the product from a velocity scale $u(x, t)$ and a length scale $l(x, t)$:

$$\nu_T \propto ul \quad (4.6)$$

Hence, for the complete specification of ν_T we need to describe a velocity scale, which is usually done based upon the turbulence kinetic energy k . However, there is a large arbitrariness in the choice of the second quantity. Based on dimensional analysis, any quantity which can be stated as a product between k and l , in principle, can be used. Authors have adopted many different variables to describe the length scale, e.g., dissipation rate (ϵ), specific dissipation rate (ω). Yet, these distinct formulations are theoretically equivalent.

The derived equation for k , obtained from algebraic manipulation of the Navier-

Stokes equation, is given by:

$$\frac{\partial k}{\partial t} + U_j \frac{\partial k}{\partial x_j} = \tau_{ij} \frac{\partial U_i}{\partial x_j} - \epsilon + \frac{\partial}{\partial x_j} \left[\nu \frac{\partial k}{\partial x_j} - \frac{1}{2} \overline{u'_i u'_i u'_j} - \frac{1}{\rho} \overline{p u'_j} \right] \quad (4.7)$$

In Eq. (4.7) the unsteady and convection terms are given on the left-hand side. On the right-hand side the first term is called Production (P_k) and describes the rate of turbulent kinetic energy transfer from the mean flow to the turbulence. The dissipation rate (ϵ) is the rate with which turbulence kinetic energy is converted into thermal energy. The term $\nu \frac{\partial k}{\partial x_j}$ represents the molecular diffusion. The triple velocity correlation is usually referred as turbulent transport and the last term on the right-hand side is the pressure diffusion.

The exact derivation of equations for turbulent quantities from the Navier-Stokes equation yields unknown double- and triple-velocity correlations. Wilcox (2001) points out that the modeling of the physics is more important than the modeling of the differential equations, and therefore, the term-by-term modeling is not the most appropriate approach. The modeled version of turbulence kinetic energy in Eq. (4.7) assumes the form:

$$\frac{\partial k}{\partial t} + U_j \frac{\partial k}{\partial x_j} = \tau_{ij} \frac{U_i}{x_j} - \epsilon + \frac{\partial}{\partial x_i} \left[\left(\nu + \frac{\nu_T}{\sigma_k} \right) \frac{\partial k}{\partial x_i} \right] \quad (4.8)$$

where τ_{ij} is given by Eq. (4.4). Note that the unsteady term, convection and molecular are exactly represented, while the remaining terms are modeled using closure approximations.

In Appendix A, the most popular two-equation models are shown, as well as their standard closure approximations. The equation for the turbulent kinetic energy is similar for all the given models, nevertheless, distinct closure constants are used. Major differences are observed in the second transport equation, where new terms and auxiliary relations are introduced.

4.4 The realizable $k - \epsilon$ turbulence model

The $k - \epsilon$ model has been developed by several contributors, starting from early efforts of Chou (1945) and Harlow and Nakayama (1968), but most prominently in the 70s by Hanjalić (1970), Jones and Launder (1972) as well as Launder and Spalding (1974). Its standard form is now usually credited to Launder and Sharma (1974). Since then, many different and extended formulations have been published. The realizable $k - \epsilon$ model was first proposed by Shih et al. (1995) and has soon become very popular. In general, it provides superior predictions for flows involving

rotation, boundary layers under strong adverse pressure gradients, separation and recirculation.

The realizable $k - \epsilon$ model differs from the original one in two main respects. First, it involves a new formulation for the eddy turbulent viscosity. Second, it uses a modified equation for the dissipation rate (ϵ), while the equation for k remains exactly the same as in the standard model. The corresponding transport equations for k and ϵ read:

$$\frac{\partial k}{\partial t} + U_j \frac{\partial k}{\partial x_j} = \frac{\partial}{\partial x_j} \left[\left(\nu + \frac{\nu_t}{\sigma_k} \right) \frac{\partial k}{\partial x_j} \right] + P_k + P_b - \epsilon \quad (4.9)$$

$$\frac{\partial \epsilon}{\partial t} + U_j \frac{\partial \epsilon}{\partial x_j} = \frac{\partial}{\partial x_j} \left[\left(\nu + \frac{\nu_t}{\sigma_\epsilon} \right) \frac{\partial \epsilon}{\partial x_j} \right] + C_1 S_\epsilon - C_2 \frac{\epsilon^2}{k + \sqrt{\nu \epsilon}} + C_{1\epsilon} \frac{\epsilon}{k} C_{3\epsilon} P_b \quad (4.10)$$

where the term P_k accounts for the turbulence kinetic energy production due to mean velocity gradient as it appears in Eq. (4.7) and the term P_b is the turbulence energy production due to buoyancy. In the ϵ equation, a new source term S_ϵ has been introduced together with the parameter C_1 . The new parameter C_1 has been described by [Shih et al. \(1995\)](#) as follows:

$$C_1 = \max \left[0.43, \frac{\eta}{\eta + 5} \right] \quad (4.11)$$

with $\eta = s \frac{k}{\epsilon}$, $s = \sqrt{2s_{ij}s_{ij}}$

The last term on the right-hand in Eq. (4.10) does not appear in the original formulation of [Shih et al. \(1995\)](#), but is adopted in the implementations such of the commercial Software ANSYS Fluent.

The eddy viscosity reads as in the standard model:

$$\nu_T = \frac{C_\mu k^2}{\epsilon} \quad (4.12)$$

In the realizable $k - \epsilon$ formulation, the eddy viscosity model satisfies the so-called realizability constraints. This means that the models should have positive value for the normal Reynolds stresses and also respect the Schwarz inequality for the shear stresses.

From the expression for the normal Reynolds stress in an incompressible flow (see Eq. 4.4), note that the result of the normal stress, $\overline{u'_j u'_j}$, which is a positive quantity, becomes negative when the strain is large enough to satisfy the inequality in Eq. (4.13).

$$\frac{k}{\epsilon} \frac{\partial U_j}{\partial x_j} > \frac{1}{3C_\mu} \quad (4.13)$$

In the same way, the Schwarz inequality for shear stresses ($\overline{u_i u_j^2} \leq \overline{u_i^2 u_j^2}$) is violated for very large strain rate.

This inconsistency in the model can be mitigated using a variable value for C_μ . Experiments as well as DNS data suggest that the value for C_μ changes depending on the flow (Pope (2000)). Supported by the work of Reynolds (1987), Shih et al. (1995) elaborated a formulation for C_μ as follows:

$$C_\mu = \frac{1}{A_0 + A_s \frac{U^{(*)} k}{\epsilon}} \quad (4.14)$$

with $U^{(*)} = \sqrt{s_{ij}s_{ij} + \tilde{\Omega}_{ij}\tilde{\Omega}_{ij}}$, $\tilde{\Omega}_{ij} = \Omega_{ij} - 2\epsilon_{ijk}\omega_k$, $\Omega_{ij} = \overline{\Omega_{ij}} - \epsilon_{ijk}\omega_k$, where $\overline{\Omega_{ij}}$ is the mean rate-of-rotation tensor and ω_k is the angular velocity. The parameter A_s is given by:

$$A_s = \sqrt{6} \cos \phi \quad (4.15)$$

with $\phi = \frac{1}{3} \arccos(\sqrt{6}W)$, $W = \frac{s_{ij}s_{jk}s_{ki}}{\tilde{S}}$, $\tilde{S} = \sqrt{S_{ij}S_{ij}}$

The commonly accepted model parameters for the realizable $k - \epsilon$ description are presently: C_μ (given by Eq.(4.14)), $A_0 = 4.04$, C_1 (given by Eq.(4.11)), $C_2 = 1.9$, $\sigma_k = 1.0$ and $\sigma_\epsilon = 1.2$ (Shih et al. (1995)) and $C_{\epsilon 1} = 1.44$, see ANSYS Inc. (2011).

4.4.1 Determination of the model parameters

The closure parameters in RANS model have been introduced in order to replace unknown double and triple correlations by algebraic expressions. A traditional way to determine the closure parameters consists in applying the general equations to simple, canonical flows so that several terms in the transport equations can be simplified and only one or two coefficients remain in the resulting equation. The next step is the comparison with theory, experimental data or DNS, to determine those coefficients, as exemplified in what follows.

Determination of constant C_2

The value of C_2 for the realizable $k - \epsilon$ model has been determined experimentally by considering the decay of isotropic turbulence behind a grid at high Reynolds number, see Shih et al. (1995). The experiment consists of a uniform flow past a

grid. Considering $U_i = U_{i,0}$ and $U_j = U_k = 0$ and neglecting turbulent diffusion in the streamwise direction, the equation for k reduces for a uniform flow to:

$$U_{i,0} \frac{dk}{dx_i} = -\epsilon \quad (4.16)$$

and the equation for ϵ can be written as follows:

$$U_{i,0} \frac{d\epsilon}{dx_i} = -C_2 \frac{\epsilon^2}{k} \quad (4.17)$$

Combining both and eliminating $\frac{d\epsilon}{dx_i}$ and ϵ , we obtain:

$$k \frac{dk^2}{dx_i^2} = -C_2 \left(\frac{dk}{dx_i} \right)^2 \quad (4.18)$$

The analytical solution for this equation shows that the decay of k obeys a power law, $k = \alpha x_i^{-n}$, with α being a constant depending on the particular experiment and n being:

$$n = \frac{1}{(C_2 - 1)} \quad (4.19)$$

Experiments by [Batchelor and Townsend \(1948\)](#) yield the value $n = 1$, whereas [Mohamed and Larue \(1990\)](#) obtained values n in the range between 1.08 and 1.3. The latter range allows C_2 to assume a value in the span $C_2 \in (1.77; 1.93)$. The recommended value of 1.9 corresponds to $n = 1.11$. Yet, it is possible to find in the scientific literature values between 1.68 (for instance [Sarkar et al. \(1997\)](#)) and 2.0 (see [Duynderke \(1988\)](#)).

The parameters $C_{\epsilon 2}$ in the standard $k - \epsilon$ and C_2 in the realizable $k - \epsilon$ model are equivalent and calibrated using the same simple flows. We refer to C_2 when dealing with the realizable $k - \epsilon$ model and to $C_{\epsilon 2}$ when using the standard version.

Determination of constant $C_{\epsilon 1}$

A relation between $C_{\epsilon 1}$ and C_2 can be determined based on the homogeneous turbulent shear flow behind a grid. For this kind of flow, $U_i = U_{i,0}(x_j)$, $U_j = U_k = 0$ and $\frac{\partial}{\partial x_i} = \frac{\partial}{\partial x_j} = 0$. Under these considerations the k -equation becomes:

$$P_k - \epsilon = 0 \quad (4.20)$$

and the equation for ϵ can be written as:

$$C_{\epsilon 1} \frac{\epsilon}{k} P_k - C_2 \frac{\epsilon^2}{k} \approx 0 \quad (4.21)$$

Substituting Eq.(4.20) in (4.21), one obtains $C_{\epsilon 1} \approx C_2 = 1.9$, using the previously recommended value for C_2 . Nevertheless, the conventional value for $C_{\epsilon 1}$ is set to 1.44, following [Launder and Spalding \(1974\)](#).

A homogeneous turbulent shear flow has been investigated in [Tavoularis and Corrsin \(1981\)](#). There, diffusion effects can be neglected and the equation for k reads:

$$U_i \frac{dk}{dx_i} = P_k - \epsilon = \epsilon \left(\frac{P_k}{\epsilon} - 1 \right) \quad (4.22)$$

From their experimental data it is possible to derive that $\frac{P_k}{\epsilon}$ and $\frac{\epsilon}{k}$ are almost constant. Thus, the equations for ϵ and k can be written as follows:

$$\left(\frac{\epsilon}{k} \right) U_i \frac{dk}{dx_i} = U_i \frac{d\epsilon}{dx_i} = -C_{\epsilon 1} \frac{\epsilon}{k} P_k - C_2 \frac{\epsilon^2}{k} \quad (4.23)$$

Combining Eqs. (4.22) and (4.23):

$$C_{\epsilon 1} = 1 + \frac{\epsilon}{P_k} (C_2 - 1) \quad (4.24)$$

From the experiments of [Tavoularis and Corrsin \(1981\)](#) and [Harris et al. \(1977\)](#) the value of $\frac{\epsilon}{P_k}$ can be determined. If $\frac{\epsilon}{P_k} = 1$, one obtains $C_{\epsilon 1} = C_2$. The popular value $C_{\epsilon 1} = 1.44$ is obtained when $\frac{\epsilon}{P_k} \approx 0.5$.

Recently, [Goebbert et al. \(2011\)](#) used dissipation energy analysis from DNS simulation to obtain theoretical values of the C_2 and $C_{\epsilon 1}$ constants for different Reynolds number. The range obtained was $C_2 \in [0.57, 1.64]$ and $C_{\epsilon 1} \in [0.425, 1.20]$, with the theoretical values approaching the semi-empirical ones for high Reynolds number.

Determination of constants C_μ and A_0

The eddy viscosity formulation in the realizable $k - \epsilon$ models allows for a variable parameter C_μ , satisfying the realizability constraints. A new unknown A_0 is introduced in the model. In [Shih et al. \(1995\)](#) the value for this constant is calibrated using simple flows (homogeneous shear flow, boundary layer). The finally proposed value $A_0 = 4.04$ corresponds to $C_\mu = 0.09$ in the inertial sublayer and $C_\mu = 0.06$ in the case of homogeneous shear flow. These are close to values presented in [Pope \(2000\)](#), where DNS results combined with the relation $C_\mu = \frac{\nu_T \epsilon}{k^2}$ show that C_μ is close

to 0.09 except near the wall where it decays. To our knowledge, no other alternative value for A_0 can be found in the literature.

Determination of constants σ_k and σ_ϵ

The values for the parameters σ_k and σ_ϵ can be calibrated based on the analysis of the logarithm region in a boundary layer flow. In [Launder and Spalding \(1972\)](#) an analysis revealed that σ_k may assume values between 0.5 (free stream flow) and 1.75 (near-wall flow). For pipe flows values have been found in the range from 0.7 up to 1.0 depending on the Reynolds number. Finally, [Launder and Spalding \(1972\)](#) have suggested as most probable value $\sigma_k = 1.0$.

An analysis of the log-law layer ([Libby \(1996\)](#)) leads to following relation:

$$\sigma_\epsilon = \frac{\kappa^2}{C_2 C_\mu^{1/2} - C_{\epsilon 1}} \quad (4.25)$$

considering the von Kármán constant κ in the range $[0.40, 0.41]$. This relation, however, is not verified by the conventionally accepted parameter values. It might be interesting to mention here that even the value of the von Kármán constant, one of the most important constants in fluid dynamics, is not known precisely, with scientists defending values from 0.37 to 0.436, see [Spalart \(2009\)](#).

In the work of [Hoffman \(1975\)](#), the behavior of the $k - \epsilon$ model is examined at the turbulent/non-turbulent interface to determine a limit value for the turbulent diffusion coefficients σ_ϵ and σ_k . This analysis leads to the relation $\sigma_k = \frac{2}{n}$ and $\sigma_\epsilon = \frac{3}{n}$, where n is the exponent of the mean streamwise profile, which should then be determined by experiments. For $n = 2$, one obtains $\sigma_k = 1$ and $\sigma_\epsilon = 1.5$, thus very close to the standard values. However, [Nee and Kovasznay \(1969\)](#) have observed in their experiments a close fit to $n = 1$, which would deliver $\sigma_k = 2$ and $\sigma_\epsilon = 3$.

Two other arguments can be found in the literature to justify values for σ_k and σ_ϵ . Firstly, in the direction away from the boundary layer the dissipation rate should be vanishing faster than the rate of turbulent kinetic energy. This requires σ_k smaller than σ_ϵ to satisfy the realizability of the model. Secondly, boundary edges of turbulent kinetic energy appear to extend further than the mean velocity profiles. This implies σ_k less than unity. Including these recommendations the values proposed by [Chen and Kim \(1987\)](#) are: $\sigma_k = 0.75$ and $\sigma_\epsilon = 1.15$.

Determination of constant $C_{\epsilon 3}$

It is also possible to find in the literature some references regarding the parameter $C_{3\epsilon}$ (see [Henkes and van der Flugt \(1991\)](#)). This parameter is related to the degree

in which ϵ is affected by buoyancy. Generally, this parameter is defined assuming the following relation:

$$C_{\epsilon 3} = \tanh \left| \frac{v}{u} \right| \quad (4.26)$$

where the component v is the velocity of the flow parallel to the gravitational vector direction and u is the velocity component perpendicular to the gravitational vector.

4.4.2 Overall values in literature

To summarize, since the publication of the standard form of the model in the early 70s, numerous parameter sets have been proposed. Table 4.1 provides a corresponding overview.

An independent estimation of the model parameters has been discussed by [Qian and Cai \(2001\)](#) in order to find a best set of constants for the $k - \epsilon$ model. The corresponding optimization problem was solved in this case applying the Newton-Raphson scheme, investigating three configurations: channel flow with Reynolds number 388 000, backward facing step (BFS) with expansion rate 1.5 and Reynolds number 44 000 and BFS with expansion rate 1.125 and Reynolds number 36 000. This differs from the present work, as the parameter estimation has been performed separately for each cases. The authors finally do not come up with a single, best set of model parameters. Moreover, some of the optimal values differ strongly from the conventional values (see Table 4.1), which might be surprising for such a well-established model.

Different values of C_μ can be found in the literature for the standard $k - \epsilon$ model. In many cases this parameter is tailored for a certain application in order to mitigate some other deficiency of the model. For example, [Bottema \(1997\)](#) shows that the turbulence overproduction in front of an obstacle can be mitigated by specifically tuning the standard $k - \epsilon$ model for boundary layer flows. A theoretical relation between an inactive turbulence parameter and C_μ is established, resulting in a value of $C_\mu = 0.03$.

In [Darbandi et al. \(2006\)](#), a modified $k - \epsilon$ turbulence model was applied for the simulation of a multi-element airfoil (NACA 0012). Optimized values for $C_{\epsilon 1}$ and C_2 were obtained using a single-objective simplex optimization algorithm. The improved model showed better predictions for the pressure coefficient (C_P) at different attack, Mach and Reynolds numbers. Nevertheless, this is a tailored solution for a particular case and the application of such model for different geometries were not considered.

As a consequence, we decided to consider again this question using an efficient, multi-objective parameter optimization involving a broad variety of canonical flows in order to ensure a suitable generality of the results.

Table 4.1: Parameter values found in the literature for the $k - \epsilon$ model family. Note that C_μ is variable in the realizable $k - \epsilon$. Therefore, it is not considered in the present optimization. All parameters are dimensionless.

C_μ	$C_{\epsilon 1}$	C_2	σ_k	σ_ϵ	Author
0.07	1.45	2.0	1.0	1.3	Hanjalić (1970)
0.09	1.55	2.0	1.0	1.3	Jones and Launder (1972)
0.09	1.44	1.92	1.0	1.3	Launder and Sharma (1974)
0.09			1.0-2.0	1.5-3.0	Hoffman (1975)
	1.15	1.90	0.75	1.15	Chen and Kim (1987)
		1.83	1.0		Duynkerke (1988)
		1.9	1.0	1.2	Shih et al. (1995)
0.03					Bottema (1997)
0.088	1.391	1.826	1.0	1.3	Qian and Cai (2001)
0.554	1.416	1.672	1.0	1.3	Qian and Cai (2001)
0.102	1.180	1.513	1.0	1.3	Qian and Cai (2001)
0.01-0.17					Pope (2000)
	0.425-1.20	0.457-1.64			Goebbert et al. (2011)

4.5 Selected test cases

The four test cases considered for the optimization are standard benchmarks for development and validation of turbulence models. The experimental data have been collected from the ERCOFTAC database, QNET database and peer-reviewed articles. The selected flows include wall-bounded flows and boundary-free flows at high Reynolds number; these test cases present distinct flow phenomena, e.g., separation of the boundary layer over a sharp edge, separation of the boundary layer over a curved surface, recirculation, reattachment, free shear layer; such distinct underlying characteristics allow to investigate the behavior of the model under very different conditions.

For each configuration a relevant turbulent quantity, later called assessment parameter (AP), is considered as objective function for the optimization. Details about the CFD simulations, as well as mesh independence study are discussed in Section 4.6.

4.5.1 Channel flow

The experimental data for the channel flow was obtained from [El Telbany and Reynolds \(1981\)](#). Measurements of mean velocities, fluctuation velocities, as well as derived quantities such as the turbulence kinetic energy, are available for several flat channels configurations.

The measurements are given in the midplane close to the exit of the channel ($x = 60h$, see the dashed line represented in [Figure 4.1](#)), where the flow is assumed to be fully developed.

Schematic view of the channel geometry is shown in [Figure 4.1](#); overall characteristics of the considered configuration are presented in [Table 4.2](#). The turbulence kinetic energy was chosen as assessment parameter for the channel flow.

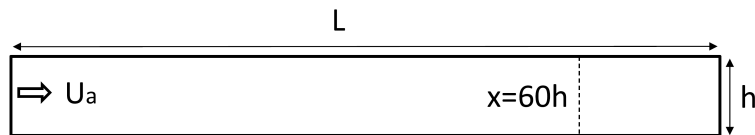


Figure 4.1: Channel geometry scheme.

Table 4.2: Overall characteristics of the channel flow.

Flow parameters	
Channel height (h)	0.033 m
Channel length (L)	2.440 m
Average velocity (U_a)	14.55 m/s
Reynolds number (Re_{2h})	64 600

4.5.2 Backward-facing step

The backward-facing step (BFS) is a classical example of flow separation and reattachment. The data for this test case was taken from the experiments of [Ruck and Makiola \(1993\)](#) and is available on the ERCOFTAC database website. Velocity data measurements are available at several locations after the step (see dashed lines in [Figure 4.2](#)), which allows the calculation of integral quantities, e.g, reattachment length.

The characteristics of the selected configuration are given in [Table 4.3](#) and the geometry scheme is shown in [Figure 4.2](#). The reattachment length after the step was chosen as assessment parameter for the optimization.

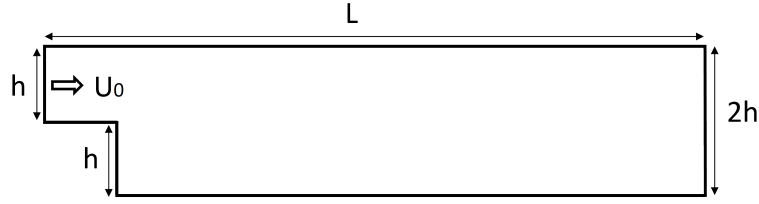


Figure 4.2: BFS geometry scheme.

Table 4.3: Overall characteristics of the BFS.

Flow parameters	
Step height (h)	0.025 m
Step inclination angle	90°
Expansion rate (ER)	2
Reference velocity (U_0)	42.34 m/s
Reynolds number (Re_h)	64 000

4.5.3 Free jet

The reference experimental data for the round free jet flow was obtained from [Modaress et al. \(1982\)](#). It is an example of free shear flow, which includes velocity decay and spread along the axial distance. Details about the experimental geometry and flow parameters are shown in Figure 4.3 and Table 4.4, respectively.

The assessment parameter for this case is the jet spreading rate, which was calculated based on measurement data of axial velocity (U_{axial}) along the axis and its radial evolution at ($x = 40r$).

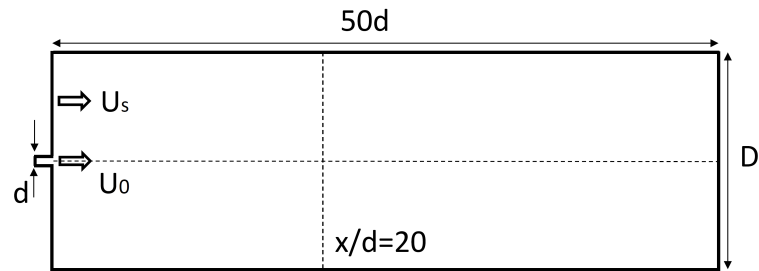


Figure 4.3: Jet flow geometry scheme.

Table 4.4: Overall characteristics of the jet flow.

Flow parameters	
Injector diameter (d)	0.02 m
Diameter of the chamber (D)	$30d$
Velocity on the axis (U_0)	13.4 m/s
Primary velocity profile ($U(r)$)	$U_0(1 - 2\frac{r}{d})^{1/66}$
Primary intensity of turbulence (u')	$U_0(0.04 + 0.1(\frac{r}{d}))$
Secondary velocity (U_s)	0.05 m/s
Secondary intensity of turbulence (U_s)	0.1
Reynolds number (Re_d)	18 350

4.5.4 Flow over periodic hill

The test case of the flow over a periodic hill was taken from the ERCOFTAC QNET database. The data is from experiments at the Laboratory for Hydromechanics of the Technical University of Munich (Rapp (2009)). It exhibits complex flow phenomena such as separation from a curved surface, recirculation and natural reattachment.

Details about the geometry and characteristics of the flow are shown in Figure 4.4 and Table 4.5, respectively. The reattachment length after the hill was chosen as assessment parameter for the optimization.

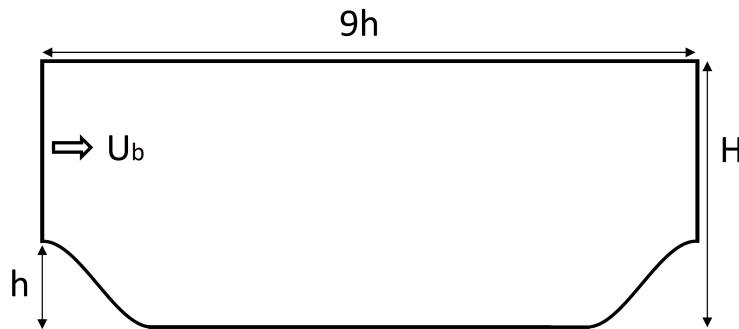


Figure 4.4: Periodic hill geometry scheme.

Table 4.5: Overall characteristics of the flow over a periodic hill.

Flow parameters	
Height (H)	$3.035h$
Hill height (h)	0.05 m
Reference velocity (U_b)	0.59 m/s
Reynolds number (Re_h)	37 000

4.6 Details of the CFD simulations

All cases have been set up using the commercial software FLUENT 6.3. To increase the accuracy of the simulation, all cases have been computed with double precision. The second-order, upwind interpolation scheme and the default pressure-velocity coupling method (SIMPLE) have been systematically employed for pressure-velocity coupling. Sufficiently low residual thresholds have been imposed for continuity, u , v , k and ϵ residuals; convergence has been associated with normalized residuals below 10^{-6} for all those quantities.

Boundary conditions were chosen to approximate experimental conditions as close as possible. Values for k and ϵ , when not given at inlet, were calculated from classical correlations.

The standard wall function was systematically adopted in this work for all the simulations. Studies using the near-wall treatment were not considered in this first investigation, but will be subject of further works.

4.7 Multi-objective optimization

The in-house optimization code OPAL (OPTimization ALgorithm, described for instance in [Thévenin and Janiga \(2008\)](#) and [Hilbert et al. \(2006\)](#)) was used to perform the optimization. The CFD simulations were performed in FLUENT while the objective functions were evaluated in MATLAB. As described in Chapter 3, in OPAL the optimization loop is performed in an automatic manner, the schematic representation of the optimization loop is shown in Figure 4.5.

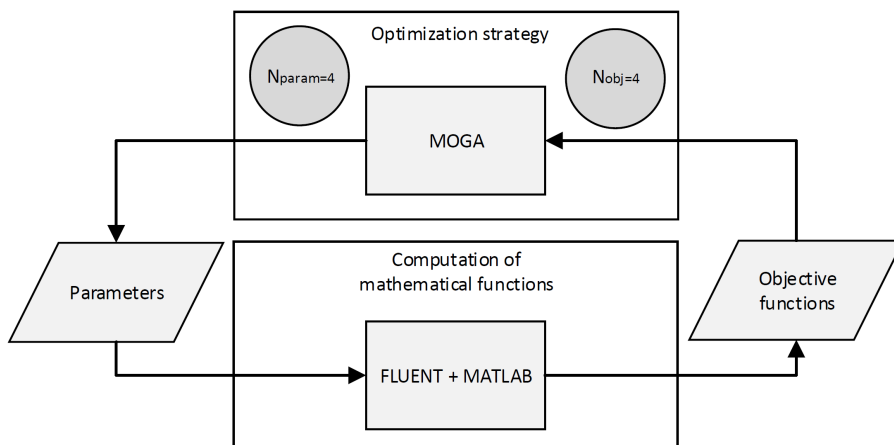


Figure 4.5: Diagram showing the optimization loop. A C program is used for the automatization of the loop.

The specific multi-objective optimization problem can be formulated as:

$$\min f_i(\boldsymbol{\theta}) \quad \forall i = 1, 2, \dots, N_{obj}$$

subjected to:

$$x_j \in [\theta_{j,min}; \theta_{j,max}] \quad j = 1, 2, \dots, N_{param}$$

where $N_{obj} = 4$ is the number of objective functions (four test-cases) and $N_{param} = 4$ is the number of model parameters to optimize. Limit values for the parameters $\boldsymbol{\theta}$ have been set based on the values found in the analysis of the literature (see Table 4.1). The retained parameter range is given by ($C_{e1} \in [1.15; 1.55]$; $C_2 \in [1.51; 2.0]$; $\sigma_k \in [0.75; 2.0]$; $\sigma_\epsilon \in [1.0; 3.0]$). The objective functions (difference between CFD results and reference data) have been calculated using the Euclidean norm and should be minimized.

Altogether, 620 designs (parameter sets) have been evaluated. The total computing time for the optimization was around 12 days using a single PentiumIV PC (2.7 GHz/2 GB memory).

The settings used in the multi-objective optimization algorithm are summarized in Table 4.6. For further details, the reader is referred to [Hilbert et al. \(2006\)](#) and [Thévenin and Janiga \(2008\)](#).

Table 4.6: Settings for the Multi-objective optimization algorithm.

Settings for MOGA	
Initial population size	40 (SOBOL)
Number of generations	30
Average offspring	10
Crossover offspring	10
Mutation probability	95%
Mutation magnitude	50 %
	($\times 0.9$ at each generation)

4.8 Independent configurations

The optimized parameters have been tested in four additional configurations, which were not included in the optimization. A brief description of the selected configurations is presented in the following subsections.

4.8.1 Savonius turbine

The unsteady flow around a vertical-axis (Savonius) wind turbine was investigated by Mohamed (2011). Torque and power coefficients (C_m and C_p , respectively) was compared with the experimental measurements of Hayashi et al. (2005). Sketch of the geometry and computational domain are shown in Figure 4.6. Overall characteristics of the flow are given in Table 4.7.

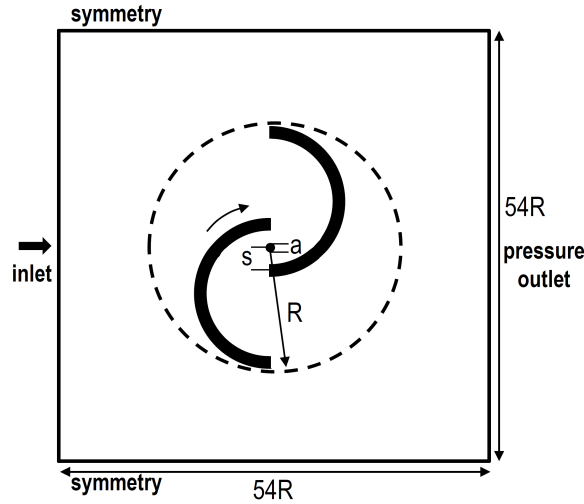


Figure 4.6: Sketch of the geometry and computational domain for the Savonius wind turbine.

Table 4.7: Overall characteristics of the Savonius wind turbine and selected assessment parameters.

Flow parameters	Assessment parameters
Rotor diameter (D)	0.33
Bucket diameter (d)	0.184 m
Bucket rotation angle (a)	30°
Speed ratios (λ)	0.3-1.2
	C_p, C_m

4.8.2 Airfoil wake

The incompressible flow around a conventional airfoil (DSMA661) at zero angle of incidence was simulated. The velocity profile in the wake of the airfoil was compared with the experimental data of Nakayama (1985) described in the ERCOFTAC database. The geometry sketch and computational domain are shown in Figure 4.7. Overall characteristics of the flow are given in Table 4.8.

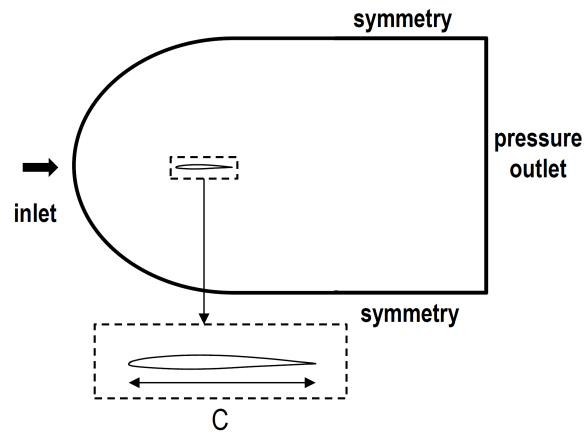


Figure 4.7: Sketch of the geometry and computational domains for the airfoil wake test case.

Table 4.8: Overall characteristics of the airfoil wake test case and selected assessment parameter.

Flow parameters		Assessment parameter
Chord length (C)	0.610 m	
Angle of attack	0°	
Reference velocity (U_{ref})	30.5 m/s	U profile across the wake
Turbulence intensity	0.02	
Reynolds number (Re_C)	120 000	

4.8.3 Flow around building

The flow and turbulence in the wake of an airport building were investigated. The experimental data for this configuration was obtained from the QNET database. The geometry sketch and computational domain are shown in Figure 4.8. Overall characteristics of the flow are given in Table 4.9.

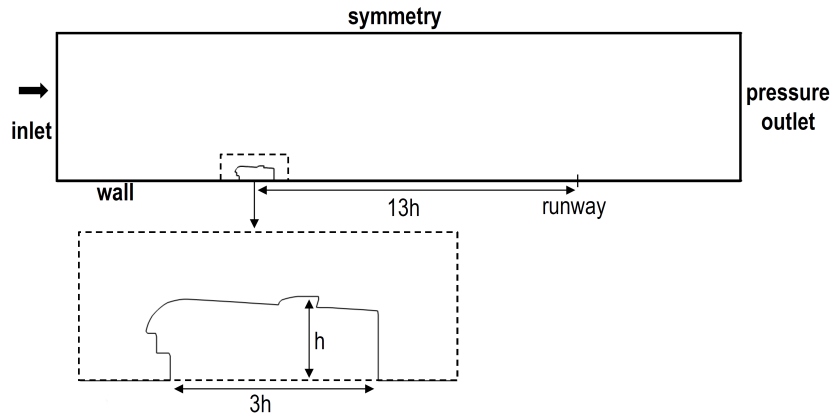


Figure 4.8: Sketch of the geometry and computational domain for the flow around building.

Table 4.9: Overall characteristics of the flow around a building and selected assessment parameter.

Flow parameters		Assessment parameter
Height (H)	37 m	U at the runway
Wind direction	0°	
Reference velocity (U)	2 m/s	
Reynolds number (Re_h)	5×10^6	

4.8.4 Square duct with 180° bend

The flow through a square duct was investigated. The experimental data for this configuration was obtained from the experiments of [Choi et al. \(1989\)](#) available ERCOFTAC database. The geometry sketch and computational domain are shown in Figure 4.9. Overall characteristics of the flow are given in Table 4.10.

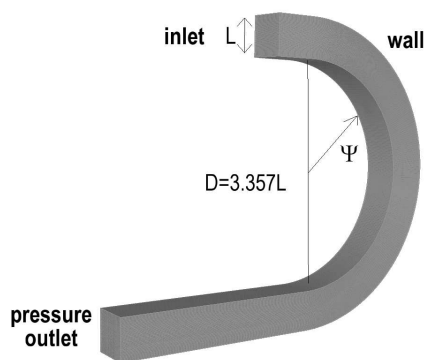


Figure 4.9: Sketch of the geometry and computational domain for the square duct with 180° bend.

Table 4.10: Overall characteristics of the square duct with 180° bend flow and selected assessment parameter.

Flow parameters		Assessment parameter
Height (H)	0.0889 m	Centerline streamwise velocity
Centerline curvature radius (R_c)	$3.357H$	
Inlet bulk axial velocity (W_B)	11 m/s	
Reynolds number (Re_{W_b})	56 690	

4.9 Results and discussion

Optimal parameter values were manually selected from the optimal set (Pareto solutions). As shown in Figure 4.10 the Pareto set consisted of very distinct designs. The procedure to identify a single optimal solution screened a set of Pareto designs based on the comparison with the standard model, i.e., solutions with better or equally good predictions for the 4 test cases were selected. From these pre-screened solutions the optimal set was chosen as being that with the parameter values closest to the recommended values from the literature.

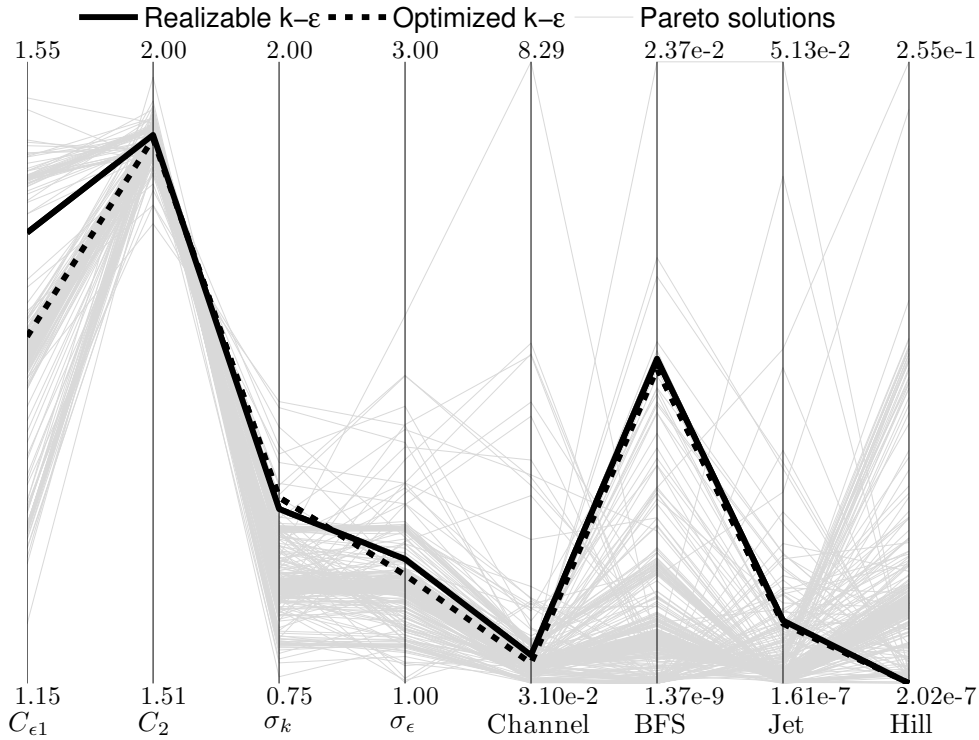


Figure 4.10: Parallel coordinate plot. Each line is associated with a different design and connects the values of the parameters (4 vertical axes on the left) and the objective function of each test cases (4 vertical axes on the right).

The parameters obtained in this manner (Table 4.11) differ by less than 5% from the standard values.

Table 4.11: Optimal parameter values for the $k - \epsilon$ model.

$k - \epsilon$ Model	$C_{\epsilon 1}$	C_2	σ_k	σ_ϵ
Realizable (standard)	1.44	1.9	1.0	1.2
Realizable (optimized)	1.37	1.89	1.02	1.14
Relative difference [%]	4.64	0.25	0.25	4.79

The obtained optimized realizable $k - \epsilon$ model was then compared with the RNG, standard and realizable $k - \epsilon$ models for all considered test cases. The results are presented in Figure 4.11 and in Tables 4.12 to 4.14. The best predictions are systematically obtained with the optimized model, both the standard and optimized realizable models performing equally well for the flow over a periodic hill.

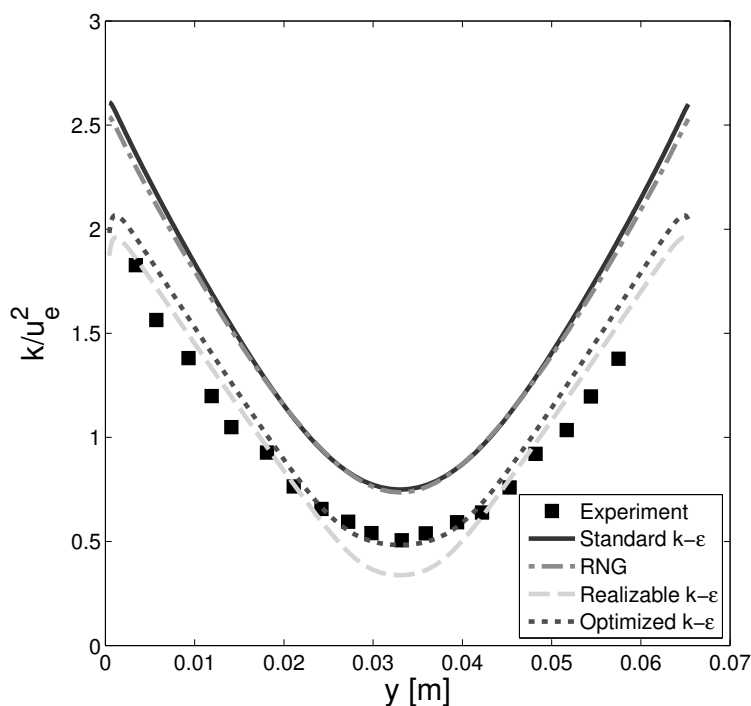


Figure 4.11: Turbulent kinetic energy (TKE) scaled with the effective friction velocity.

Some of the known deficiencies of the standard $k - \epsilon$ model such as the overprediction of the reattachment length for the BFS and the underprediction of the spread rate for the round jet have been mitigated with the new set of parameters. The turbulent kinetic energy k shows also a sensible improvement for the channel flow, especially in the center part of the channel.

The best result for the prediction of the reattachment length in the case of the periodic hill was obtained by the realizable $k - \epsilon$ with the conventional set of parameters. However, the optimized model can still predict the reattachment length within less than 1% relative difference from the experimental result, a value probably well within the experimental uncertainty.

Table 4.12: Reattachment length for the BFS case.

Model	Reattachment length [cm]	Relative difference [%]
Experiment	20.97	-
Standard	15.91	24.11
RNG	17.98	14.23
Realizable	18.54	11.58
Optimized	18.67	10.96

Table 4.13: Spread rate values for the jet flow case.

Model	Spread rate $S = \frac{dy_{1/2}}{dx}$	Relative difference [%]
Experiment	0.1047	-
Standard	0.1142	9.07
RNG	0.1309	25.02
Realizable	0.1130	7.92
Optimized	0.1121	7.06

Table 4.14: Reattachment length for the periodic hill case.

Model	Reattachment length [cm]	Relative difference [%]
Experiment	17.7650	-
Standard	12.9335	27.19
RNG	18.3835	3.48
Realizable	17.8330	0.38
Optimized	17.9355	0.95

In a final step, the general applicability of the optimized realizable $k - \epsilon$ model is further tested by considering four different configurations. The optimal parameter set has first been tested in a more complex and completely independent configuration, the unsteady flow around a vertical-axis (Savonius) wind turbine investigated by [Mohamed \(2011\)](#). Geometry and boundary conditions are shown in [Figure 4.6](#).

The values of torque coefficient (C_m) and power coefficient (C_p) for the two-blade Savonius rotor are investigated and compared with experimental data from [Hayashi et al. \(2005\)](#) for a standard range of operation (see [Fig. 4.12](#)). Here again, the optimized model shows the best overall predictions for torque and power coefficients over a wide range of speed ratios compared to experimental measurements.

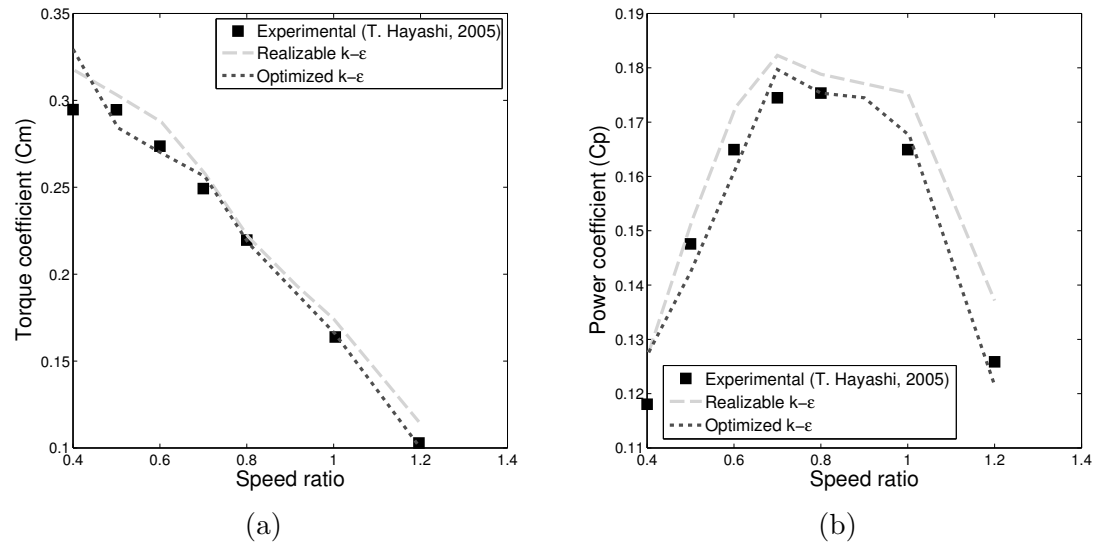


Figure 4.12: (a) Torque coefficient for the Savonius turbine (b) Power coefficient for the Savonius turbine.

Flow and turbulence in the wake of an airport terminal building were then investigated. The experimental data for this configuration was obtained from the QNET database. A simplified 2D profile of the terminal building was employed for the simulation, see Figure 4.8. This is a plausible simplification since the length of the building is much greater than its width and height. Furthermore, the surrounding area is well open with buildings of low heights.

The building is located near one of the runways of the airport. The influence of the building onto the runway was investigated. The velocity deficit and turbulence intensity excess, as well as velocity and kinetic energy profile over the runway, were analyzed for this purpose.

Simulations considering the computational domain with and without the building have been performed. This is important in order to quantify the influence of the building on the runway. Moreover, it allows to investigate the rate of production of turbulence caused by the building. In Fig. 4.13(a), the velocity on the runway at different heights is compared. The predictions of the realizable and the optimized model are almost identical. Both models deliver reasonable agreement for the velocity profile in the case without the building. However, they predict prematurely the reattachment of the flow behind the building, as shown in Fig. 4.13(a).

Both models also failed to predict the turbulent kinetic energy profiles for the simulated flows. Although the comparison of the k profile in Fig. 4.13(b) can not be done directly, because the experimental and the given boundary profiles for k obviously differ, the plot shows that the production of turbulent kinetic energy is four times higher in the CFD compared with the measured data. This confirms the well-documented excessive production of k by the $k-\epsilon$ model in flows with high

strain rates.

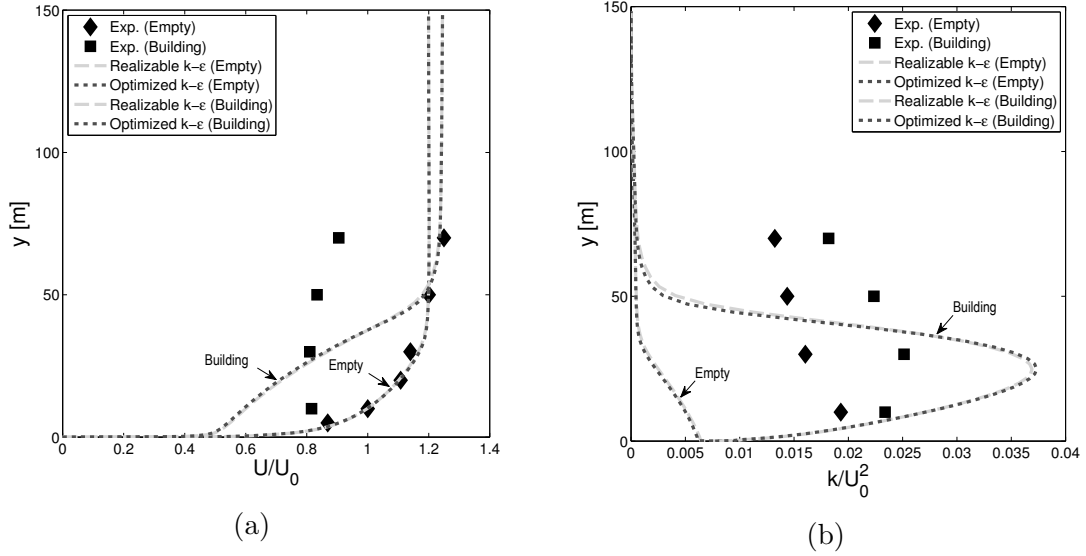


Figure 4.13: Plots of the flow around a building (a) Comparison of velocity profiles U/U_0 with experimental data. (b) Comparison of turbulent kinetic energy profiles k/U_0^2 with experimental data.

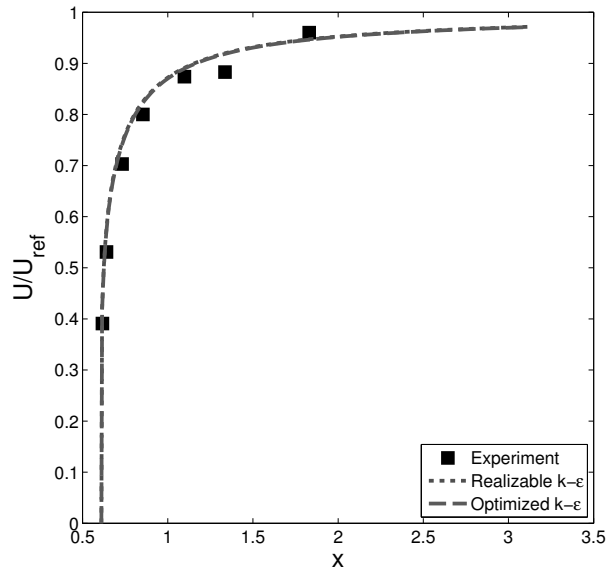


Figure 4.14: Comparison of the normalized velocity profile in the wake of an airfoil.

The incompressible flow around a conventional airfoil (DSMA661) at zero angle of incidence was simulated in a third step. The velocity profile in the wake of the airfoil was compared with the experimental data of Nakayama (1985) described in the ERCOFTAC database. Computational domain and boundary condition for the test case considered are shown in Figure 4.7.

Both turbulence models have been able to predict with an excellent accuracy the mean velocity in the wake of the airfoil. They lead to the same accuracy, as shown in Figure 4.14.

Another flow of practical importance but with very different turbulence properties is the flow through square ducts. A 3D simulation of a square duct with a 180° bend (depicted in Figure 4.9) was therefore performed in a last step. The streamwise velocity profile in the centerline of the duct at different angular positions was compared with the experimental data of Choi et al. (1989) contained in the ERCOFTAC database.

The flow pattern predicted by the realizable model with the standard constants and the optimized model are again almost identical for the streamwise velocity profiles at all angular positions, as can be seen in Figure 4.15.

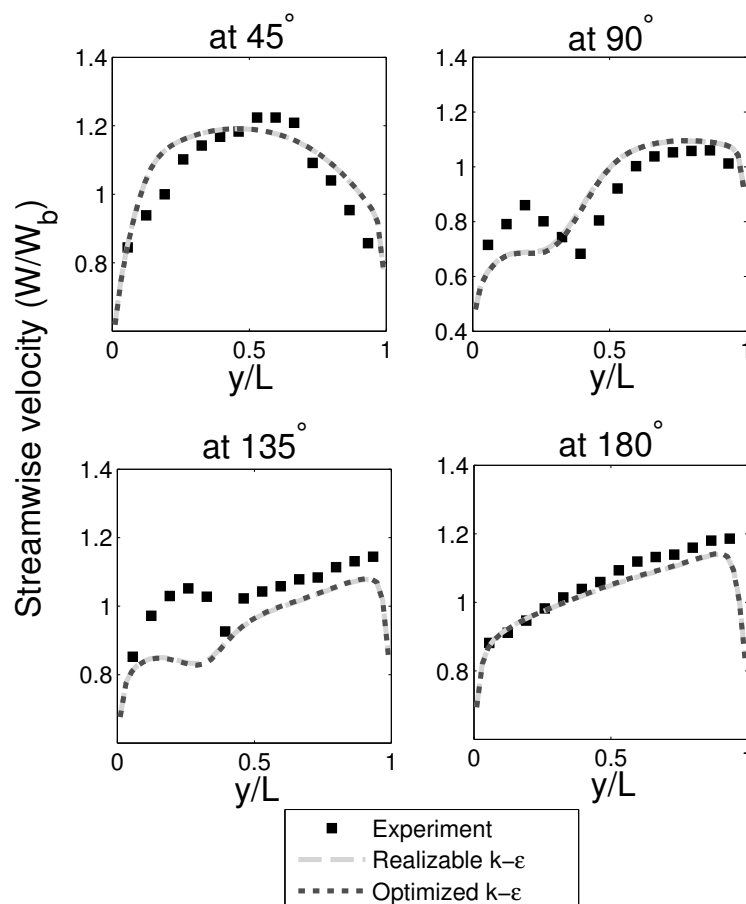


Figure 4.15: Comparison of streamwise velocity profiles at different angular positions.

4.10 Conclusions

The developed optimization methodology described here has been proved to be a valuable tool to improve the parameters of the realizable $k - \epsilon$ turbulence model. Slightly improved predictions were consistently obtained for all test cases considered, even though the optimized parameters do not differ much from the conventional values. The optimal parameter set has been afterwards tested for four independent configurations. The optimized model could predict the torque and power coefficients for the vertical-axis wind turbine with a better accuracy than the realizable $k - \epsilon$ model with the standard constants. For all other cases, it performs equally well. Limitations of the framework of the realizable $k - \epsilon$ still exist. In flows where the original model performs well, the optimization has improved the results, whereas in flows where the original results are qualitatively different, tuning of the coefficients is not helpful.

It is clear that the standard constants used in the realizable $k - \epsilon$ have been already well calibrated over decades and thus deliver robust results for a broad range of applications. Nevertheless, it has been shown that it is possible to fine tune further these parameters thanks to an efficient optimization methodology.

The suggested values for the realizable $k - \epsilon$ model constants are $C_{\epsilon 1} = 1.37$, $C_2 = 1.89$, $\sigma_k = 1.02$ and $\sigma_\epsilon = 1.14$. Employing these parameters does not lead to any increase in computational cost, but should lead to a slightly improved or at least to the same level of accuracy. These optimized values will be employed for the reactor simulations in chapter 6.

Chapter 5

Model optimization for chemical reactions using global model structure

This chapter is written based on the following paper:

L. G. M. de Souza, H. Haida, D. Thévenin, A. Seidel-Morgenstern, G. Janiga. Model selection and parameter estimation for chemical reactions using global model structure, (2013). *Computers and Chemical Engineering* (58), 269-277.

5.1 Introduction

In chemical kinetics studies, usually after the determination of the reaction network, several kinetic models are investigated in order to characterize the reaction kinetics with the best possible accuracy. Each model describes a different possible mechanism. Hence, the selection of one specific model induces also the choice of a particular mechanism ([Warnatz et al. \(2006\)](#)).

In complex reaction systems such as those found in heterogeneous catalytic reactions, the number of plausible models is very large. This is even the case for systems with a relatively small number of reactions and components ([Xu et al. \(1988\)](#)). Considering the different possible model concepts, e.g., Eley-Rideal (ER), Mars-Van Krevelen (MVK), Langmuir-Hinshelwood and Hougen-Watson (LHHW) and different mechanisms for adsorption of reactants and products, the investigation of all possible kinetic models constitutes a formidable task. Therefore, only a restricted subset of models are usually evaluated in detail ([Ozdemir and Gultekin \(2009\)](#); [Marvast et al. \(2011\)](#)).

Often, the rivaling models are analyzed separately or sequentially. The latter practice is particularly useful in the case of complex reaction networks. Nevertheless,

the investigation of a very large number of models is usually too time-consuming as the parameter estimation needs to be performed for each model.

In most cases the values for all kinetic parameters, such as activation energies, are reported in the literature with a prescribed level of precision. However, some kinetic constants may be poorly known and the documented values may span several orders of magnitude in some cases.

In the present work, a global search within the plausible models and parameter sets has been developed. For this purpose, the formulation of a general and flexible global model is important. This superstructure model involves real-value and discrete-value parameters, where the real-value parameters describe the kinetic parameters and the discrete-value parameters are related to different model concepts and reaction orders.

The genetic algorithm NSGA-II implemented in the software modeFrontier 4.2.1 (ESTECO s.p.a., Italy) is applied for the optimization. The original NSGA-II algorithm has been developed by [Deb et al. \(2002\)](#). With this algorithm it is possible to treat continuous (real-coded) and discrete (binary-coded) variables simultaneously. The kinetic coefficients and model mechanisms are simultaneously considered as decision variables. This allows an automatic global search within a large number of possible reaction mechanisms.

Superstructure-based optimization has already been applied to other problems in chemical engineering, mostly for the determination of optimal process structures and process parameters (e.g., [Yeomans and Grossmann \(1999\)](#); [Kawajiri and Biegler \(2006\)](#); [Kaspereit et al. \(2012\)](#)). Process optimization with a view toward control has been also extensively considered (e.g., [Schwerin et al. \(2000\)](#)). In the majority of these cases the optimization problems were solved using Mixed-Integer Non-Linear Programming (MINLP). However, in cases where the parameters are not known with a sufficient precision (as in reaction kinetics) a global search appears to be a more robust technique.

The distinct treatment of real-value and discrete-value parameters in the GA is crucial for the efficiency of the optimization algorithm when solving mixed-integer optimization problem. As pointed out by [Elliott et al. \(2004\)](#), binary encoding may affect negatively the quality of the result when applied to multi-dimensional optimization problems, this being the rule for reaction parameter optimization. As a result, premature convergence of the population to a non-global optimum, slow convergence rate and difficulties to reach fine local tuning have been documented. The observed difficulties in performing local tuning when using binary encoding arise mainly because of the Hamming cliff effect ([Elliott et al. \(2004\)](#)).

The real-coded or floating-point (FP) implementation makes it possible to apply

the optimization to larger domains without sacrificing precision. Another benefit is the possibility to perform local tuning in the objective space. Real encoding produces in general better results for numerical optimization than binary encoding (Michalewicz (1996)). On the other hand, the real-coded or floating-point genes are not the optimal treatment for discrete variables as they require truncations and rounding procedures. Therefore, the best approach for solving mixed-integer optimization problems using GA is to consider a distinct formulation for the binary-coded and for the real-coded variables.

This is the approach retained in the present study. The binary-coded variables are treated using the classical genetic operators for binary encoding, while for the real-valued variables the Simulated Binary genetic operators proposed by Deb and Agarwal (1995) are applied, avoiding the typical drawbacks of coding real-valued variables in finite length strings.

The methodology developed in Chapter 3 is applied to the model optimization of the partial oxidation of the ethane reaction network (Joshi (2007)). The robustness of the automated methodology and the quality of the obtained results are compared with that presented in Joshi (2007), where an exhaustive and time-consuming analysis of hundreds of models have been performed manually. However, the optimization procedure in Joshi (2007) did not include the model parameters (discrete-value variables) and the optimization was performed only for the kinetic parameters (real-valued variables). The present work is therefore considerably more general.

5.2 Generalized kinetic model for heterogeneous catalytic reactions

The formulation of a general and flexible global model is an important point for the elaboration of a procedure allowing an automatic search within the possible models and parameter sets. The generalized model is able to describe the different mechanisms possible with the Eley-Rideal (ER) and the Langmuir-Hinshelwood Hougen-Watson model (LHHW). Considering an irreversible heterogeneous catalyzed reaction $A + B \xrightarrow{r_j} C + D$, a generalized kinetic model expression can be written as follows:

$$r_j = \frac{k_{j,\infty} \exp\left(\frac{-E_{A,j}}{RT}\right) (K_A p_A)^{\alpha_A} (K_B p_B)^{\alpha_B}}{\left(1 + \sum_i^N \phi_i^I (K_i p_i)^{\alpha_i}\right)^{\gamma^I} \left(1 + \sum_i^N \phi_i^{II} (K_i p_i)^{\alpha_i}\right)^{\gamma^{II}}} \quad (5.1)$$

The generalized model contains kinetic parameters and model parameters. The kinetic parameters are continuous variables, while the model parameters are repre-

sented by discrete variables.

In Eq. (5.1), the pre-exponential factor $k_{j,\infty}$, the activation energy $E_{A,j}$ and the adsorption equilibrium constant K_i are the kinetic parameters for all reactions ($j = 1, \dots, M$) and species ($i = 1, \dots, N$) involved. They are free adjustable parameters within an appropriate physical range. The constants \tilde{R} and T are the universal gas constant and the temperature, respectively.

Different reaction mechanisms can be represented by the model parameters α_i , ϕ_i^I , ϕ_i^{II} , γ^I and γ^{II} . For instance, the exponents α_i describe either molecular or dissociative adsorption. Setting $\alpha_i = 1$ corresponds to choosing molecular adsorption while setting $\alpha_i = 0.5$ means a dissociative adsorption. Each reactant and product can adsorb according to a different mechanism.

The components may adsorb on the catalyst surface and inhibit the reaction rate. This is taken into account through the switching parameters ϕ_i^I and ϕ_i^{II} . The values allowed for these parameters are either 1 or 0, meaning that the component is adsorbed or not, respectively. In order to account for non-competitive adsorption mechanism, the values of ϕ_i^I and ϕ_i^{II} are set to be always opposite. In this manner components appearing in one site will not appear on another site. Nevertheless, the generalized model also accounts for competitive adsorption.

The exponents γ^I and γ^{II} allow to account for single and dual-sites. The values for the parameter γ^I is either 1 or 2 and the values for the parameter γ^{II} is 0 or 1. For example, if $\gamma^I = 1$ and $\gamma^{II} = 1$, the non-competitive dual-site mechanism is enabled. Alternatively, if $\gamma^I = 2$ and $\gamma^{II} = 0$ the competitive dual-site mechanism is considered.

Although it does not rely on a completely rigorous derivation, Eq. (5.1) offers a general structure for the generation of a large amount of different mechanisms found in the reaction engineering literature. The described model parameters and mechanisms are summarized in Table 5.1.

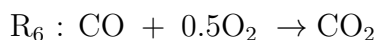
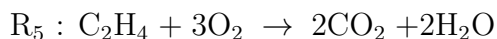
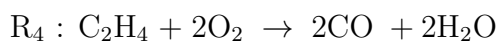
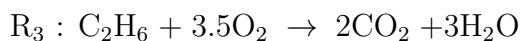
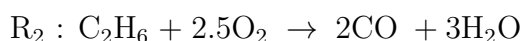
Table 5.1: Description of the model parameters and mechanisms.

Parameter Values	Description
$\alpha_i = \begin{cases} 1 \\ 0.5 \end{cases}$	$\alpha_i = 1$ (Molecular adsorption) $\alpha_i = 0.5$ (Dissociative adsorption)
$\phi_i^I = \begin{cases} 0 \\ 1 \end{cases}$	$\phi_i^I = 0$ (Not Adsorbed) $\phi_i^I = 1$ (Adsorbed)
$\phi_i^{II} = \begin{cases} 0 \\ 1 \end{cases}$	$\phi_i^{II} = 0$ (Not Adsorbed) $\phi_i^{II} = 1$ (Adsorbed)
$\gamma^I = \begin{cases} 1 \\ 2 \end{cases}$	<i>if</i> $(\gamma^I + \gamma^{II}) = 1$ (Single-Site)
$\gamma^{II} = \begin{cases} 0 \\ 1 \end{cases}$	<i>if</i> $(\gamma^I + \gamma^{II}) = 2$ (Dual-Site)

5.3 System under investigation

The developed methodology has been applied to the partial oxidation of ethane reaction network. This system has been previously studied experimentally within a collaborative research group at the University of Magdeburg using a supported vanadium oxide catalyst in a laboratory-scale fixed bed reactor ([Seidel-Morgenstern \(2010\)](#)). A wide range of experimental conditions have been investigated. With these results, a reaction network has been proposed. All these results have been documented in [Joshi \(2007\)](#).

Based on this study, the finally proposed network consisted of 6 reactions and 6 components ([Klose et al. \(2004\)](#)):



The rank of the corresponding stoichiometric matrix is 3, indicating that three key components are sufficient to represent the system. Knowing the partial pressure of these components it is possible to obtain the partial pressure of all the components present in the system.

In [Joshi \(2007\)](#), an exhaustive and time-consuming fitting procedure has been performed for hundreds of different models. Much less models are usually investigated

in the scientific literature. Therefore, an automated and robust approach would be very useful to derive as efficiently as possible optimal reaction networks for complex systems.

The parameters for the ethane oxidation and its intermediates ethylene and CO were estimated in Joshi (2007) with a stepwise manner, e.g., (i) at first kinetic parameters have been estimated only for CO oxidation (reaction R_6), considering 60 models; (ii) in a second step kinetic parameters were estimated for 244 models in order to describe the ethylene oxidation (reactions R_4 , R_5 and R_6) and (iii) the parameters for the whole ethane oxidation reaction network were estimated (reactions R_1 to R_6), keeping fixed the parameters already estimated in reactions R_4 , R_5 and R_6 ; finally, 344 models have been evaluated in this last step. As discussed in Joshi (2007), the parameter estimation for the ethane oxidation network has been carried out using the pattern search method and the Levenberg-Maquardt method, considering always a single objective function.

In the present work, ethane oxidation is still described by the 6 reactions discussed previously. However, the parameter estimation is now obtained for the whole network in a single step using multi-objective optimization. Thus, a stepwise, tedious and error-prone approach is not required anymore. The developed, automatic methodology for model and parameter optimization is presented in what follows. More details about the investigated system can be found in Joshi (2007).

The same experimental data is used for the fitting of the complete ethane network as in Joshi (2007). The data set contains $N_{\text{exp}} = 533$ experimental points with temperature varying from 460°C to 610°C . Different volumetric flow rates and catalyst mass have been used but keeping a constant gas hourly space velocity (GHSV). The inlet concentrations of ethane and oxygen have been varied as well.

5.3.1 Modeling

In order to obtain results comparable with those of Joshi (2007), the same simplification has been adopted, where the individual reaction rates (r_j) were expressed as function of the averaged partial pressures. This is a realistic assumption considering the small dimensions of the system and low conversion levels of ethane in a diluted feed stream. This also led to nearly isothermal conditions in the reactor. Moreover, since only powder catalysts have been used, the intra-particle mass transfer is not a limiting factor (Seidel-Morgenstern (2010)). A Matlab code was written taking into account these simplifications.

The modeled net rate of production of a component (Marin and Yablonsky (2011)) is related to the individual reaction rates r_j and the stoichiometric coefficient v_{ij} as follows:

$$R_i = \sum_j^M v_{ij} r_j \quad i = 1, \dots, N \quad (5.2)$$

The individual reaction rates r_j can not be measured in the experiments. Nevertheless, the net rate of production of a component can be calculated by the following equation:

$$R_i^{\text{exp}} = \frac{p_i^{\text{in}} - p_i^{\text{out}}}{m_{\text{cat}} \tilde{R} T} \dot{V} \quad (5.3)$$

where p_i^{in} and p_i^{out} are the partial pressure at the inlet and outlet, respectively \dot{V} is the volumetric flow-rate, m_{cat} is the mass of the catalyst and \tilde{R} and T are the universal gas constant and the temperature, respectively. The overall reaction rate has dimensions $\text{mol.kg}_{\text{cat}}^{-1}.\text{h}^{-1}$.

In this manner the overall reaction rates delivered by experiments and simulation can be compared.

5.4 Reparametrization

The effective rate constant k_j^{eff} has been introduced in order to reduce the well known, strong correlation between the pre-exponential factor $k_{j,\infty}$ and the activation energy E_A in Equation (5.1). The reparametrized Arrhenius equation reads:

$$k_j^{\text{eff}} = k_{j,\text{ref}}^{\text{eff}} \exp \left[\frac{-E_{A,j}}{\tilde{R}} \left(\frac{1}{T} - \frac{1}{T_{\text{ref}}} \right) \right] \quad (5.4)$$

the reference temperature is given by the center of the experimental range as follows,

$$T_{\text{ref}} = \frac{1}{2} (T_{\text{min}} + T_{\text{max}}) \quad (5.5)$$

and $k_{j,\text{ref}}^{\text{eff}}$ is defined as,

$$k_{j,\text{ref}}^{\text{eff}} = k_{j,\infty} \exp \left(\frac{-E_{A,j}}{\tilde{R} T_{\text{ref}}} \right) \quad (5.6)$$

5.5 Optimization methodology

The optimization procedure developed in this work can be applied in principle to many different heterogeneous catalytic reaction systems. For the case considered here, the mixed-integer (Bertsimas and Weismantel (2005)), multi-objective, concurrent optimization can be formally written in the following manner:

$$\min OF \left(k_j^{eff}, E_{A,j}, K_i, \alpha_i, \phi_i^I, \phi_i^{II}, \gamma^I, \gamma^{II}, p_{i,k}, T_k \right)_{i=C_2H_6, C_2H_4, CO_2}^{OLS} \quad (5.7)$$

subjected to: Real-value constraints:

$$k_j^{eff} \in [k_{j,min}^{eff}, k_{j,max}^{eff}] \quad j = 1, \dots, M \quad (5.8)$$

$$E_{A,j} \in [E_{A,j,min}, E_{A,j,max}] \quad j = 1, \dots, M \quad (5.9)$$

$$K_i \in [K_{i,min}, K_{i,max}] \quad i = 1, \dots, N \quad (5.10)$$

Discrete-value constraints:

$$\alpha_i \in \{0.5, 1\} \quad i = 1, \dots, N \quad (5.11)$$

$$\phi_i^I \in \{0, 1\} \quad i = 1, \dots, N \quad (5.12)$$

$$\gamma^I \in \{1, 2\} \quad (5.13)$$

$$\gamma^{II} \in \{0, 1\} \quad (5.14)$$

$$(\gamma^I + \gamma^{II}) \leq 2 \quad (5.15)$$

Note that 3 concurrent objective functions ($OF_{C_2H_6}^{OLS}$, $OF_{C_2H_4}^{OLS}$ and $OF_{CO_2}^{OLS}$) need to be minimized simultaneously. This treatment is adopted as an alternative to the traditional stepwise parameter estimation procedures used in chemical reaction networks (Joshi (2007); Jiang et al. (2010); Stewart et al. (1992)).

Altogether, 29 decision variables are considered for the optimization. The kinetic coefficient parameters are represented using 17 real-value decision variables, and the model parameters are further associated to 12 discrete-value decision variables. A constraint, $(\gamma^I + \gamma^{II}) \leq 2$, is added to the problem so that only single-site and dual-site are allowed to exist.

Since H_2O appears only as a product and no reliable measurements concerning its partial pressure are available, this component was not included in the rate expressions, reducing the considered number of species to $N = 5$.

The real-value decision variables for the ethane reaction network consist of 6 effective rate constants k_j^{eff} , 6 activation energies $E_{A,j}$ and 5 adsorption equilibrium constants K_i . The feasible range retained for the kinetic parameters were chosen around the optimal values found by Joshi (2007) but keeping a wide range of possible variations.

For the reaction network finally considered ($N = 5$ components) the number of discrete-value variables α_i , ϕ_i^I and $\gamma^{I,II}$ sum up to 12. The parameters ϕ_i^{II} are not directly included as design parameters, as their values depend on the values of ϕ_i^I according to the following conditional expression:

$$\phi_i^{II} = \begin{cases} 0 & \text{if } \phi_i^I = 1 \\ 1 & \text{if } \phi_i^I = 0 \end{cases} \quad (5.16)$$

The objective functions are calculated using the ordinary least-square (OLS) difference between the values of the experimental overall reaction rate R_i^{exp} and the modeled one R_i^{model} . Objective functions were evaluated for the three accurately measurable key components: Ethane, Ethylene and Carbon Dioxide. They can be written as follows:

$$OF(\theta, p_{i,k}, T_k)_{C_2H_6}^{OLS} = \sum_{k=1}^{N_{exp}} \left(R_{C_2H_6,k}^{exp} - R(\theta, p_{C_2H_6,k}, T_k)_{C_2H_6,k}^{model} \right)^2 \quad (5.17)$$

$$OF(\theta, p_{i,k}, T_k)_{C_2H_4}^{OLS} = \sum_{k=1}^{N_{exp}} \left(R_{C_2H_4,k}^{exp} - R(\theta, p_{C_2H_4,k}, T_k)_{C_2H_4,k}^{model} \right)^2 \quad (5.18)$$

$$OF(\theta, p_{i,k}, T_k)_{CO_2}^{OLS} = \sum_{k=1}^{N_{exp}} \left(R_{CO_2,k}^{exp} - R(\theta, p_{CO_2,k}, T_k)_{CO_2,k}^{model} \right)^2 \quad (5.19)$$

where $N_{exp} = 533$ is the number of experimental observations for the data set considering the full ethane reaction network.

Taking into account all the possible combinations of the discrete model parameters, a total of 1544 different models can be derived for this specific system from the generalized kinetic model. The optimization algorithm searches within all these possible models, simultaneously estimating the best set of kinetic parameters for the studied system.

Table 5.2: Settings employed for the optimization algorithm NSGA-II.

Settings for NSGA-II	
Number of Generations	40
Initial Population	290
Total Number of Designs	11600
Crossover Probability [0.0, 1.0]	0.9
Mutation Probability [0.0, 1.0]	1.0

Details about the NSGA-II settings are shown in Table 5.2. Standard values have been adopted for the genetic operators. The Uniform Latin Hypercube distribution

has been used for the generation of the initial population. An automatic scaling for the mutation probability is implemented, increasingly stabilizing the population at each generation by decreasing the mutation amplitude. The total computing time for the complete optimization process using a standard desktop PC (Intel Core i5-2500, 3.30 GHz, 8 GB RAM, 64 bit) is about 120 minutes.

The optimization procedure has been implemented using the commercial software modeFrontier 4.2.1 (ESTECO s.p.a., Italy) while the model evaluation has been coded in Matlab R2011a (The Mathworks Inc., Natick, Massachusetts, USA). The Matlab integration mode in modeFrontier has been used for a fast connection between both softwares. The optimization loop is showed in Fig. 5.1.

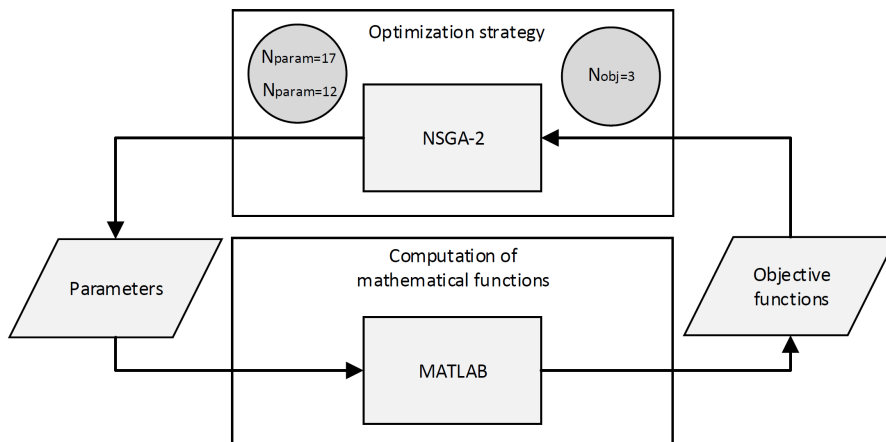


Figure 5.1: Diagram showing the optimization loop.

5.6 Results and discussions

A selected region of the obtained Pareto solutions (corresponding to $\rho_i^2 > 0.90$) is shown as a 3-D scatter plot in Fig. 5.2. For the sake of comparison, the optimal solution obtained by Joshi (2007) using a manual procedure is also plotted (black circle). It can be seen from Fig. 5.2 that the Pareto solutions obtained with the automatic procedure presented in this work are, in terms of Pareto optimality, of the same quality as the optimal solution found manually by Joshi (2007).

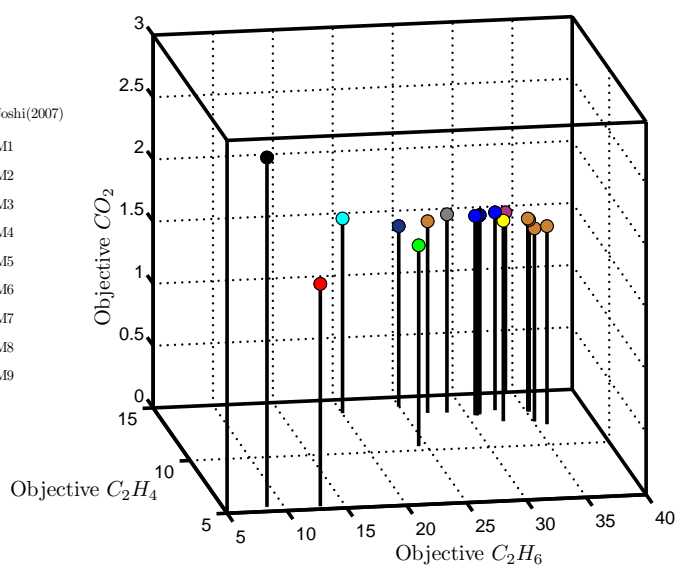


Figure 5.2: 3-D scatter plot from a selected region of the Pareto solution showing the values of the three objective functions, Eqs.(5.17) to (5.19).

However, the automatic optimization is completed within 120 minutes and can be immediately applied to different systems, while a manual approach requires months of error-prone comparisons for the same level of quality.

The selected region of the Pareto front contains indeed 17 designs. However, only nine distinct models (M1 to M9, represented by colors in Fig. 5.2) finally remain in Fig. 5.2 when looking at the underlying model parameters (Fig. 5.3). The reason for that is the presence of solution clusters. One classical issue associated to multi-objective optimization algorithms is to avoid clustered regions in order to obtain a uniformly distributed representation of the Pareto front.

An analysis of the model parameters for (M1, . . . , M9) shows that all these models share some common features. For instance, the dual-site and competitive adsorption mechanisms are used identically by all the selected designs, as shown in Fig. 5.3. Nevertheless, the models (M1, . . . , M9) represent a great variety of underlying mechanisms. Joshi's optimal model and the model M7 rely on the same mechanisms, but use a quite distinct parameter set, as shown when plotting the coordinates in a parallel coordinate diagram (Fig. 5.4).

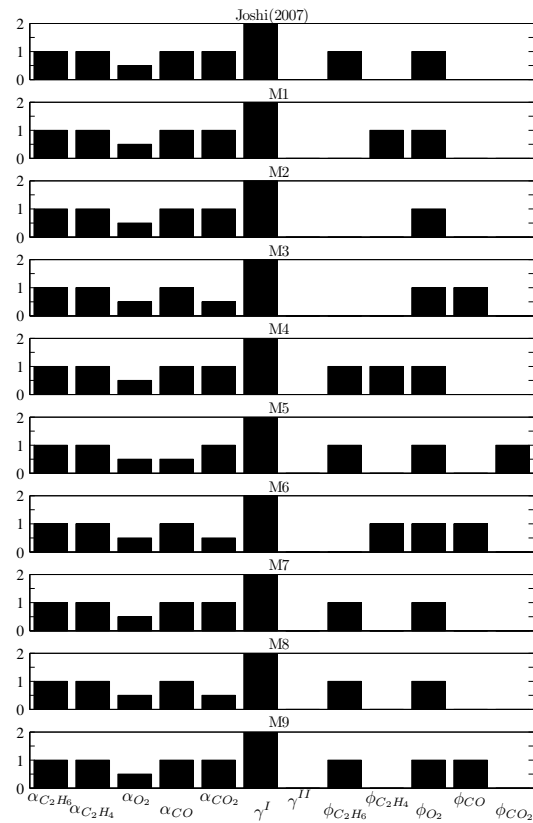


Figure 5.3: Model parameters for the models (M1,...,M9) associated to the optimal solutions shown in Fig. 5.2.

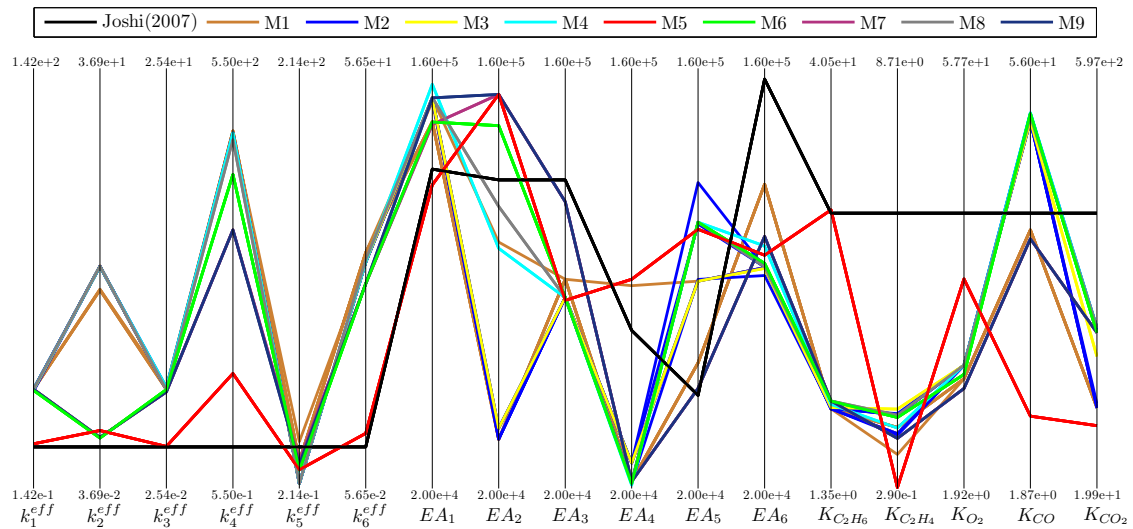


Figure 5.4: Parallel coordinate plot showing the kinetic parameters for the selected solutions.

Very often in practice, a single optimal design is chosen more or less arbitrarily by the user from the set of non-dominated solutions. As a better alternative, the

coefficient of determination (ρ_i^2) is a meaningful statistical property to differentiate between alternative models and is therefore applied here as additional decision-maker.

The definition of ρ_i^2 reads:

$$\rho_{i=C_2H_6, C_2H_4, CO_2}^2 = 1 - \frac{OF(\theta, p_{i,k}, T_k)_i^{OLS}}{\sum_{k=1}^{N_{\text{exp}}} \left(R_{i,k}^{\text{exp}} - \frac{1}{N_{\text{exp}}} \sum_{i=1}^{N_{\text{exp}}} R_{i,k}^{\text{exp}} \right)^2} \quad (5.20)$$

It is important to find an optimal solution with a good compromise between all the 3 objectives, Eqs. (5.17) to (5.19). Therefore, only solutions with all $\rho_i^2 > 0.90$ were retained in Fig. 5.2. The solution M5 (red color, Fig. 5.2) corresponds to the design with the highest averaged value of ρ_i^2 . Another optimal solution, M6 (green color) has also been included for further comparisons, using as criterion the "best of the worst" strategy, i.e., maximizing for the worst objective.

The parallel coordinate plot in Fig. 5.4 shows the kinetic parameter values for the selected designs. Each polyline represents one different optimal design, including along the horizontal axis all the 17 real-value design variables simultaneously. The lower and upper bound values considered in the optimization are shown in the parallel plot for each parameter (vertical axes). The optimal parameters found by the present optimization differ considerably depending on the specific model (look at the range covered). Furthermore, they are indeed quite different from the values retained by Joshi (2007), solution plotted in black in Fig. 5.4.

The objective functions and the ρ_i^2 values for the optimal solutions are summarized in Table 5.3. Remember that the $OF(\theta, p_{i,k}, T_k)_i^{OLS}$ values must be minimized while the ρ_i^2 values should be maximized. It is again visible that the solution obtained manually by Joshi (2007) is of high quality and belongs to the Pareto set. However, the solutions corresponding to models M5 and M6 (Table 5.4) obtained automatically and within a short computational time are equally optimal in the sense of Pareto. The parity plots obtained with the three models and shown in Fig. 5.5 confirm this statement.

Table 5.3: Objective functions (OF_i^{OLS}) and coefficient of determination (ρ_i^2) values for the selected optimal solutions M5 and M6.

	Joshi (2007)	M5	M6
$OF(\theta, p_{i,k}, T_k)_{C_2H_6}^{OLS}$	8.5955	12.9420	24.3331
$OF(\theta, p_{i,k}, T_k)_{C_2H_4}^{OLS}$	5.4134	5.2537	10.4000
$OF(\theta, p_{i,k}, T_k)_{CO_2}^{OLS}$	2.8121	1.7901	1.6155
$\rho_{C_2H_6}^2$	0.9762	0.9642	0.9327
$\rho_{C_2H_4}^2$	0.9640	0.9650	0.9307
$\rho_{CO_2}^2$	0.8730	0.9192	0.9270

As it is shown by the Pareto plot in Fig. 5.2, it is not possible to obtain an improvement in any of the objectives without impacting negatively at least one of the concurrent objectives. For example, comparing with Joshi’s model the solution M5 shows better OF_i^{OLS} for two of the objectives, but loses for the third objective (check the values in Table 5.3). The coefficient of determination (ρ_i^2) may give a better idea about the quality of the solutions (see again Table 5.3). One may notice, for instance, that M5 and M6 present $\rho_i^2 > 0.919$ for the three objectives, which is not the case of Joshi’s solution.

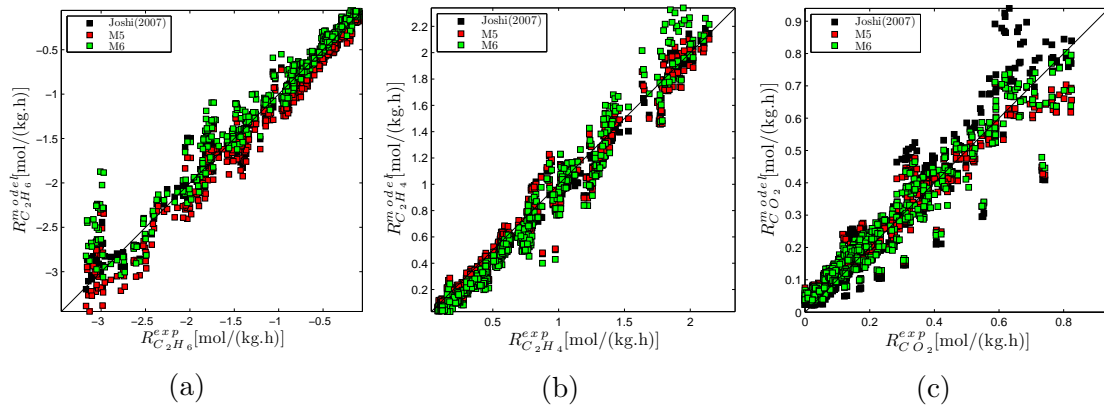


Figure 5.5: Parity plot for the net rate of production of (a) C_2H_6 , (b) C_2H_4 and (c) CO_2 for the 533 experimental points.

Table 5.4: Reaction rate equations for the optimal model of Joshi (2007) and for the selected optimal models M5 and M6.

Model	Reaction Rate
Joshi (2007)	denominator $r_1 \dots r_6$ $\left(1 + K_{C_2H_6} p_{C_2H_6} + (K_{O_2} p_{O_2})^{0.5}\right)^2$ numerator $\begin{array}{ll} r_1 & r_2 \\ k_1^{eff} \left(\frac{-E_{A,1}}{RT}\right) K_{C_2H_6} p_{C_2H_6} (K_{O_2} p_{O_2})^{0.5} & k_2^{eff} \left(\frac{-E_{A,2}}{RT}\right) K_{C_2H_6} p_{C_2H_6} K_{O_2} p_{O_2}^{0.5} \\ r_3 & r_4 \\ k_3^{eff} \left(\frac{-E_{A,3}}{RT}\right) K_{C_2H_6} p_{C_2H_6} (K_{O_2} p_{O_2})^{0.5} & k_4^{eff} \left(\frac{-E_{A,4}}{RT}\right) K_{C_2H_4} p_{C_2H_4} (K_{O_2} p_{O_2})^{0.5} \\ r_5 & r_6 \\ k_5^{eff} \left(\frac{-E_{A,5}}{RT}\right) K_{C_2H_4} p_{C_2H_4} (K_{O_2} p_{O_2})^{0.5} & k_6^{eff} \left(\frac{-E_{A,6}}{RT}\right) K_{CO} p_{CO} (K_{O_2} p_{O_2})^{0.5} \end{array}$
M5	denominator $r_1 \dots r_6$ $\left(1 + K_{C_2H_6} p_{C_2H_6} + (K_{O_2} p_{O_2})^{0.5} + K_{CO} p_{CO}\right)^2$ numerator $\begin{array}{ll} r_1 & r_2 \\ k_1^{eff} \left(\frac{-E_{A,1}}{RT}\right) K_{C_2H_6} p_{C_2H_6} (K_{O_2} p_{O_2})^{0.5} & k_2^{eff} \left(\frac{-E_{A,2}}{RT}\right) K_{C_2H_6} p_{C_2H_6} K_{O_2} p_{O_2}^{0.5} \\ r_3 & r_4 \\ k_3^{eff} \left(\frac{-E_{A,3}}{RT}\right) K_{C_2H_6} p_{C_2H_6} (K_{O_2} p_{O_2})^{0.5} & k_4^{eff} \left(\frac{-E_{A,4}}{RT}\right) K_{C_2H_4} p_{C_2H_4} (K_{O_2} p_{O_2})^{0.5} \\ r_5 & r_6 \\ k_5^{eff} \left(\frac{-E_{A,5}}{RT}\right) K_{C_2H_4} p_{C_2H_4} (K_{O_2} p_{O_2})^{0.5} & k_6^{eff} \left(\frac{-E_{A,6}}{RT}\right) (K_{CO} p_{CO})^{0.5} (K_{O_2} p_{O_2})^{0.5} \end{array}$
M6	denominator $r_1 \dots r_6$ $\left(1 + K_{C_2H_4} p_{C_2H_4} + (K_{O_2} p_{O_2})^{0.5} + K_{CO} p_{CO}\right)^2$ numerator $\begin{array}{ll} r_1 & r_2 \\ k_1^{eff} \left(\frac{-E_{A,1}}{RT}\right) K_{C_2H_6} p_{C_2H_6} (K_{O_2} p_{O_2})^{0.5} & k_2^{eff} \left(\frac{-E_{A,2}}{RT}\right) K_{C_2H_6} p_{C_2H_6} (K_{O_2} p_{O_2})^{0.5} \\ r_3 & r_4 \\ k_3^{eff} \left(\frac{-E_{A,3}}{RT}\right) K_{C_2H_6} p_{C_2H_6} (K_{O_2} p_{O_2})^{0.5} & k_4^{eff} \left(\frac{-E_{A,4}}{RT}\right) K_{C_2H_4} p_{C_2H_4} (K_{O_2} p_{O_2})^{0.5} \\ r_5 & r_6 \\ k_5^{eff} \left(\frac{-E_{A,5}}{RT}\right) K_{C_2H_4} p_{C_2H_4} (K_{O_2} p_{O_2})^{0.5} & k_6^{eff} \left(\frac{-E_{A,6}}{RT}\right) K_{CO} p_{CO} (K_{O_2} p_{O_2})^{0.5} \end{array}$

Although the quality of the results obtained with the three models (Joshi (2007); M5; M6) is very similar, there are significant differences in the structure of these models. The main difference lies in the formulation of the denominators for the rate equations. All three selected models consider competitive adsorption with dissociative adsorption of oxygen. The component C_2H_6 is assumed to adsorb on the catalyst surface in Joshi's model as well as in M5. In fact, M5 becomes very similar to Joshi's model in the case of very small concentrations of CO_2 . At the opposite, a quite distinct mechanism is assumed in M6, for which C_2H_6 does not adsorb on the surface of the catalyst, while C_2H_4 and CO act as inhibitor for the reaction rate.

The optimal kinetic parameters of the three selected models differ considerably (Fig. 5.4). The optimal values of the activation energies (E_A) for Joshi’s model, M5 and M6 are compared directly in Table 5.5.

Table 5.5: Values of the $E_{A,j}$ parameters for the optimal model of Joshi (2007) and for the selected optimal models M5 and M6.

Parameter	Joshi (2007)	M5	M6
$E_{A,1}$	126441.1	121162.6	142108.5
$E_{A,2}$	122839.2	151383.6	140889.9
$E_{A,3}$	122839.2	82698.56	83620.52
$E_{A,4}$	72693.76	89725.68	21646.98
$E_{A,5}$	51026.79	106382.5	108709.5
$E_{A,6}$	156414.9	97726.88	95021.34

5.7 Conclusions

The developed methodology appears to be a very effective way to evaluate and to identify complex reaction mechanisms in an automatic and flexible manner. For the system investigated in this study, the quality of the results finally obtained is similar to that obtained by Joshi (2007) using a tedious and error-prone manual optimization during many months. While recognizing clearly the quality of the solution found in Joshi (2007), which is one prominent member of the optimal Pareto set, the present methodology allows the investigation of a much larger number of plausible model mechanisms in a fully automatic manner and has been completed in two hours on a standard PC.

The developed optimization framework is very flexible, so that it could be easily applied to any other heterogeneous catalytic reaction system as well as to further mechanisms. To the knowledge of the authors this is the first time that a superstructure-based automatic optimization has been applied to optimize kinetic models for a catalytic system.

Chapter 6

Simulation of a multiphase chemical reactor

In this chapter, a crystallization reactor is investigated. The simulation of this complex multiphase system involves distinct modeling levels, e.g., the fluid dynamics, the particle properties evolution and the crystallization kinetics.

The methodology developed to simulate polydisperse multiphase flows described in Chapter 2, as well as the distribution reconstruction technique of Section 2.4 are employed. Furthermore, the optimized RANS turbulence model (see Chapter 3 and Chapter 4) is also applied. Details on the growth kinetics are elaborated in this chapter.

The simulation of phenomena with very different time and length scales leads to further complexities. Therefore, a methodology to track the particle properties evolution while considering a detailed fluid dynamics description has been established. Details on simulation and methods are discussed in the next sections.

6.1 Crystallization: a multiscale problem

Crystallization refers to the process of formation of solid crystals from a solution. During crystallization mass transfer occurs from the liquid solution to the pure solid crystalline phase. Crystallization is widely employed as a separation and purification technique for the production of a variety of chemical, e.g., pharmaceutical, agricultural, flavor, fragrances and other chiral products.

In order for crystallization to occur, the solution should be supersaturated. The supersaturation is the difference between the existing concentration and the solubility concentration at a given temperature. The supersaturation is the driving force for the crystal growth and nucleation; depending on the supersaturation degree one of these mechanisms will be dominant. For a well-controlled crystal growth, it is

essential to know the solubility curve and the width of the so-called “metastable zone” (see Fig. 6.1), which is the region adjacent to the solubility curve where the crystal growth is assumed to be the dominant mechanism.

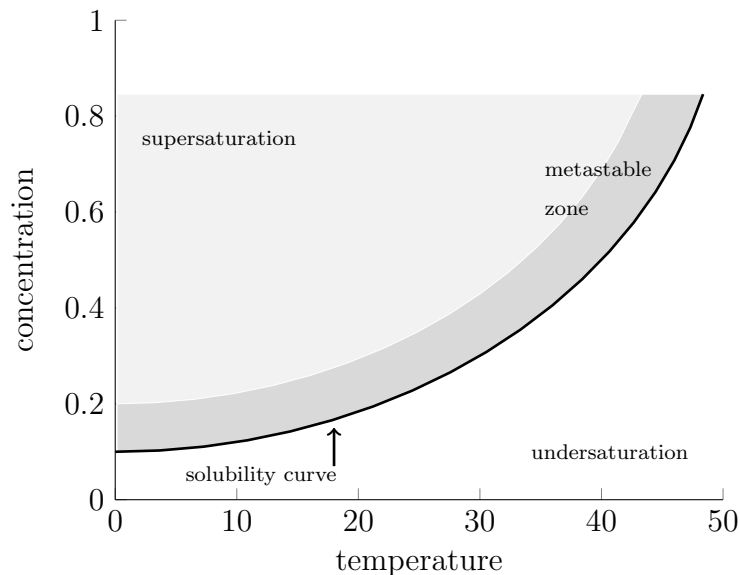


Figure 6.1: Illustrative solubility curve. Also showed in the figure: undersaturation, supersaturation and metastable zone.

In a crystallization process, the particle size and crystal shape are import criteria to evaluate the final quality of the product. The particles may undergo several phenomena, e.g., nucleation, growth, aggregation, breakage, which are directly influenced by the local flow condition. The accurate description of these phenomena involves the following modeling levels (or subproblems), see [Kulikov \(2010\)](#):

1. The fluid dynamics subproblem, which describes the particle transport in the reactor, as well as the local flow properties, e.g., slip velocities, turbulent kinetic energy.
2. The population balance subproblem, which describes the particles properties evolution.
3. The crystallization kinetics subproblem, which describes the nucleation and growth rate of the crystals.

The modeling methodology for (1) and (2) has already been discussed in Chapter 2. In the next subsection, the focus is the description of (3) the crystallization growth kinetics, which is the most relevant phenomenon in crystallization. All these subproblems (1)-(3) are interrelated and should be coupled through variables that are transferred between the distinct modeling levels.

6.2 Crystal growth kinetics and interplay with fluid dynamics

The major phenomenon in crystallization is the particle growth due to the mass transfer from the solution to the solid phase. The growth kinetics is commonly described by two main mechanisms: the transport of the solute molecules from the bulk of the solution through the boundary layer by diffusion and the integration into the crystal lattice, like in a diffusion-reaction framework.

Thus, the global growth kinetic is given by the slowest mechanism. The growth is said to be diffusion-limited if diffusion is the slower mechanism, or integration-limited if surface integration is the slower mechanism.

A general expression for the growth kinetic is typically given by:

$$G = \frac{dL}{dt} = k_{total} \left(\frac{c - c^*}{c^*} \right)^{n_g} \quad (6.1)$$

where n_g is the kinetic order; c is the solute concentration and c^* is the solute saturation concentration; k_{total} is the total (overall) growth rate constant, it combines the diffusive mass transfer coefficient (k_d) and the surface integration coefficient (k_s).

It is only possible to derive analytical relations for k_{total} when $n_g = 1$ or $n_g = 2$. In a first order growth kinetic ($n_g = 1$) the following relation can be obtained (Goede and Rosmalen (1990)):

$$k_{total} = \frac{1}{\frac{1}{k_d} + \frac{1}{k_s}} \quad (6.2)$$

This simplified relation is used in the present study.

In most cases, the lumped model (Eq. (6.1)) describes the particle size evolution with good accuracy. Nevertheless, no information about the dominating growth mechanism can be derived. It is generally accepted that the kinetic order $n_g = 1$ represents a case of exclusively diffusion-limited growth, while $n_g = 2$ represents a case of exclusively integration-limited growth. Most crystallization systems are better described with n_g in the range between 1 and 2, indicating that both mechanisms are relevant. As discussed later in Section 6.7.2, experiments have delivered a value of $n_g = 1.4$ for the present conditions.

6.2.1 Slip velocity and the diffusive mass transfer coefficient (k_d)

Considering the relation $k_d \approx D/\delta$ from Mullin (2001), k_d depends on the the diffusion coefficient D and on the boundary layer thickness δ , which is strongly influenced by the local slip velocities.

With the Eulerian-Eulerian modeling approach (see Chapter 2) it is possible to evaluate local slip velocities, which can be used for the calculation of the local diffusive mass transfer (k_d) coefficient based on a Sherwood-type relation:

$$\text{Sh} = a + b\text{Re}^c\text{Sc}^d \quad (6.3)$$

where $\text{Sh} = k_d l / D$ is the Sherwood number (Sh), $\text{Re} = u_s l \rho / \mu$ is the Reynolds number involving u_s , the particle slip velocity and l , the particle diameter. $\text{Sc} = \mu / \rho D$ is the Schmidt number.

In Fig. 6.2 the Sherwood number calculated by three different correlations is plotted against the slip velocity. The Sherwood correlation of Frössling (Frössling (1938)), Ranz (Ranz and Marshall (1952)) and Friedlander (Friedlander (1957)) are given by Eqs. (6.4a), (6.4b) and (6.4c), respectively

$$\text{Sh}_{\text{Frössling}} = 2 + 1.10 \text{Re}^{1/2} \text{Sc}^{1/3} \quad \text{Re} > 1 \quad (6.4a)$$

$$\text{Sh}_{\text{Ranz-Marshall}} = 2 + 0.6 \text{Re}^{1/2} \text{Sc}^{1/3} \quad 0 < \text{Re} < 200 \quad (6.4b)$$

$$\text{Sh}_{\text{Friedlander}} = 0.99 \text{Re}^{1/3} \text{Sc}^{1/3} \quad \text{Re} < 1 \quad (6.4c)$$

Note that these are empirical relations fitted based on mass transfer experiments for single spheres. All tested correlations show similar trends. The Friedlander correlation is used in this work as it is reportedly more accurate for very low Reynolds number. A more rigorous approach would involve the measurement of the thickness of the concentration boundary layer for a single potassium aluminium sulfate crystal at varying flow velocities, see Liiri et al. (2006). This might be worth to investigate in future studies.

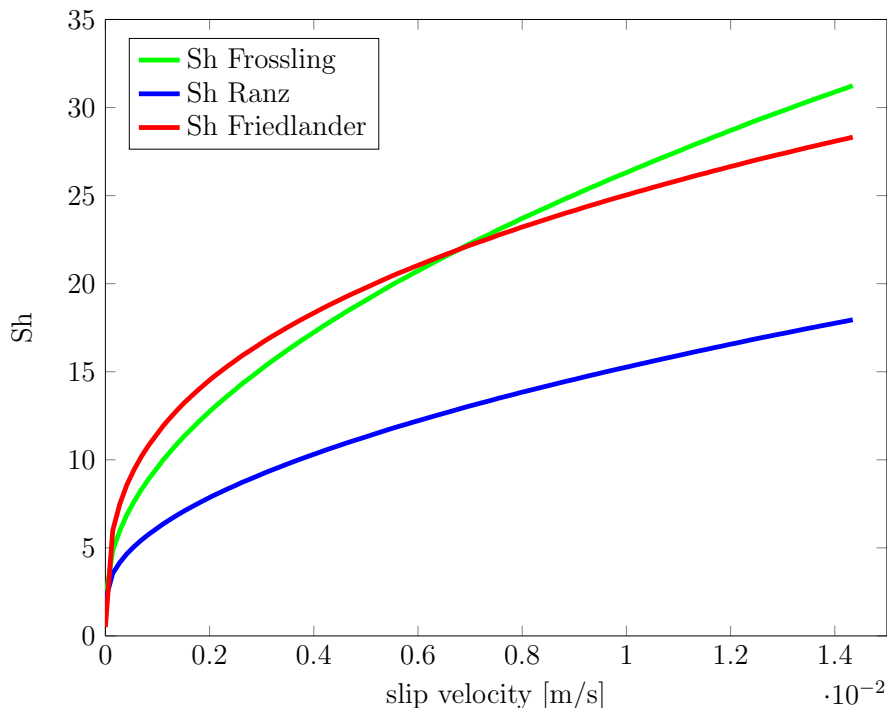


Figure 6.2: Sherwood number correlations, as function of slip velocities.

6.3 Studied system: batch cooling crystallization reactor

The studied system is a batch cooling crystallization reactor. The experimental data has been obtained from the group “Physical and Chemical Foundations of Process Engineering” at the Max Planck Institute in Magdeburg. Relevant experimental details are described in this section. For more information please refer to [Tommel et al. \(In press, 2016\)](#).

6.3.1 Experimental details

The experiments were conducted in a double jacketed stirred tank reactor. The system is equipped with temperature (T) and concentration measurement (refractive index probe, RI) devices for the liquid phase. For the analysis of the solid phase an online microscope (OM) and a non-classifying bottom outlet was used, see experimental scheme in Fig. 6.3.

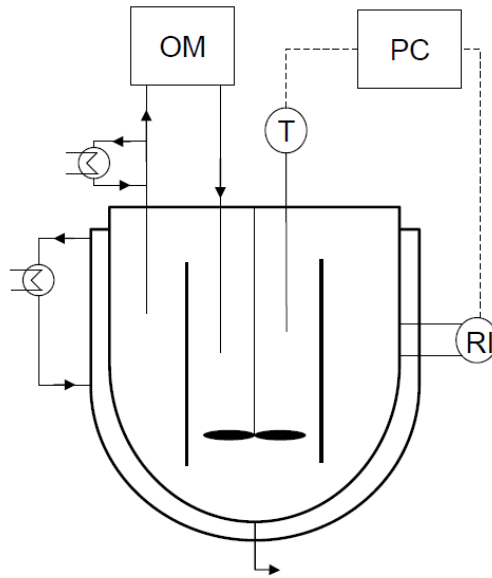


Figure 6.3: Sketch of the experiment set-up.

Crystallization of potassium aluminium sulfate ($\text{KAL}(\text{SO}_4)_2$) has been considered. Operating conditions for the selected experiment are given in Table 6.1. The original experiment investigated the crystallization and the dissolution processes. Nevertheless, in this chapter only the data for the crystallization process has been considered.

Table 6.1: Operating conditions for the selected experiment.

Property	Value
Mass of water (in the initial solution)	20 [kg]
Mass of $\text{KAL}(\text{SO}_4)_2$ (in the initial solution)	4 [kg]
Mass of $\text{KAL}(\text{SO}_4)_2$ (solid)	0.1 [kg]
Temperature ramp	-10 [K/h]
T_{ini}	307 [K]
Agitation speed	300 [rpm]

6.3.2 Physical properties and measured data

The physical properties for the liquid phase (continuous phase) and the solid phase (disperse phase) are given in Tables 6.2 and 6.3, respectively.

Table 6.2: Properties of the liquid phase (continuous phase).

Property	Value
Density (solution)	1077 [kg/m ³]
Dynamic viscosity (solution)	1.1733×10^{-3} [N s/m ²]
Saturation concentration (solubility curve)	$5.06 + 0.23T + 7.76 \times 10^{-3}T^2 - 2.43 \times 10^{-4}T^3 + 4.86 \times 10^{-6}T^4$ [wt-%]
Diffusion coeff. (KAL(SO ₄) ₂ in water)	3×10^{-10} [m ² /s] at 300K

In fact, the density and viscosity values of the liquid phase vary slightly during the crystallization process. Only the average values for the density and viscosity are given in Table 6.2. These values are used as constant flow properties for the CFD simulation.

A small volume variation of the reactor during the crystallization process is expected. Nevertheless, the reactor volume is considered constant during the CFD computations. The volume variation is estimated to be approximately 0.1%, as showed in Appendix A.2, and is thus negligible.

Online measured data for concentration and temperature are given in Fig. 6.4. These information together with the saturation concentration are required to calculate the supersaturation values, which is the driving force for crystallization.

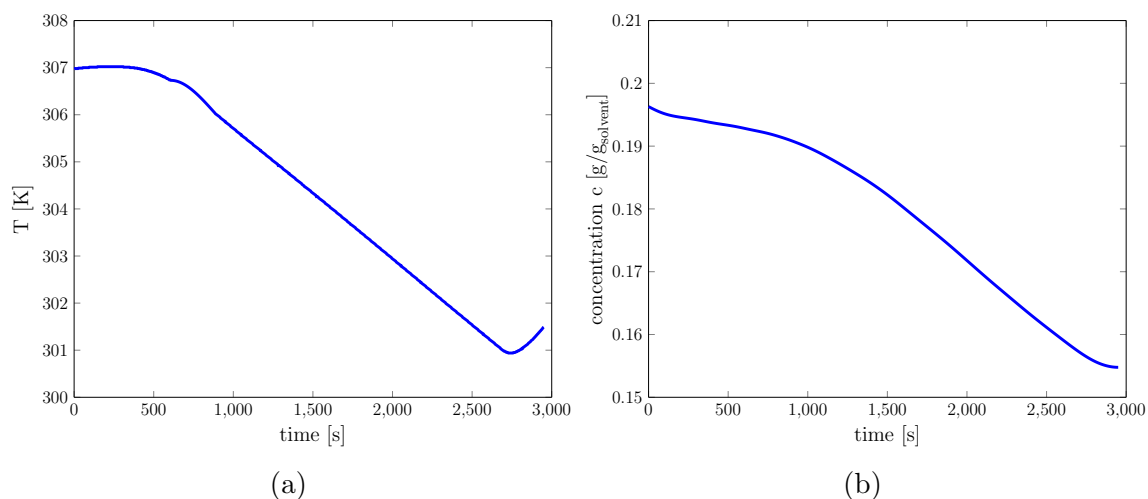


Figure 6.4: Online measurements during the crystallization process (a) temperature (b) concentration.

Table 6.3: Properties of the solid phase (disperse phase).

Property	Value
Density (KAL(SO ₄) ₂ crystals)	1750 [kg/m ³]
Crystal shape factor (KAL(SO ₄) ₂ crystals)	1/3

Online measurements of the particle size using the online microscope (OM) have been considered. The measured distributions are showed in Fig. 6.5 in terms of mass density distribution (q_3) and number density distribution (q_0). Fig. 6.5(a) represents a two-peak distribution. The left (smaller) peak was most probably generated by nucleated crystals while the right peak evolved from the initial seed distribution. Note that in terms of mass the nucleated crystals do not represent a significant percentage. As the main focus of this study is the investigation of the growth mechanism, a filtered distribution disconsidering the nucleated crystals has been generated (see Fig. 6.6) for the later comparison with the QMOM and CFD-QMOM simulations.

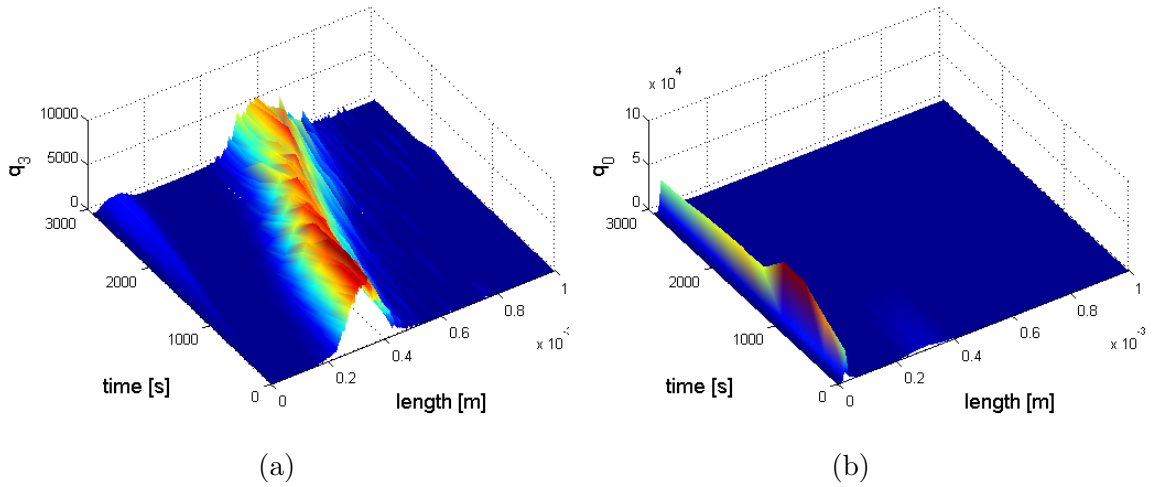


Figure 6.5: Measured distributions represented in terms of (a) mass density distribution and (b) number density distribution.

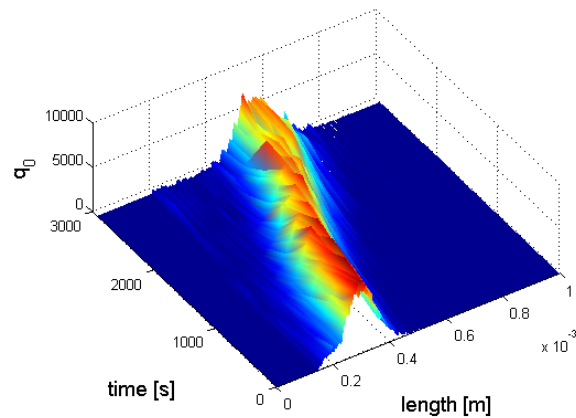


Figure 6.6: Filtered number density distribution, without nucleated crystals.

6.4 Reactor geometry

The 3-D geometry of the stirred tank reactor was created using the CAD-software Siemens PLM NX7. The geometry was built according to original drawings and only minor details were neglected, i.e., slight impeller curvature, outlet connection and measurement instruments. The vertical cylindrical vessel, draft tube with baffles and three-blade propeller are depicted in Fig. 6.7 and the assembled geometry is given in Fig. 6.8.

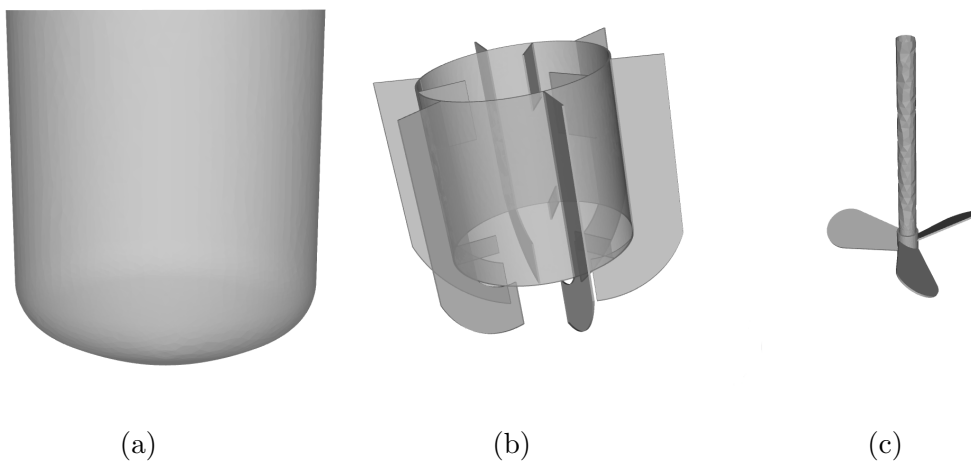


Figure 6.7: Stirred tank reactor geometry (a) Vertical cylindrical vessel (b) Draft tube with baffles (c) Three-blade propeller.



Figure 6.8: Assembled 3D geometry.

Dimensions of the reactor elements are given in Table 6.4. A detailed sketch of the reactor geometry can be found in [Henneberg \(2014\)](#).

Table 6.4: Dimensions of reactor elements.

Reactor element	Value
Vessel height (at working volume)	0.35 [m]
Vessel diameter	0.31 [m]
Draft tube diameter	0.19 [m]
Propeller number of blades	3
Propeller diameter	0.09 [m]
Propeller blade pitch	60°

6.5 Reactor mesh and boundary conditions

The mesh for the 3-D stirred tank reactor was created using the software ANSYS-ICEM 14.0. Unstructured mesh with tetrahedral elements was used in most part of the domain, see Figure 6.9. At near-wall, prism layer elements were generated. Due to the small distance between the propeller and the draft tube it was not possible to generate enough number of prism layers there. Therefore, pentahedral elements were used in this region.

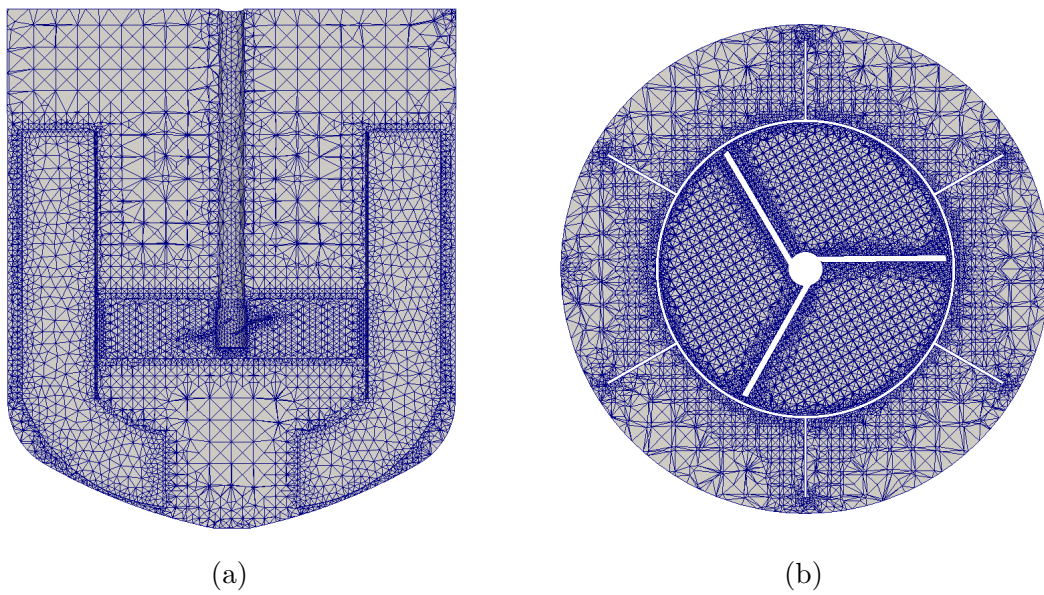


Figure 6.9: Reactor mesh (a) Clip plane of the reactor mesh (front view) (b) Clip plane of the reactor mesh (top view)

The mesh for the steady zone and the mesh for the rotating zone were created separately and merged. Non-conformal interfaces between these two zones were generated. In non-conformal interfaces the grid lines do not match. Nevertheless, it is important to create interfaces with similar amount of elements to reduce interpolation errors. The employed boundary conditions are shown in Fig. 6.10.

An extensive grid dependency study for the considered reactor is described in [Henneberg \(2014\)](#). The most important characteristics of the finally retained configuration are given in Table 6.5.

Table 6.5: Reactor mesh properties.

Property	Value
Total number of grid cells	712319
Minimum orthogonal quality	0.32
Maximum aspect ratio	13.37

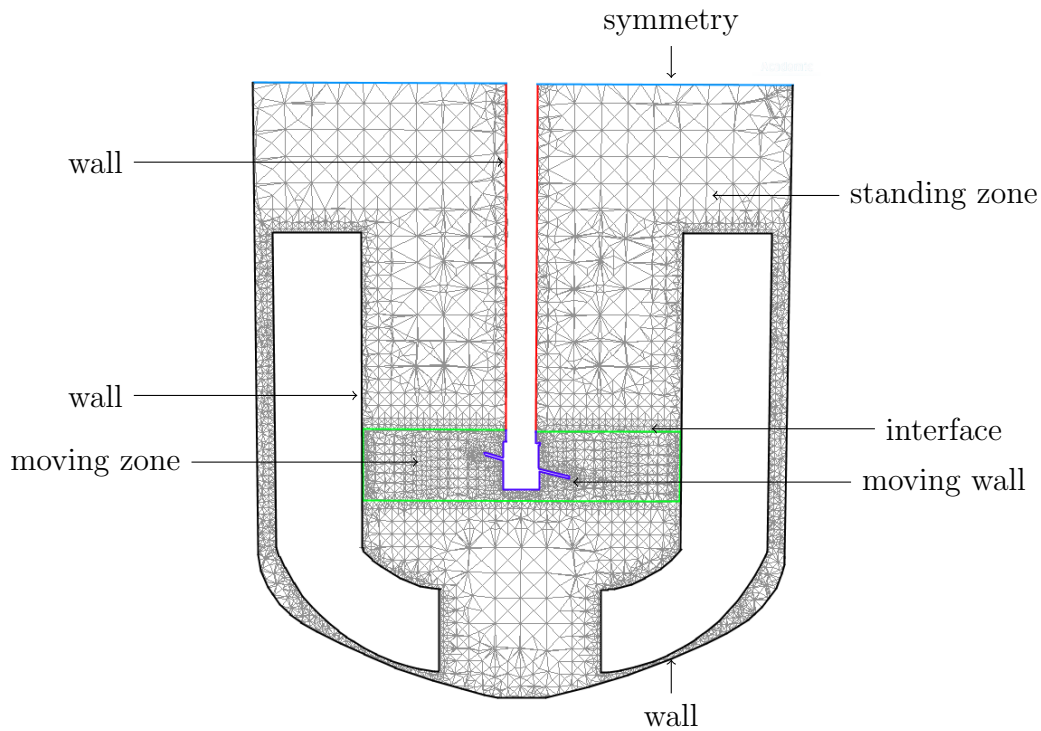


Figure 6.10: Boundary conditions.

6.6 CFD simulation: hydrodynamics (single phase)

Two approaches were initially considered for the simulation of the flow: the multiple reference frame (MRF) and the sliding mesh model (SMM). The MRF approach assumes that an assigned cell volume (moving zone) moves at a constant rotation speed, yet the mesh remains fixed. The MRF is also known as “frozen flow approach”. The SMM approach accounts for the relative motion of standing and moving zone. This approach is computationally more demanding than the MRF, as the mesh moves with the time. But it is also more accurate.

The overall flow pattern and velocity magnitude computed with MRF and SMM approaches are very similar. In both simulations the propellers produced an axial flow. Nevertheless, the vortex pattern around the propellers show visible differences (see Fig. 6.11), that implies residence time.

The gap between propeller and draft-tube is very small, which leads to a strong interaction between these components. It is reported in the literature that in this case the SMM delivers more accurate results (Bakker et al. (2009); Tabor et al. (1996) and Deglon and Meyer (2006)). The SMM has thus been employed for all simulations in this work, in spite of its higher computational cost.

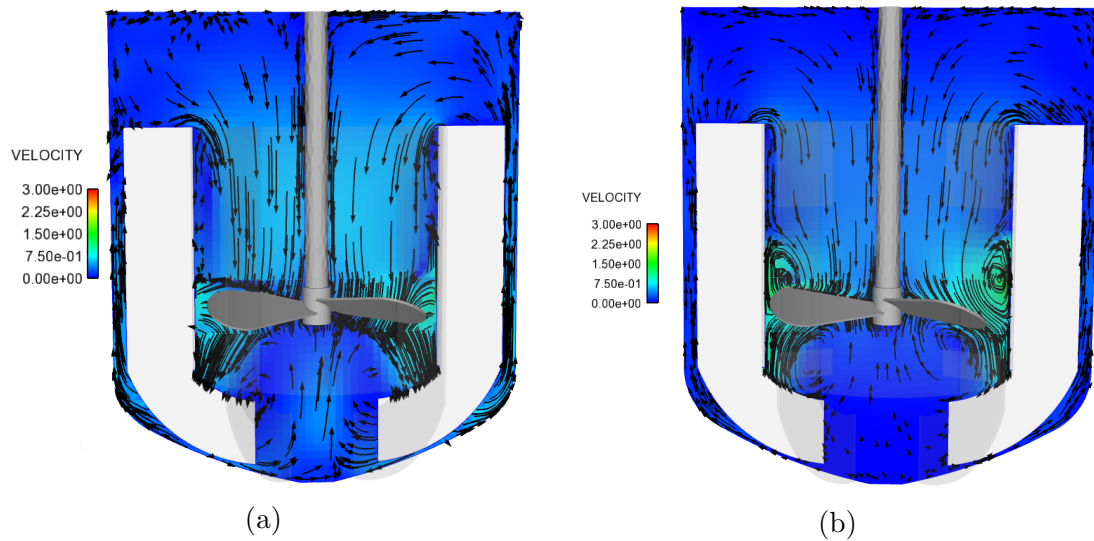


Figure 6.11: (a) MRF simulation (b) SMM simulation.

All CFD simulations employed the realizable $k - \epsilon$ RANS model with the optimized constant set (see Chapter 4). In the near-wall regions the standard wall function has been selected.

6.7 QMOM (0-D approach)

The 0-D (zero dimensional) simulation considering only the population balance modeling is an important step towards the coupled CFD-QMOM simulation of the multiphase reactor. This step is necessary in order to evaluate qualitatively and quantitatively the results obtained with QMOM.

The 0-D approach describes the reactor as an homogeneous system; local fluid dynamics information is not considered.

6.7.1 Initial distribution

The initial seed distribution in terms of number density function (NDF), as well as the computed weights and abscissas are showed in Fig. 6.12. Three quadrature points are used to describe the distribution. In this manner the first six moments can be accurately described, see Section 2.3.1. In Table 6.6 the initial six moments and characteristic diameters are given.

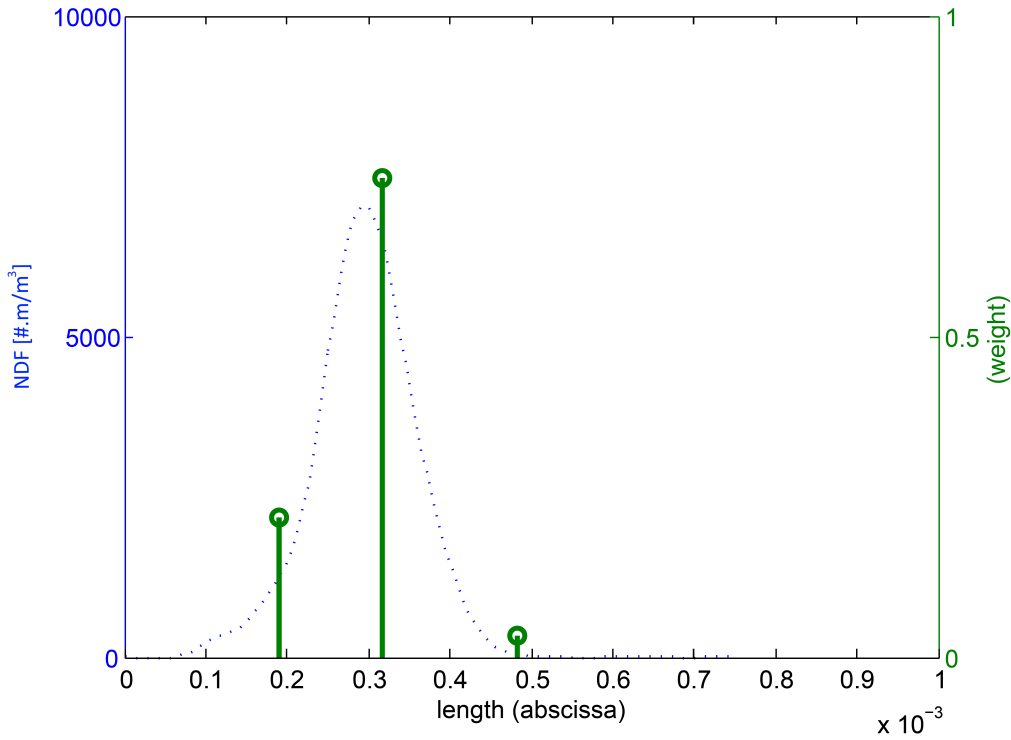


Figure 6.12: Weights and abscissas of the normalized NDF.

Table 6.6: Moments and characteristic diameters of the initial distribution.

Property	Value
Moments of the normalized distribution	$\mu_0 = 1.0$ $\mu_1 = 2.945000 \times 10^{-4}$ $\mu_2 = 8.967175 \times 10^{-8}$ $\mu_3 = 2.814088 \times 10^{-11}$ $\mu_4 = 9.078798 \times 10^{-15}$ $\mu_5 = 3.004811 \times 10^{-18}$
Median diameter (d_{10})	294×10^{-6} [m]
Sauter diameter (d_{32})	313×10^{-6} [m]

6.7.2 Modeling

The lumped model presented in Eq. (6.1) is employed for the calculation of the growth rate kinetic. The values for the model parameters are obtained from [Temmel et al. \(In press, 2016\)](#), where the model has been fitted and tested for different experiments. The employed parameter values are given as follows: $k_{total} = 6 \times 10^{-6}$ [m/s], $n_g = 1.4$ and $E_A = 4.5 \times 10^{-7}$ [kJ/mol].

The measured concentration and temperature profiles given in Fig 6.4 are used for the calculation of the supersaturation concentration.

In this work, the idea is to study the crystal growth and the interplay with the fluid dynamics. Therefore, only the growth phenomenon have been considered. As showed in Fig. 6.5(a) the mass of the nucleated crystals is very small compared with the mass of the seeds.

The QMOM algorithm, which includes the ODEs for the solution of the moments equation and the Product-difference algorithm (PDA) for the computation of weights and abscissas have been implemented in MATLAB. In the considered case three-point quadratures are used to represent the distribution. Therefore, six moment equations have to be simultaneously solved.

6.7.3 Results

The evolution of the median particle size with time is given in Fig. 6.13. The comparison between experiment and simulation shows that the QMOM is an accurate approach for the description of the crystal growth. Futhermore, the simple lumped model can quite accurately describe the growth kinetics.

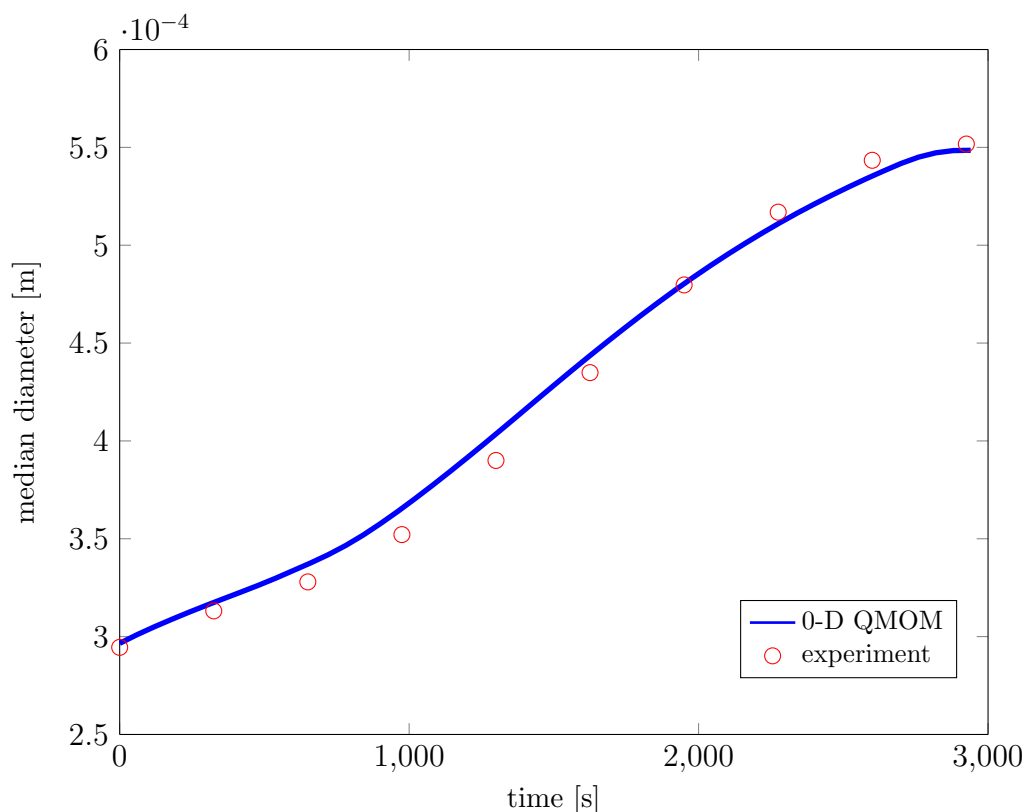


Figure 6.13: Particle median diameter evolution; comparison between experiment and 0-D QMOM simulation.

6.8 CFD-QMOM (3-D brute-force approach)

The 3-D (three dimensional) simulation considering the full multiphase reactor modeling is discussed in this Section. In this comprehensive simulation the distinct modeling levels have been coupled within the Euler-Euler multifluid framework. The CFD-QMOM model implemented in ANSYS Fluent 14.0 is used together with an implemented user-defined function (UDF).

6.8.1 CFD-QMOM (mixing dynamics)

The evaluation of the moment transport in the absence of any size changing mechanisms, e.g., growth, nucleation, breakage, aggregation, is important for the verification of the stability of the CFD-QMOM algorithm.

The CFD-QMOM implementation in ANSYS Fluent 14.0 considers that all the moments are transported with the same velocity. Nevertheless, in regions close to boundaries, to interfaces or when the volume fraction of the disperse phase tends to zero the CFD-QMOM may still deliver unphysical results.

When no source term is considered in the moment transport equation, the characteristic diameter should remain constant. Figure 6.14 shows the Sauter mean diameter at the initial time and at time 1.5s. The Sauter mean diameter remains indeed constant in the whole domain (note the color scale), showing that no unphysical processes occur.

As expected, the volume fraction assumes different values in the domain but the ratio between the moments in each cell remains constant, see Fig. 6.15.

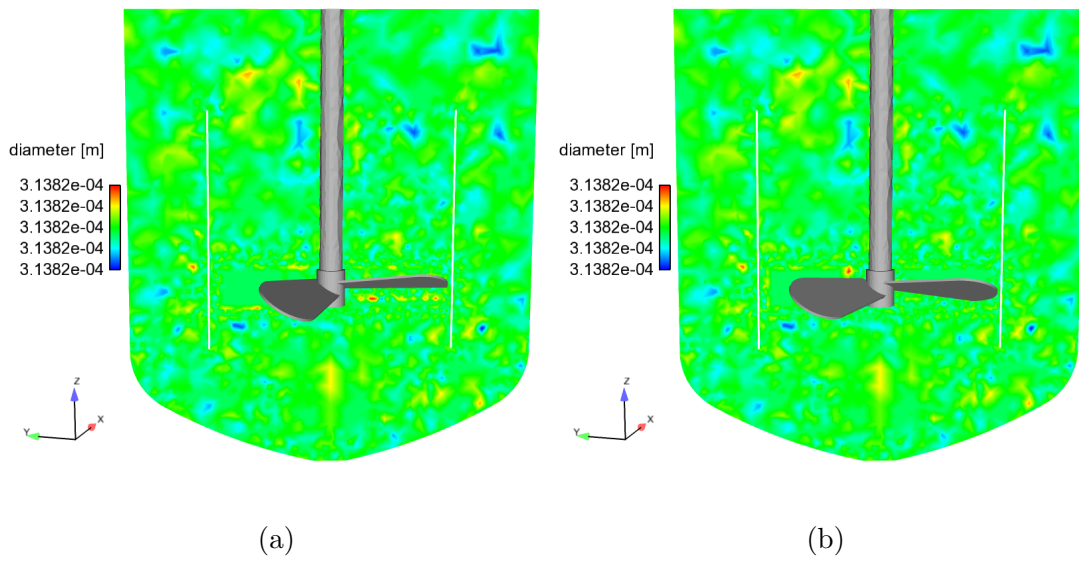


Figure 6.14: Sauter mean diameter contour plot: (a) initial condition, (b) at time 1.5s. Note that the color scale corresponds to size modifications in nanometers, showing that the diameters remain indeed constant

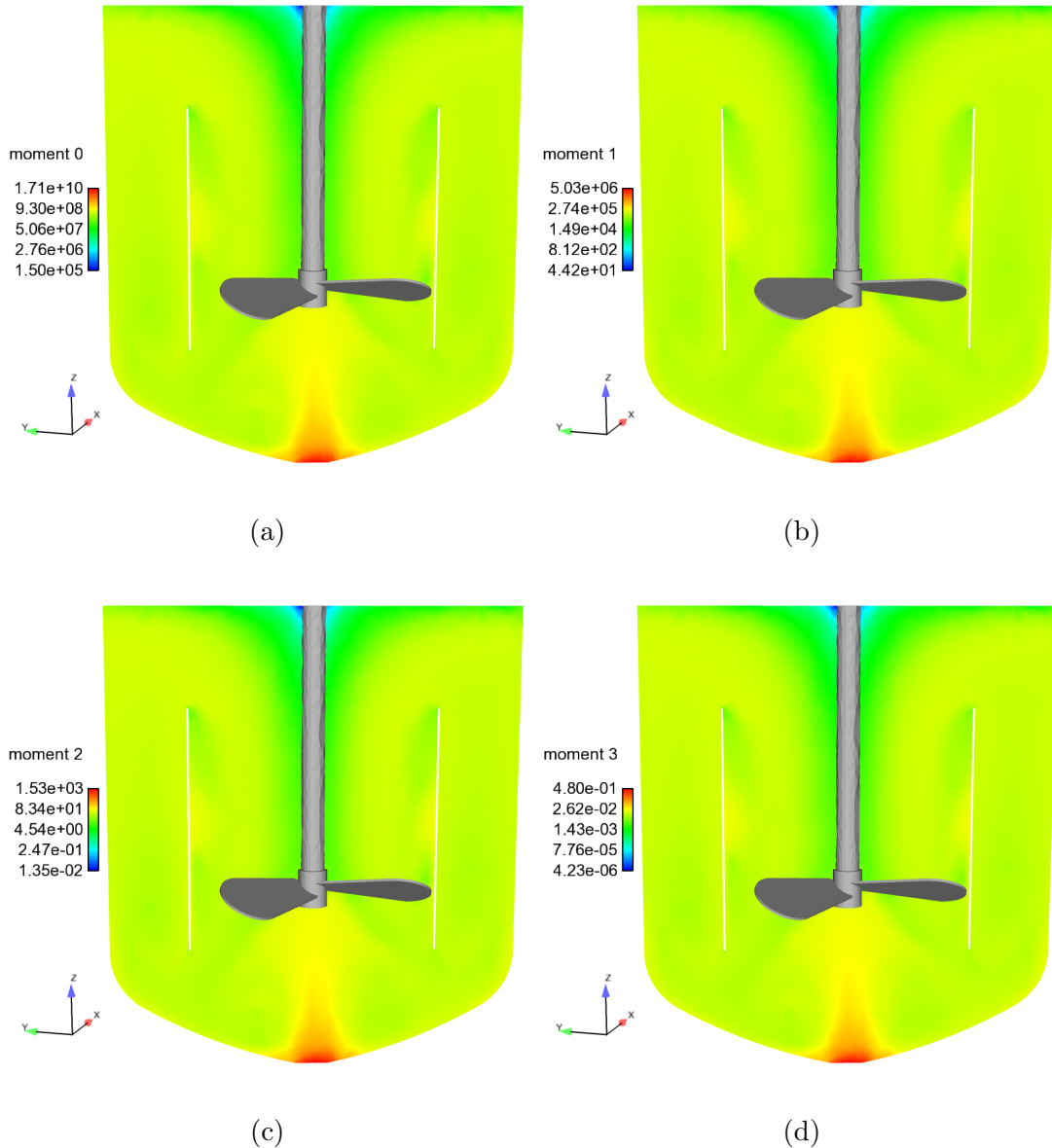


Figure 6.15: Moments contour plot at time 1.5s (a) μ_0 (b) μ_1 (c) μ_2 and (d) μ_3 .

6.8.2 Models used in ANSYS Fluent

The employed models are as follows:

- Fluid dynamics modeling: optimized realizable $k - \epsilon$ turbulence model, Euler-Euler multifluid, Schiller-Naumann drag model
- Particle properties evolution modeling: quadrature method of moments (QMOM)
- Kinetics modeling: growth kinetic model

These are mostly built-in models from ANSYS Fluent 14.0. The additional growth kinetic model was implemented via a user-defined function (UDF). It takes

into account the local slip velocity for the estimation of the diffusive mass transfer coefficient (k_d) as described in Section 6.2.

Fig. 6.16 shows a diagram with the most important variables exchanged between the distinct modeling levels.

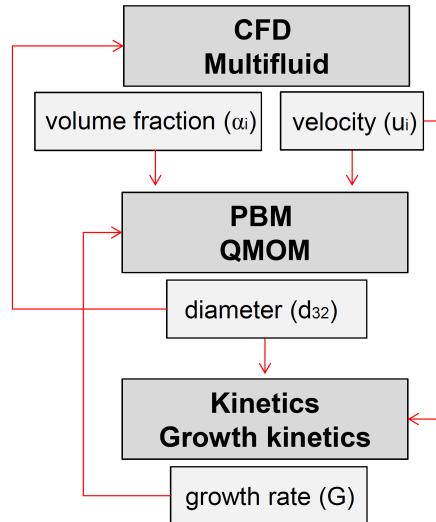


Figure 6.16: Diagram showing the link between the modeling levels.

The liquid phase (continuous phase) was treated as a homogeneous continuum. Thus, the supersaturation concentration is uniform in the domain, but changing with time according to the measured profile. Nevertheless, it is also possible to calculate the supersaturation concentration based on the information of the mass balance in the reactor.

6.8.3 Results

The contour plot of the volume fraction and the Sauter mean diameter of the disperse phase at time 1.5s is given in Fig. 6.17. The simulation time is still too short to observe significant changes in the particle diameter, since the whole process takes about 3000s. Nevertheless, smaller particles already tend to be found in the bottom of the reactor. This is a region with low velocity and prone to form recirculation zones, which might explain the slower growth rate.

Simulating 1.5s (physical time) of the process takes approximately 4 days on 24 cores (4 intel 6-core computers) Intel(R) Xeon(R) CPU 3.50GHz. Considering the long duration of the crystallization process which takes approximately 3000s (physical time), the CFD 3-D brute-force simulation of the full crystallization process leads to an intractable computing time (more than 20 years). Motivated by this, a novel methodology combining the 3-D and the 0-D simulation has been elaborated.

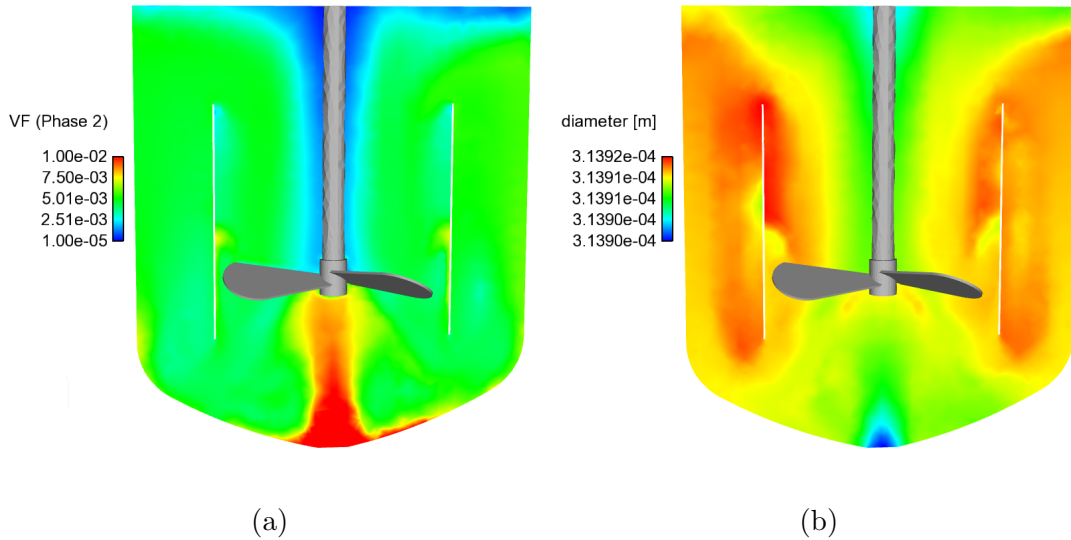


Figure 6.17: (a) Volume fraction and (b) Sauter mean diameter of the disperse phase, at time 1.5s.

6.9 Coupled 3-D/0-D simulation

The phenomena in a crystallization reactor have very different time and length scales. For instance, while the transport and mixing of the particles in the reactor occurs in a couple of seconds, the crystal growth is a much slower process. In general, the duration of the crystallization process in a batch reactor ranges from some minutes to a few hours. The large difference of time scales prevents any use of the CFD 3-D brute-force approach for the simulation of a long time span in this multiscale chemical reactor, as shown in Section 6.8.

CFD-based “multicompartment”, “network-of-zones” or “multi-zone” are practical approaches to simulate multiphase chemical reactors (Bezzo et al. (2005); Delafosse et al. (2014)), while still considering the different modeling levels, e.g., fluid dynamics, population balance, growth kinetics. In the “multi-zone” approach the domain is divided into a limited number of interconnected zones in which the flow properties are assumed to be homogeneous. In the classical approach the CFD calculation is performed normally only once, before the start of the reduced simulation. In more elaborated approaches the CFD calculation is performed more frequently. Nevertheless, the main difficulty is still the definition of the zones in a way that they represent a perfectly mixed region. Therefore, there is still a need for methodologies that account for the correct local flow condition and mixing in an integrated multiscale chemical reactor modeling approach.

6.9.1 Methodology

The 3-D/0-D simulation approach developed in this work takes into account the mixing process, as well as the local condition of the flow for the simulation of the particle growth in the crystallization reactor. Knowing that in a batch stirred tank reactor the mixing process is relatively fast compared with the duration of the crystallization process, the simulation procedure is divided in two parts: the simulation of the mixing process and the simulation of the crystal growth.

The mixing process is again simulated in ANSYS Fluent 14.0. The 3-D CFD-QMOM model (see Section 6.8) is employed in this step. Only the sufficient amount of time to obtain a good mixing in the reactor is simulated. This represents just a short time of the real process, but it still takes a long simulation time. In a following step, the obtained local flow condition is frozen and used for the calculation of the particle size evolution in each grid cell. A 0-D QMOM model implemented in MATLAB is used in this step. The temporal discretization for solving the population balance equations is much larger than the temporal discretization used in the CFD calculation, see Fig. 6.18. In this manner, a large time of the real process can be simulated at low computational cost.

The coupling variables to be transferred between the two simulations are depicted in Fig. 6.18. The number of intermediate steps (np) should be chosen depending on the problem and the available computing power. The solution using the coupled 3-D/0-D methodology approaches the solution of the 3-D brute-force CFD simulation when increasing of the number of intermediate steps.

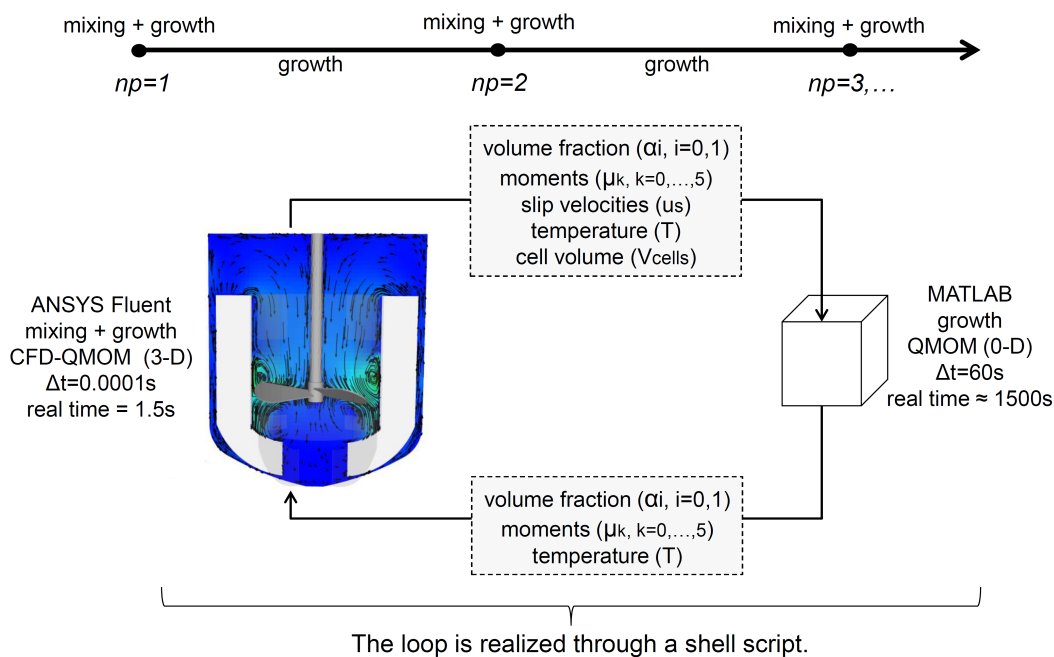


Figure 6.18: Simulation procedure for the coupled 3-D/0-D simulation.

6.9.2 Mixing time

The mixing time required to achieve a periodically unsteady flow condition in the reactor is a relevant parameter for the coupled 3-D/0-D simulation approach since it will strongly constrain the overall computational cost. For this purpose, the needed time has been evaluated.

The simulation set-up follows that described in Section 6.8. The variance (Var) of the volume fraction of the disperse phase (Eq. (6.5)) has been employed to quantify the mixing degree.

$$Var = \frac{1}{N_{cell}} \sum^{cells} (\alpha_d)^2 \quad (6.5)$$

The variance plot (Fig. 6.19) shows that after approximately 1s the reactor starts to converge to a periodically unsteady flow condition, which is consistent with the results of Ali et al. (2015), where the Euler-Lagrange approach Discrete Element Method (DEM) was used to simulate the same reactor but with different crystal seeds.

In Fig. 6.20 the volume fraction of the disperse phase is showed at four different times. Note that at times 3s and 4s the volume fraction contour plots are qualitatively very similar. Based on that, a physical time of 3s has been chosen as the recommended mixing time for all full 3-D CFD-QMOM simulations.

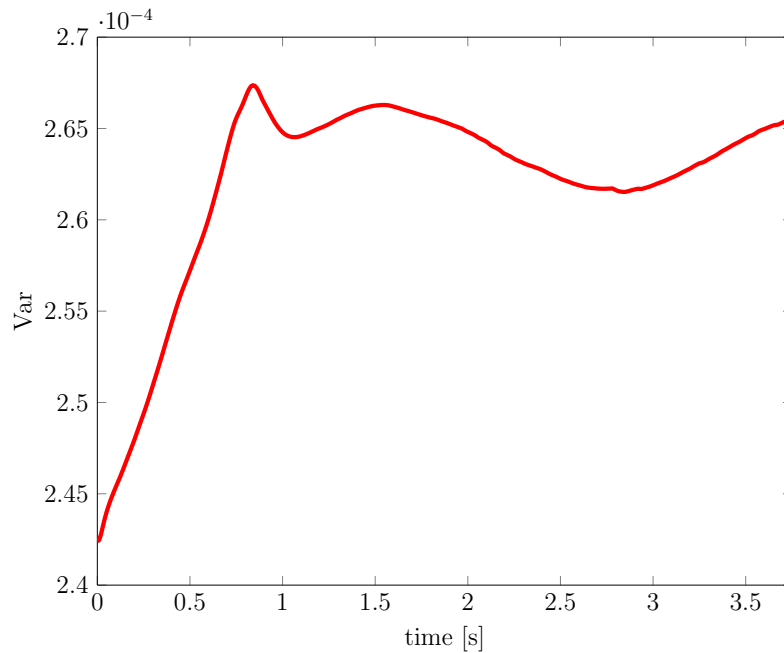


Figure 6.19: Variance of the volume fraction of the disperse phase in the stirred tank reactor as function of time.

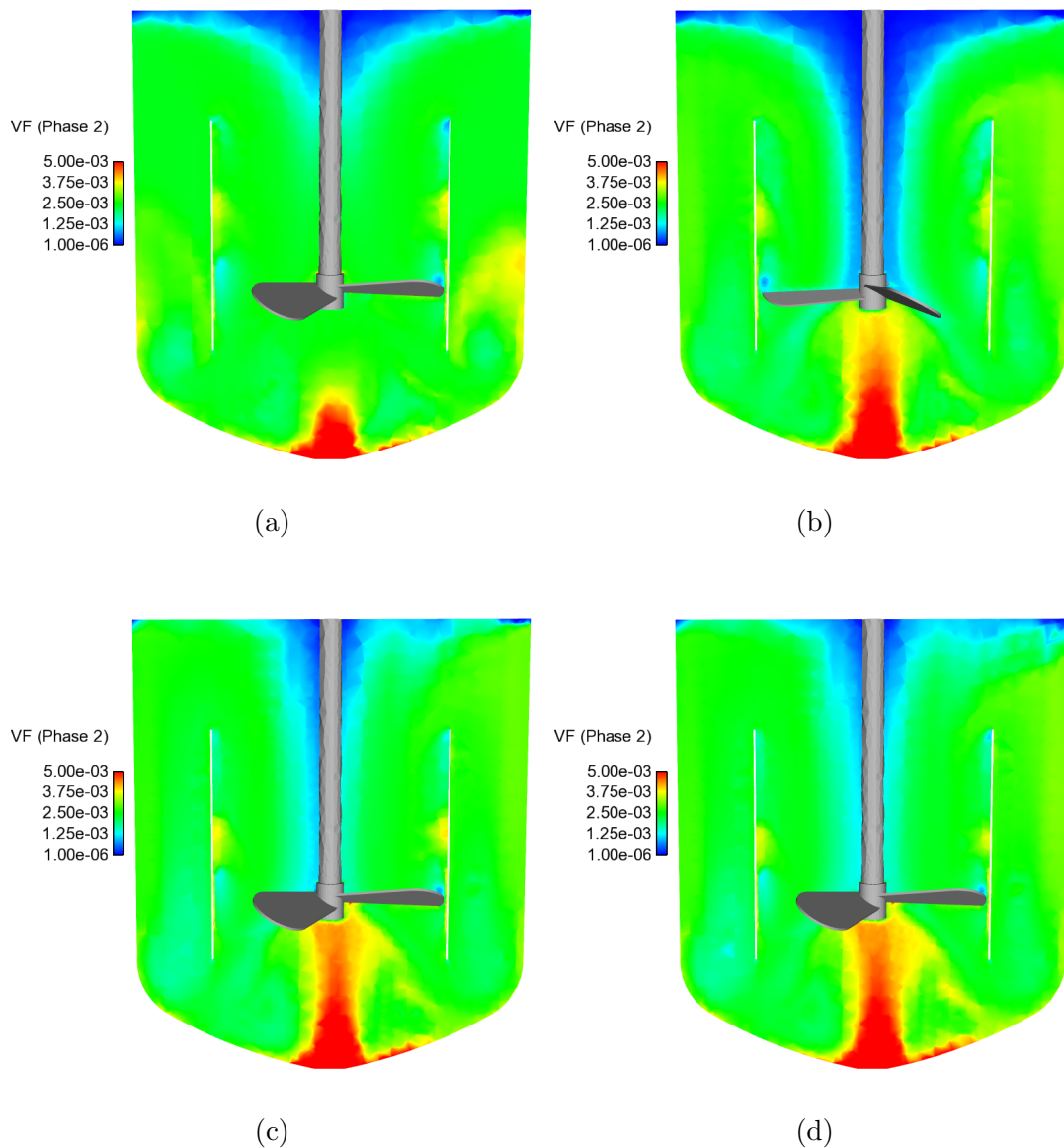


Figure 6.20: Volume fraction of the disperse phase at different times (a) 0.75s, (b) 1.5s, (c) 3.0s and (d) 4.0s.

6.9.3 Results

The results of the simulations using the coupled 3-D/0-D methodology are presented in this Section. The simulation loop follows the procedure illustrated in Fig. 6.18.

Evolution of the particle size

The evolution of the particle size during the crystallization process is showed in Fig. 6.21. Experimental and simulation results are compared for the median mean diameter $d_{10} = \mu_1/\mu_0$.

Three intermediate steps have been chosen for the coupled simulation. Thus, a full 3-D CFD-QMOM evaluation is performed at times 0s, 1440s and 2880s.

Parameters for the growth kinetic have been obtained from [Temmel et al. \(In press, 2016\)](#) as shown in Section 6.7.2. Nevertheless, the analytical relation for k_{total} (Eq. (6.2)) has been employed in this computation. In this manner, the diffusive mass transfer coefficient (k_d) has been computed in each cell based on the value of the local slip velocity. The surface integration coefficient (k_s) has been kept constant during the simulation; it has been estimated based on the value of k_{total} obtained from [Temmel et al. \(In press, 2016\)](#) and on the computed value of k_d at the initial time.

Although the simulation predicts the correct trend (see Fig. 6.21), the results deviate from the experiment increasingly so with time. This is mostly because of the inaccurate estimation of the surface integration coefficient (k_s). A more advanced approach should consider a dynamics adaptation of k_s or an iterative method to recalculate the value of k_s .

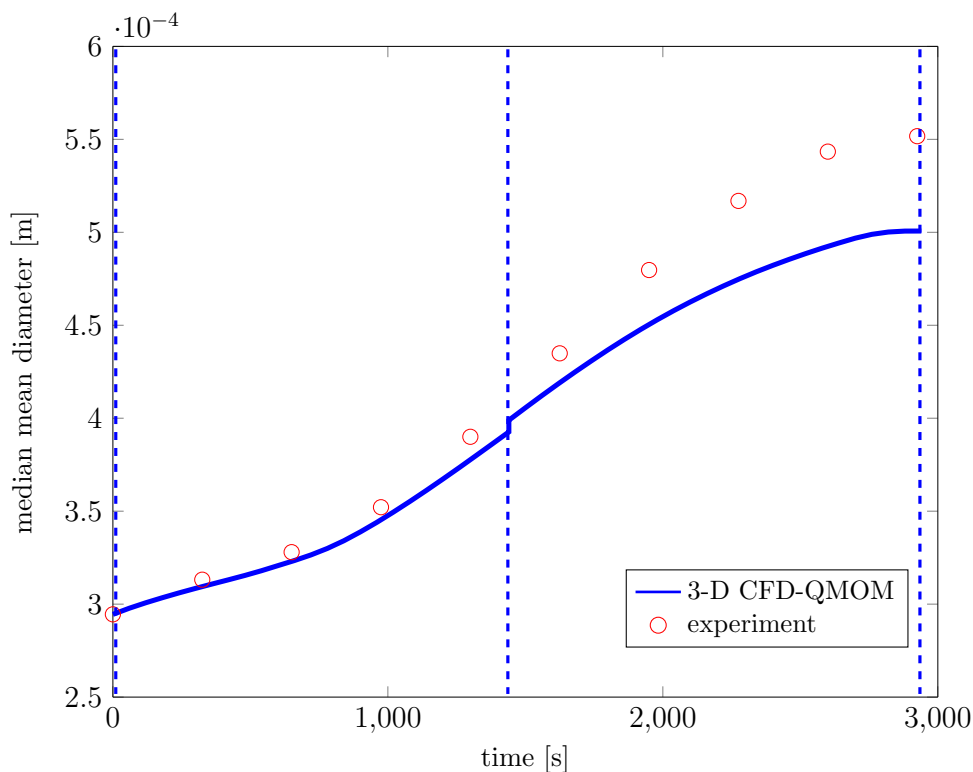


Figure 6.21: Median mean diameter evolution in the whole reactor; comparison between experiment and coupled 3-D/0-D simulation.

Volume fraction and Sauter mean diameter

The contour plot of the volume fraction and the Sauter mean diameter in the stirred tank reactor at three different times are given in Fig. 6.22. As expected, the overall values for the volume fraction of the disperse phase, as well as the Sauter mean diameter increase with time.

The volume fraction of the disperse phase is well distributed in the stirred tank reactor, with smaller values along the shaft and larger values in the region at the bottom of the reactor.

The bottom of the reactor is a region with small velocity magnitude. This is causing the deposition of the disperse phase and slower particle growth due to the low slip velocities.

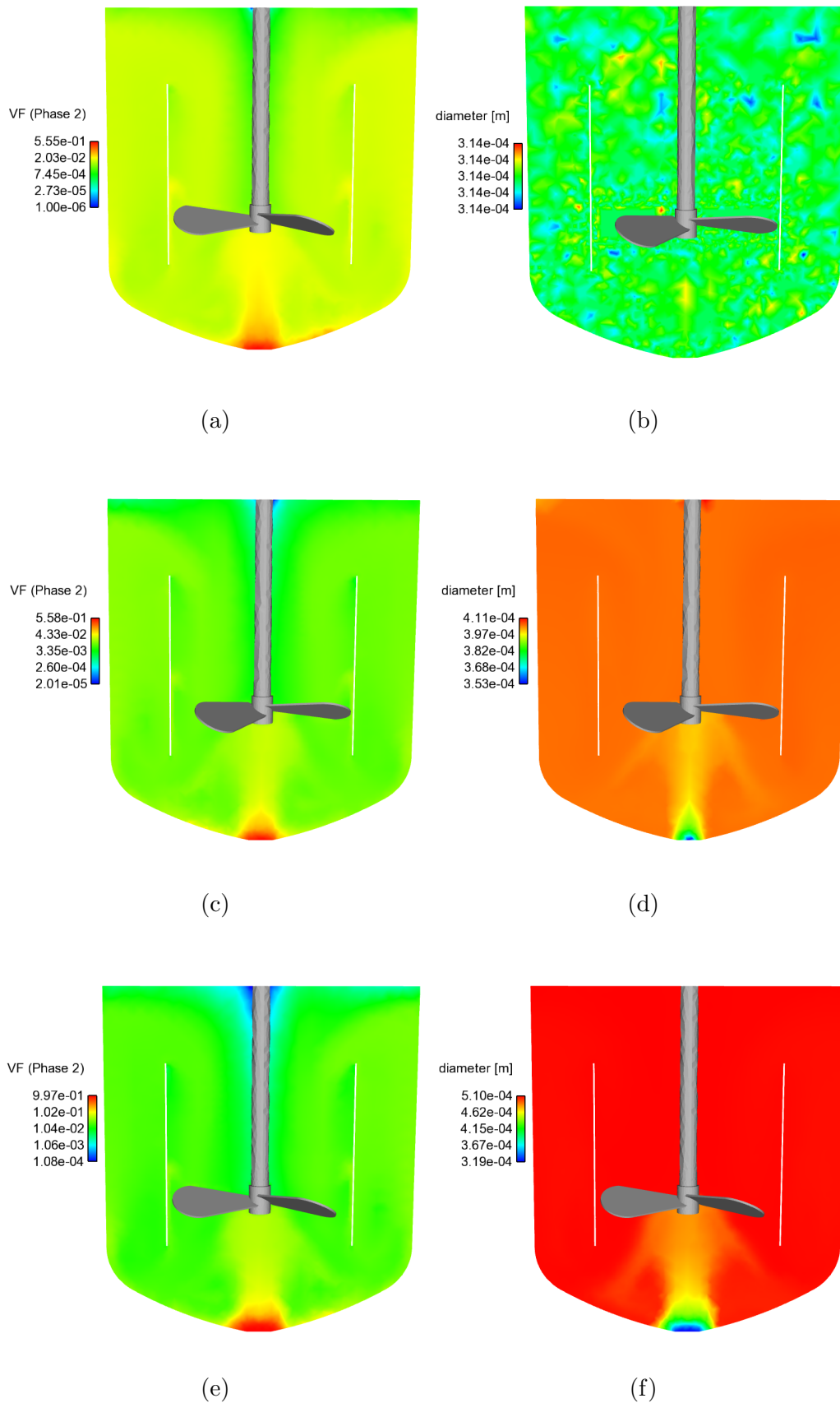


Figure 6.22: Contour plot of the volume fraction of the disperse phase (left) and Sauter mean diameter (right) at (a) and (b) starting step 1, (c) and (d) intermediate step 2, (d) and (e) final step 3.

Number density function (NDF) reconstruction

The number density function (NDF) reconstruction at a specific point is showed in Fig. 6.23. The chosen point is located approximately where the sample for the online microscopy analysis has been collected. The reconstruction of the distribution was done using the spline algorithm described in Section 2.4.

The initial distribution was accurately retrieved using only the information of the first six moments. At the final time, the reconstructed distribution presents a smaller particle size than the experimental result. This deviation is not an issue of the reconstruction algorithm, but of the growth kinetics which has lead to a smaller final particle size compared with the experiment (see Fig. 6.21).

Furthermore, the experimental result shows a broader final distribution which is related to the so-called “growth rate dispersion” phenomenon. This phenomenon is caused by the crystal-dependent growth rate. Although the considered model takes into account the different slip velocity in the reactor to calculate the growth rate, it considers that at a specific cell all the particles are subjected to the same slip velocity. Other quadrature-based method of moments (QBMM) might take into account distinct velocities at different quadrature points, allowing size-dependent growth-rate models. This will be subject of future works.

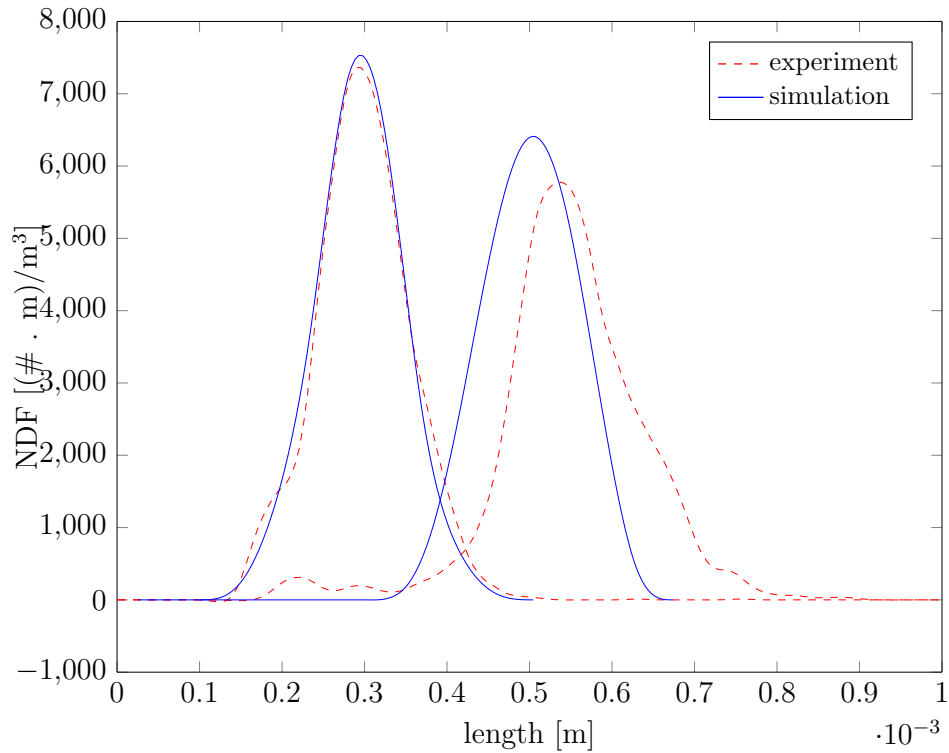


Figure 6.23: Number density function (NDF) reconstruction and comparison with experiment. Distributions at the initial time (left peaks), distributions at the final time (right peaks).

Slip velocity

The contour plot of the slip velocities for the three CFD-QMOM steps are given in Fig. 6.24. For each intermediate step, the slip velocities have been computed after the simulation of 3.0s mixing period. The slip velocities present a large range of values depending on the location in the domain. In general, the slip velocities are higher at the region close to the propeller and smaller in the regions close to the walls. As expected, the slip velocities increase with the increase of particle size.

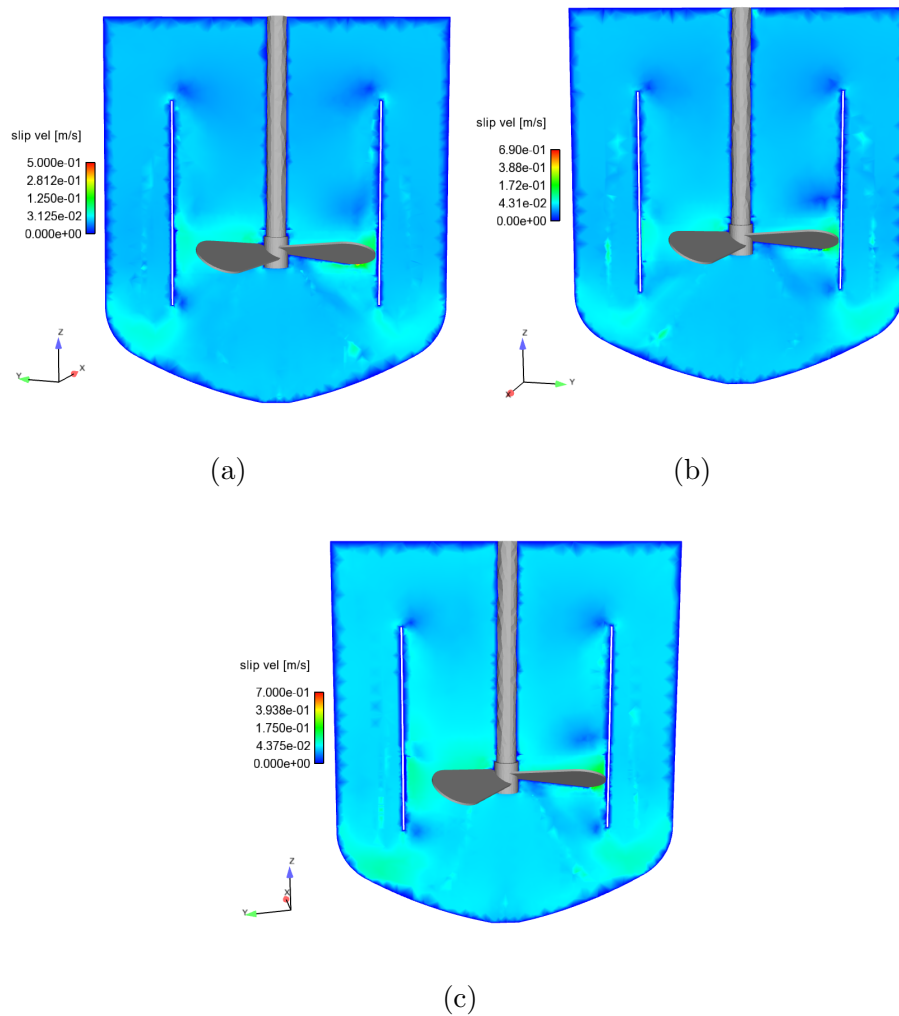


Figure 6.24: Contour plot of the slip velocities at times (a) 0s (starting step), (b) 1440s (intermediate step) and (c) 2880s (final step).

In Fig. 6.25, the cumulative mass distribution (Q_3) shows the mass percentage of particles up to a specific slip velocity. The median slip velocity values at times 0s, 1440s and 2880s are 0.0178m/s, 0.0258m/s and 0.0316m/s, respectively. The median slip velocity value corresponds to the value for which the cumulative mass distribution function is 0.5.

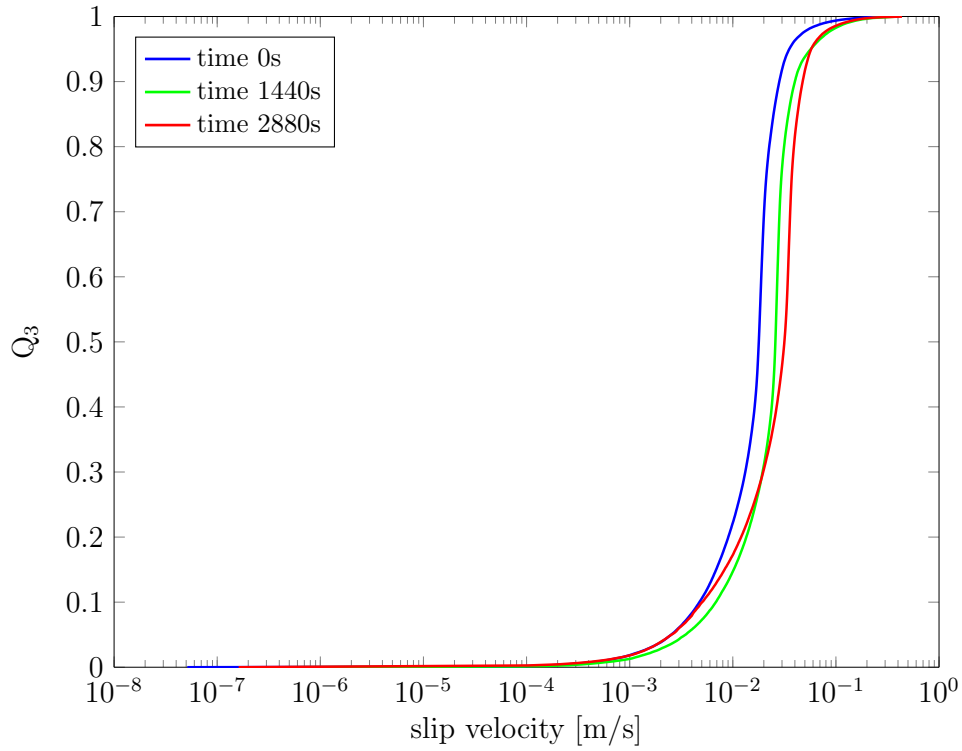


Figure 6.25: Cumulative mass distribution (Q_3) of the slip velocities at three different times (initial, intermediate, final).

Diffusive mass transfer coefficient (k_d) and surface integration coefficient (k_s)

The cumulative mass distribution (Q_3) of the diffusive mass transfer coefficient (k_d) at three different times is showed in Fig. 6.26. Note that the k_d value initially increases with time, which is directly related to the increasing value of the slip velocity. However, at the final time the value of k_d decreases, which is an effect of the increase of the particle size.

The median k_d values at times 0s, 1440s and 2880s are 1.3510×10^{-5} m/s, 1.5902×10^{-5} m/s and 1.5565×10^{-5} m/s, respectively.

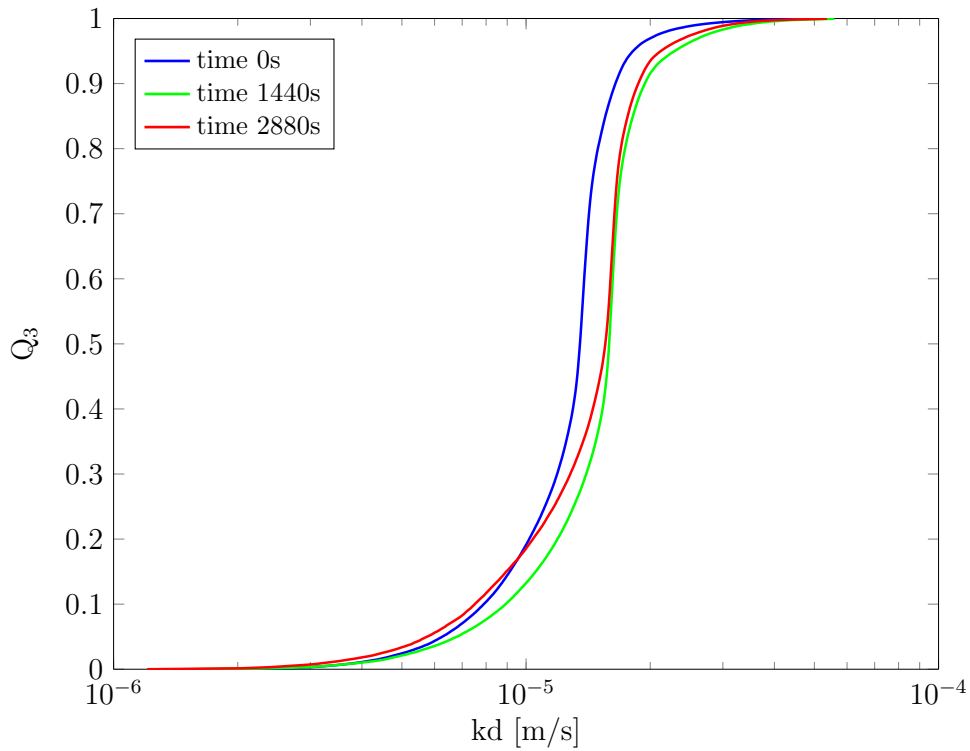


Figure 6.26: Cumulative mass distribution of the k_d in the 3-D stirrer reactor at three different times (initial, intermediate, final).

Mass balance

During the crystallization process the solute mass is transferred from the continuous phase to the disperse phase. The mass balance for the solute in the continuous and disperse phase is plotted in Fig. 6.27. The result is as expected, and the total amount of the solute mass remains constant.

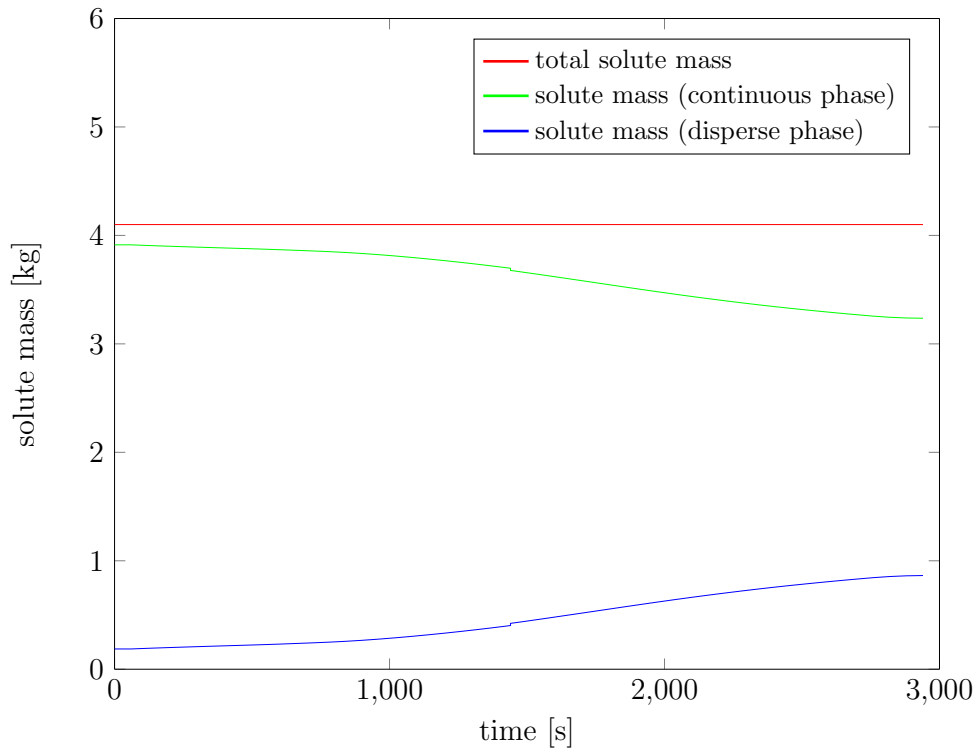


Figure 6.27: Solute mass balance in the reactor.

A comparison between the measured and the calculated supersaturation concentration (S) is showed in Fig. 6.28. The measured supersaturation concentration has been employed for the modeling. Although the calculated supersaturation concentration follows the same dynamics as the experimental supersaturation concentration, there is an increasing deviation between the values with time.

The nucleation has not been considered in the modeling. As showed in Fig. 6.5 the mass percentage of the nucleated particles is very small, but it increases with time. This probably explains the increasing deviation in the values of the supersaturation concentration.

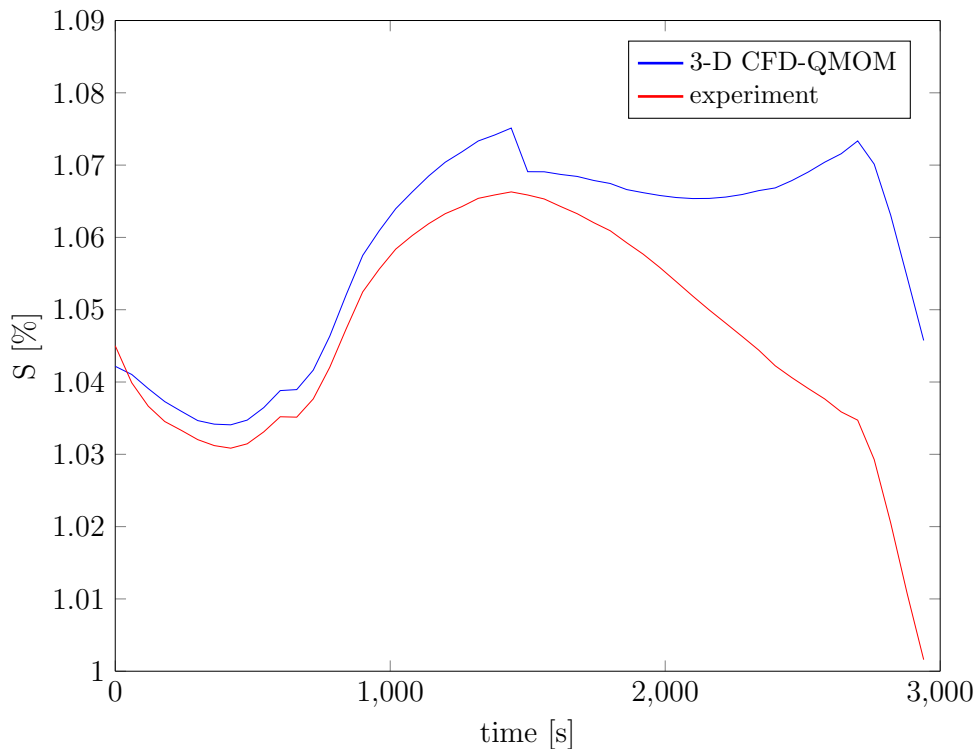


Figure 6.28: Supersaturation concentration (S).

6.10 Conclusions

Three approaches have been employed for the simulation of the batch crystallization reactor. Firstly, the quadrature method of moments 0-D (QMOM) is used to solve the population balance together with a lumped model for the description of the growth kinetic. This approach considers the crystallizer as a homogeneous system. The lumped growth model describes the evolution of the median mean diameter accurately. Nevertheless, with this approach no additional information about the process (e.g., spatial inhomogeneities, diffusive mass transfer coefficient (k_d)) can be derived.

Secondly, the 3-D CFD brute-force approach considered the unsteady fluid dynamics in the reactor coupled with the quadrature method of moments (QMOM). The implemented growth kinetic model takes into account the local slip velocity. This approach describes with details the volume fraction and particle size distributions in the reactor. Furthermore, it is possible to obtain values for the diffusive mass transfer coefficient (k_d) in the reactor. However, considering the duration of the crystallization process, the 3-D CFD brute-force approach leads to an intractable computing time (several years).

Thirdly, the developed 3-D/0-D approach divides the simulation in two parts:

the simulation of the mixing process and the simulation of the crystal growth. The exchange of information between these parts occurs at every intermediate steps. In this manner, the local flow information is used for the computation of the crystal growth during the whole crystallization process. The crystal growth is computed in every grid cell of the reactor. Thus, no zoning procedure is required as in the traditional “multi-zone” approaches.

With the developed methodology it is possible to investigate the volume fraction, particle size distribution, slip velocities and diffusive mass transfer coefficient (k_d) in the reactor at different times. This gives insights about the growth mechanisms and it is an important step towards the design and optimization of crystallization reactors.

Chapter 7

Conclusions and outlook

The simulation of multiphase chemical reactors is a complex multiscale problem. In order to accurately describe the involved phenomena, distinct modeling levels are required. Despite of the advances in modeling techniques and computational power, there is a need for efficient simulation techniques, robust models and practical coupling methodologies for the simulation of multiscale reactors of industrial interest.

In this work, techniques and methodologies that support the simulation of multiphase chemical reactors have been developed and tested, which include (i) technique for the reconstruction of distribution from a finite number of moments, (ii) methodology for model parameter optimization using multi-objective optimization and (iii) methodology for the multiscale coupling of multiphase reactors. The most relevant conclusions and outlook are discussed in the next paragraphs.

A popular method to solve PBEs is the so-called quadrature method of moments (QMOM). With this method it is possible to track the evolution of the particle properties considering only the initial moments of the underlying distribution. Nevertheless, it does not allow a straightforward reconstruction of the underlying distribution. The developed adaptive reconstruction technique using splines allows to retrieve distributions from a finite set of moments without prior knowledge on the shape of the distribution; only the initial moments and a rough estimation of the domain are needed. The algorithm is able to describe multi-peak distributions which are common in chemical engineering applications. Moreover, since its publication the developed algorithm has been applied to reconstruct distributions in different areas, e.g., pharmaceutical process, process control and quantum physics.

Another tool explored in this work is the multiobjective optimization, which has been used for the optimization of model parameters. It is a methodology that has not been well explored in this realm. In many practical situations, however, multiobjective optimization may deliver more robust and general applicable set of parameters compared with single-objective optimization. This methodology has

been applied for the optimization of the realizable $k - \epsilon$ turbulence model and for the optimization of kinetic and model parameters of a catalytic chemical reaction network.

The optimized realizable $k - \epsilon$ turbulence model improved the predictions or at least delivered results of the same level of accuracy as the standard model for all the tested configurations, even though the optimized parameter set does not differ much from the conventional values. Furthermore, the new recommended values do not lead to any increase in the computational cost.

The superstructure-based optimization applied for the optimization of model and kinetic parameters of a catalytic chemical reaction network appears to be an effective way to derive reaction mechanisms and optimal parameter sets in an automatic and flexible manner. Furthermore, the optimized parameter was fitted to distinct experiments simultaneously, leading to a generally applicable parameter set.

Finally, a batch crystallization reactor has been simulated. The Euler-Euler multiphase framework has been employed for the description of the distinct modeling levels, e.g., fluid dynamics, population balance, growth kinetics. Furthermore, the developed technique for the reconstruction of distributions from the moments, as well as the optimized set of constants of the realizable $k - \epsilon$ turbulence model have been integrated in the simulation of the crystallization reactor. However, it is computationally unaffordable to simulate the whole crystallization process considering the time step needed for the accurate description of fluid dynamics. Motivated by this, a methodology combining 3-D and 0-D simulations has been elaborated. The developed methodology takes into account the local condition of the flow, as well as the mixing process. It considers the mixing and the crystal growth separately but uses the local information of the flow for a correct description of the crystal growth. The exchange of information occurs at each “intermediate step”, which can be chosen according to the available computing power. With the increase of “intermediate steps”, the method delivers results comparable to a 3-D brute-force CFD simulation.

An important aspect investigated in the modeling was the use of local slip velocities for the calculation of the crystal growth rate. It is well accepted that the crystal growth happens due to two mechanisms, i.e., integration and diffusion. In highly agitated systems it is usually assumed that the diffusion is not the limiting mechanism. Nevertheless, in a stirred tank reactor the flow conditions are inhomogeneous and the slip velocities and crystal size vary depending on the location in the reactor. This issue has been investigated and values for slip velocities and diffusion mass transfer coefficients could be estimated.

Certainly, much more could be added to the developed techniques and method-

ologies. Further studies could, for instance, extend the reconstruction algorithm to describe multi-dimensional distributions. It would be also interesting to test the capabilities of the Kriging method to describe multi-dimensional distribution. Nevertheless, iterative reconstruction methods can only be used as a post-processing technique. The direct use of iterative reconstruction techniques in moment-based methods would increase drastically the computing time, considering that the reconstruction should be done in every grid cell and time step. Thus, non-iterative reconstruction algorithm would find an even larger application.

The methodology for model parameter estimation using multi-objective algorithm could be applied to further RANS turbulence models. In this class of models the constants have been usually determined based on simple flows. An optimization considering several geometries simultaneously would lead to more robust parameter sets. It would be interesting to add a rotating geometry test case to the optimization loop as it involves flow characteristics that do not appear in the channel, BFS, jet and flow over hill test cases.

It would be also interesting, in the case of multi-objective parameter estimation, to include some additional statistical analysis in order to quantify other aspects beyond the fitting quality.

Further improvements could also be added to the coupled 3-D/0-D simulation approach. For instance, the particle velocity history or the slip velocity distribution in the reactor could be integrated in the simulation loop rather than to rely on the frozen local flow information for the computation of the crystal growth. Moreover, in the current implementation the calculation of the slip velocity is based only on the Sauter mean diameter value. Other quadrature-based methods or a simple interpolation method could be used in other to calculate slip velocities based not only on a single diameter value.

Appendix A

Appendix

A.1 Two-equation RANS models

The multi-objective optimization methodology employed in Chapter 4 can be applied in a straightforward manner for the optimization of other RANS models. The most popular two-equation RANS models and their constants are given in Tables A.1 and A.2.

Table A.1: Popular two-equation $k - \epsilon$ turbulence models.

Model	Model Equations, Closure Constants and Auxiliary Relations
Standard $k - \epsilon$	Kinematic Eddy Viscosity: $\nu_t = C_\mu \frac{k^2}{\epsilon}$ Turbulent Kinetic Energy: $\frac{\partial k}{\partial t} + U_i \frac{\partial k}{\partial x_i} = \frac{\partial}{\partial x_j} \left[\left(\nu + \frac{\nu_t}{\sigma_k} \right) \frac{\partial k}{\partial x_j} \right] + P_k + P_b - \epsilon$ Dissipation Rate: $\frac{\partial \epsilon}{\partial t} + \frac{\partial}{\partial x_i} (\epsilon u_i) = \frac{\partial}{\partial x_j} \left[\left(\nu + \frac{\nu_t}{\sigma_\epsilon} \right) \frac{\partial \epsilon}{\partial x_j} \right] + C_{1\epsilon} \frac{\epsilon}{k} (P_k + C_{3\epsilon} P_b) - C_{2\epsilon} \frac{\epsilon^2}{k}$ Closure Constants: $C_\mu = 0.09, \sigma_k = 1.0, C_{1\epsilon} = 1.44, C_{2\epsilon} = 1.92, \sigma_\epsilon = 1.3$
RNG $k - \epsilon$	Kinematic Eddy Viscosity: $\nu_T = \frac{a_1 k}{\max(a_1 \omega, S F_2)}$ Turbulent Kinetic Energy: $\frac{\partial k}{\partial t} + U_i \frac{\partial k}{\partial x_i} = \frac{\partial}{\partial x_j} \left[\left(\mu + \frac{\mu_t}{\sigma_k} \right) \frac{\partial k}{\partial x_j} \right] + P_k + P_b - \epsilon$ Specific Dissipation Rate: $\frac{\partial}{\partial t} (\epsilon) + \frac{\partial}{\partial x_i} (\epsilon u_i) = \frac{\partial}{\partial x_j} \left[\left(\nu + \frac{\nu_t}{\sigma_\epsilon} \right) \frac{\partial \epsilon}{\partial x_j} \right] + C_{1\epsilon} \frac{\epsilon}{k} P_k - C_{2\epsilon}^* \frac{\epsilon^2}{k}$ Closure Constants and Auxiliary Relations: $C_\mu = 0.0845, \sigma_k = 0.7194, \sigma_\epsilon = 0.7194$ $C_{\epsilon 1} = 1.42, C_{\epsilon 2} = 1.68, \eta_0 = 4.38, \beta = 0.012$ $C_{2\epsilon}^* = C_{2\epsilon} + \frac{C_\mu \eta^3 (1 - \eta / \eta_0)}{1 + \beta \eta^3}, \eta = S_{ij} k / \epsilon$

Table A.2: Popular two-equation $k - \omega$ turbulence models.

Wilcox $k - \omega$	Kinematic Eddy Viscosity: $\nu_T = \frac{k}{\omega}$ Turbulent Kinetic Energy: $\frac{\partial k}{\partial t} + U_j \frac{\partial k}{\partial x_j} = P_k - \beta^* k \omega + \frac{\partial}{\partial x_j} \left[(\nu + \sigma^* \nu_T) \frac{\partial k}{\partial x_j} \right]$ Specific Dissipation Rate: $\frac{\partial \omega}{\partial t} + U_j \frac{\partial \omega}{\partial x_j} = \alpha \frac{\omega}{k} \tau_{ij} \frac{\partial U_i}{\partial x_j} - \beta \omega^2 + \frac{\partial}{\partial x_j} \left[(\nu + \sigma \nu_T) \frac{\partial \omega}{\partial x_j} \right]$ Closure Constants and Auxilary Relations: $\alpha = \frac{5}{9}, \beta = \frac{3}{40}, \beta^* = \frac{9}{100}, \sigma = \frac{1}{2}, \sigma^* = \frac{1}{2}, \varepsilon = \beta^* \omega k$
Wilcox modified $k - \omega$	Kinematic Eddy Viscosity: $\nu_T = \frac{k}{\omega}$ Turbulent Kinetic Energy: $\frac{\partial k}{\partial t} + U_j \frac{\partial k}{\partial x_j} = P_k - \beta^* k \omega + \frac{\partial}{\partial x_j} \left[(\nu + \sigma^* \nu_T) \frac{\partial k}{\partial x_j} \right]$ Specific Dissipation Rate: $\frac{\partial \omega}{\partial t} + U_j \frac{\partial \omega}{\partial x_j} = \alpha \frac{\omega}{k} \tau_{ij} \frac{\partial U_i}{\partial x_j} - \beta \omega^2 + \frac{\partial}{\partial x_j} \left[(\nu + \sigma \nu_T) \frac{\partial \omega}{\partial x_j} \right]$ Closure Constants and Auxilary Relations: $\alpha = \frac{13}{25}, \beta = \beta_0 f_\beta, \beta^* = \beta_0^* f_{\beta^*}, \sigma = \frac{1}{2}, \sigma^* = \frac{1}{2}, \beta_0 = \frac{9}{125}$ $f_\beta = \frac{1+70\chi_\omega}{1+80\chi_\omega}, \chi_\omega = \left \frac{\Omega_{ij}\Omega_{jk}S_{ki}}{(\beta_0^*\omega)^3} \right , \beta_0^* = \frac{9}{100}$ $f_{\beta^*} = \begin{cases} 1, & \chi_k \leq 0 \\ \frac{1+680\chi_k^2}{1+80\chi_k^2}, & \chi_k > 0 \end{cases}, \chi_k \equiv \frac{1}{\omega^3} \frac{\partial k}{\partial x_j} \frac{\partial \omega}{\partial x_j}, \varepsilon = \beta^* \omega k, l = \frac{k^{\frac{1}{2}}}{\omega}$

A.2 Reactor volume variation

For the CFD computations in Chapter 6 the volume of the reactor was considered constant. Nevertheless, a certain variation of the reactor volume occurs as the liquid phase density changes with time. Measurements of the height or volume of the reactor during the experiment are not available. Therefore, the volume estimation have been done based on the concentration, temperature and density values of the liquid phase.

The assumption for the calculation of the reactor volume include: (i) water is not present in the solid phase (ii) the concentration of the potassium alum in the liquid phase is considered homogeneous in the reactor.

The density of the liquid phase was calculated using the measured concentration and temperature values. The dependency of concentration, temperature and density of the potassium alum were obtained from Mullin et al. (1965) and interpolated in MATLAB using the *fit poly23* function, see Fig. A.1.

Properties of the liquid and solid phases at the initial time and final time are given in Table A.3. The variation of the reactor volume with time is given in Fig. A.2.

Note that the volume variation between the initial and final time is only around 0.1%.

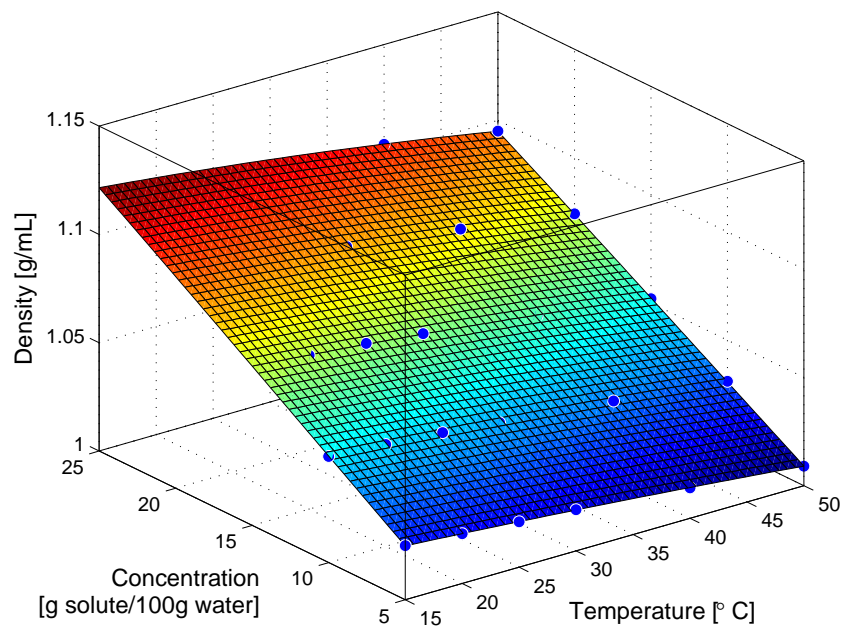


Figure A.1: Measurements from Mullin et al. (1965) for concentration, temperature and density dependency. The blue dots represent the experimental values.

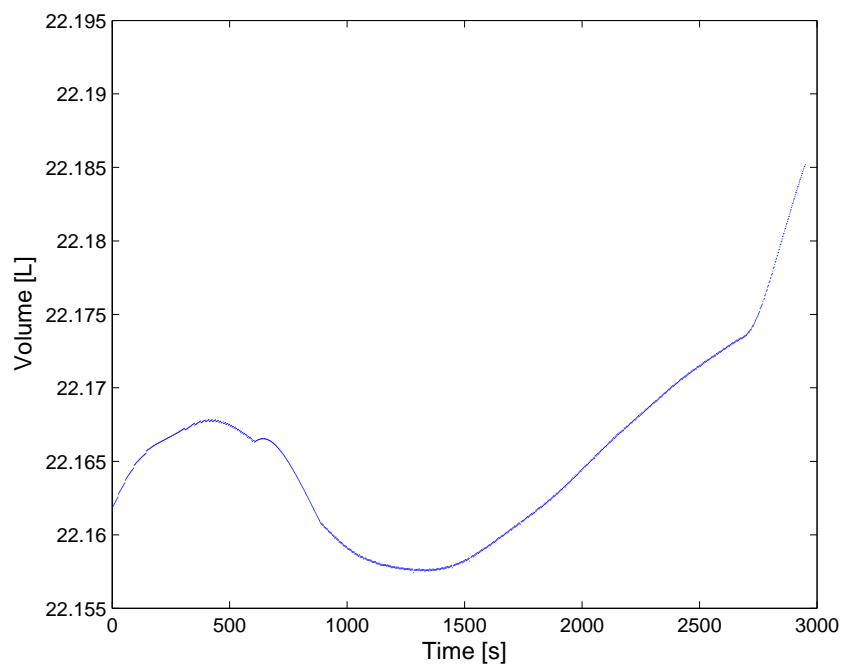


Figure A.2: Volume variation within the reactor.

Table A.3: Properties of the liquid and solid phases at initial and final time of the crystallization batch.

Properties	Initial time	Final time
temperature [°C]	33.96	28.49
saturation concentration [g/g _{water}]	0.1877	0.1549
concentration [g /g _{water}]	0.19629	0.1547
mass of water in the liquid phase [g]	20×10^3	20×10^3
mass of $KAL(SO_4)_2$ in the liquid phase [g]	3.93×10^3	3.09×10^3
mass of $KAL(SO_4)_2$ in the solid phase [g]	0.17×10^3	1.01×10^3
density of the liquid phase [g/L]	1084	1068
density of the solid phase ($KAL(SO_4)_2$) [g/L]	1750	1750
reactor work volume [L]	22.1621	22.1851

References

- B. Ashraf Ali, M. Börner, M. Peglow, G. Janiga, A. Seidel-Morgenstern, and D. Thévenin. Coupled Computational Fluid Dynamics-Discrete Element Method Simulations of a Pilot-Scale Batch Crystallizer. *Crystal growth and design*, 15(1): 145–155, 2015.
- T. Allen. *Particle Size Measurement*. Particle Technology Series, Springer, 5th Edition, 1997.
- ANSYS Inc. *ANSYS FLUENT User’s Guide*. ANSYS Inc, Canonsburg, PA, 2011.
- C. W. Bakker, C. J. Meyer, and D. A. Deglon. Numerical modelling of non-newtonian slurry in a mechanical flotation cell. *Minerals Engineering*, 22(11):944–950, 2009.
- J. Bałdyga and W. Orciuch. Barium sulphate precipitation in a pipe: an experimental study and CFD modelling. *Chemical Engineering Science*, 56:2435–2444, 2001.
- G. K. Batchelor and A. A. Townsend. Decay of turbulence in the final period. *Proceedings of Royal Society*, 194A:527–543, 1948.
- D. Bertsimas and T. R. Weismantel. *Optimization over integers*. Dynamic Ideas, Belmont, Massachusetts, 2005.
- F. Bezzo, S. Macchietto, and C. C. Pantelides. Computational issues in hybrid multizonal/computational fluid dynamics models. *AIChE Journal*, 51(4):1169–1177, 2005.
- Marcel Bottema. Turbulence closure model constants and the problem of inactive atmospheric turbulence. *Journal of Wind Engineering & Industrial Aerodynamics*, 67 and 68:897–908, 1997.
- Y.S. Chen and S.W. Kim. Computation of turbulent flows using an extended $k - \epsilon$ turbulence closure model. *Report NASA CR-179204*, 1987.
- Y. D. Choi, H. Lacovides, and B. E. Launder. Numerical computation of turbulent flow in a square-sectioned 180 deg bend. *Journal of Fluids Engineering*, 111:59–68, 1989.

-
- P. Y. Chou. On the velocity correlation and the solution of the equations of turbulent fluctuation. *Quarterly of Applied Mathematics*, 3:38, 1945.
- M. Darbandi, A. Setayeshgar, S. Vakili, and G. E. Schneider. Modification of standard k-epsilon turbulence model for multi-element airfoil application using optimization technique. *AIAA Paper 2006-2829, the 24th AIAA Applied Aerodynamics Conference, San Francisco, California, June 5-8, 2006*, 2006.
- L. G. M. de Souza, G. Janiga, V. John, and D. Thévenin. Reconstruction of a distribution from a finite number of moments with an adaptive spline-based algorithm. *Chemical Engineering Science*, 65:2741–2750, 2010.
- K. Deb and R. B. Agarwal. Simulated binary crossover for continuous search space. *Complex Systems*, 9:115–148, 1995.
- K. Deb, A. Pratap, S. Agarwal, and T. Meyarivan. A fast and elitist multiobjective genetic algorithm: NSGA-II. *IEEE Transactions on Evolutionary Computation*, 6(2):182–197, 2002.
- D. A. Deglon and C. J. Meyer. CFD modeling of stirred tanks: numerical considerations. *Minerals Engineering*, 19:1059–1068, 2006.
- A. Delafosse, M.-L. Collignon, S. Calvo, F. Delvigne, M. Crine, P. Thonart, and D. Toye. CFD-based compartment model for description of mixing in bioreactors. *Chemical Engineering Science*, 106:76–85, 2014.
- R.B. Diemer and J.H. Olson. A moment methodology for coagulation and breakage problems: Part 2-moment models and distribution reconstruction. *Chemical Engineering Science*, 57:2211–2228, 2002.
- P. G. Duynkerke. Application of the $E-\epsilon$ model to the neutral and stable atmospheric boundary layer. *Journal of the Atmospheric Sciences*, 45:865–880, 1988.
- M. M. M. El Telbany and A. J. Reynolds. Turbulence in plane channel flows. *Journal of Fluid Mechanics*, 111:283–318, 1981.
- L. Elliott, D. Ingham, A. Kyne, N. Mera, M. Pourkashanian, and C. Wilson. Genetic algorithms for optimisation of chemical kinetics reaction mechanisms. *Progress in Energy and Combustion Science*, 30:297–328, 2004.
- L. Elliott, D.B. Ingham, A.G. Kyne, N.S. Mera, M. Pourkashanian, and C.W. Wilson. Reaction mechanism reduction and optimization using genetic algorithms. *Industrial and Engineering Chemistry Research*, 44:658–667, 2005.

-
- M.P. Elsner, D.F. Fernández Menéndez, E.A. Muslera, and A. Seidel-Morgenstern. Experimental study and simplified mathematical description of preferential crystallization. *Chirality*, 17:183–195, 2005.
- R. Fan, D.L. Marchisio, and R.O. Fox. Application of the direct quadrature method of moments to polydisperse gas-solid fluidized beds. *Powder Technology*, 139:7–20, 2004.
- S. K. Friedlander. Mass and heat transfer to single spheres and cylinders at low reynolds numbers. *AIChE J.*, 3(1):43–48, 1957.
- N. Froessling. The evaporation of falling drops (in German). *Gerlands Beiträge zur Geophysik*, 52:170–216, 1938.
- J. Fröhlich. *Large Eddy Simulation turbulenter Strömungen*. Teubner-Verlag, Wiesbaden, 2006.
- F. Geldard and J.H. Seinfeld. Simulation of multicomponent aerosol dynamics. *Journal of Colloid and Interface Science*, 78 (2):485–501, 1980.
- D.T. Gillespie. The stochastic coalescence model for cloud droplet growth. *J. Atmos. Sci.*, 29:1496–1510, 1972.
- J. H. Goebbert, M. Gauding, M. Gampert, P. Schaefer, N. Peters, and L. Wang. A new view on geometry and conditional statistics in turbulence. In S. Fu, W. Haase, S.-H. Peng, and D. Schwamborn, editors, *Inside: Innovatives supercomputing in Deutschland, Vol(9) No.1*. 2011.
- R. De Goede and G. M. Van Rosmalen. Modelling of crystal growth kinetics: a simple but illustrative approach. *Journal of Crystal Growth*, 104:392–398, 1990.
- D. E. Goldberg, editor. *Genetic Algorithms in Search, Optimization and Machine learning*. Addison-Wesley, 1989.
- G. H. Golub and J. H. Welsch. Calculation of Gauss quadrature rules. *Mathematics of Computation*, 23:221–230, 1969.
- R. G. Gordon. Error bounds in equilibrium statistical mechanics. *Journal of Mathematical Physics*, 9:655–663, 1968.
- K. Hanjalić. Two-dimensional asymmetric turbulent flow in ducts. *Ph.D Thesis*, University of London, 1970.
- F. H. Harlow and P. I. Nakayama. Transport of turbulence-energy decay rate. *Los Alamos National Laboratory Report, LA-3854*, 1968.

-
- V. G. Harris, A.A. Graham, and S. Corrsin. Further experiments in nearly homogeneous turbulent shear flow. *Journal of Fluid Mechanics*, 81:657–687, 1977.
- A. Hasseine, A.-H. Meniai, M. Korichi, M. B. Lehocine, and H.-J. Bart. A genetic algorithm based approach to coalescence parameters: Estimation in liquid-liquid extraction columns. *Chemical Engineering and Technology*, 29(12):1416–1423, 2006.
- T. Hayashi, Y. Li, and Y. Hara. Wind tunnel tests on a different phase three-stage Savonius rotor. *JSME International Journal, Series B: Fluids and Thermal Engineering*, 48(1):9–16, 2005.
- R.A.W.M. Henkes and F.F. van der Flugt. Natural convection flow in a square cavity calculated with low-Reynolds-number turbulence models. *International Journal of Heat and Mass Transfer*, 34:1543–1557, 1991.
- M. Henneberg. Strömungssimulation eines Batch-Kristallisator, 2014. Studienarbeit, LSS-501/11, Magdeburg.
- R. Hilbert, G. Janiga, R. Baron, and D. Thévenin. Multi-objective shape optimization of a heat exchanger using parallel genetic algorithms. *International Journal of Heat and Mass Transfer*, 49:2567–2577, 2006.
- Gilbert H. Hoffman. Improved form of the low Reynolds number $k - \epsilon$ turbulence model. *Physics of Fluids*, 18:309–313, 1975.
- M. J. Hounslow, R. L. Ryall, and V. R. Marschall. A discretized population balance for nucleation, growth and aggregation. *AIChE Journal*, 34:1821–1832, 1988.
- M. Ishii and T. Hibiki. *Thermo-Fluid Dynamics of Two-Phase Flow*. Springer, New York, USA, second edition edition, 2006.
- G. Janiga. Flow Optimization using Computational Fluid Dynamics, 2011. Habilitation thesis, University of Magdeburg, Germany.
- H. Jiang, G. Zhong, H. Ning, F. Ouyang, and H. Weng. Lumping kinetic model of heavy oil catalytic cracking for MIP technology. *Acta Petrolei Sinica*, 26(6): 901–909, 2010.
- V. John, I. Angelov, A. A. Öncül, and D. Thévenin. Techniques for the reconstruction of a distribution from a finite number of its moments. *Chemical Engineering Science*, 62:2890–2904, 2007.

-
- W.P. Jones and B.E. Launder. The prediction of laminarization with a two equation model of turbulence. *International Journal of Heat and Mass Transfer*, 15:301–314, 1972.
- M. Joshi. Partial oxidation of ethane (real data). In: *Statistical Analysis of Models and Parameters in Chemical and Biochemical Reaction Network*. Ph.D. thesis, University of Magdeburg, ISBN, 978-3-8325-1670-3, 2007.
- M. Kaspereit, S. Swernath, and A. Kienle. Evaluation of competing process concepts for the production of pure enantiomers. *Organic Process Research & Development*, 16:353–363, 2012.
- Y. Kawajiri and L. T. Biegler. A nonlinear programming superstructure for optimal dynamic operations of simulated moving bed processes. *Industrial & Engineering Chemistry Research*, 45(25):8503–8513, 2006.
- F. Klose, M. Joshi, C. Hamel, and A. Seidel-Morgenstern. Selective oxidation of ethane over a VOx/Al₂O₃ catalyst - investigation of the reaction network. *Applied Catalysis A*, 260:101–110, 2004.
- A. Konak, D. W. Coit, and A. E. Smith. Multi-objective optimization using genetic algorithms: A tutorial. *Reliability Engineering & System Safety*, 91(9):992–1007, 2006.
- V. Kulikov. *A generalized framework for multi-scale simulation of complex crystallization processes*. PhD thesis, Technische Hochschule Aachen, Aachen, Germany, 2010.
- B. E. Launder and D. B. Spalding. The numerical computation of turbulent flows. *Computer Methods in Applied Mechanics and Engineering*, 3:269–289, 1974.
- B.E. Launder and B.I. Sharma. Application of the energy-dissipation model of turbulence to the calculation of flow near a spinning disc. *Letters in Heat and Mass Transfer*, 1:131–138, 1974.
- B.E. Launder and D.B. Spalding. *Mathematical Models of Turbulence*. Academic Press: London, New York, 1972.
- P. A. Libby. *Introduction to Turbulence*. Taylor and Francis, first edition, 1996.
- M. Liiri, Y. Enqvist, J. Kallas, and J. Aittamaa. CFD modelling of single crystal growth of potassium dihydrogen phosphate (KDP) from binary water solution at 30°C. *Journal of Crystal Growth*, 19:413–423, 2006.

-
- H. Lorenz, A. Perlberg, D. Sapoundjiev, M.P. Elsner, and A. Seidel-Morgenstern. Crystallization of enantiomers. *Chemical Engineering and Processing*, 45:863–873, 2006.
- V. Lotfi, T. J. Stewart, and S. Zionts. An aspiration-level interactive model for multiple criteria decision making. *Computers and Operations Research*, 19(7): 671–681, 1992.
- D. L. Marchisio and R. O. Fox. *Computation Models for Polydisperse Particulate and Multiphase Systems*. Cambridge University Press, New York, 2013.
- D.L. Marchisio and R.O. Fox. Solution of population balance equations using the direct quadrature method of moments. *Journal of Aerosol Science*, 36 (1):43–73, 2005.
- D.L. Marchisio, A.A. Barresi, and M. Garbero. Nucleation, growth and agglomeration in barium sulfate turbulent precipitation. *AIChE Journal*, 48:2039–2050, 2002.
- G. B. Marin and G. S. Yablonsky. *Kinetics of Chemical Reactions*. Weinheim: Wiley-VHC Verlag, 2011.
- M. A. Marvast, M. Sohrabi, and H. Ganji. Kinetic modeling of the Fischer-Tropsch reactions and modeling steady state heterogeneous reactor. *World Academy of Science, Engineering & Technology*, 74:430–437, 2011.
- R. McGraw. Description of aerosol dynamics by the quadrature method of moments. *Aerosol Science and Technology*, 27 (2):255–265, 1997.
- Z. Michalewicz. *Genetic algorithms + data structures = Evolution programs*. Berlin, New York: Springer-Verlag, 1996.
- D. Modaress, J. Wuerer, and S. Elgobashi. An experimental study of a turbulent round two-phase jet. *American Institute of Aeronautics and Astronautics/American Society of Mechanical Engineers 3rd Joint Thermophysics, Fluids, Plasma and Heat Transfer Conference, Saint Louis, June, 1982*, 1982.
- M. H. A. Mohamed. *Design optimization of Savonius and wells turbines*. PhD thesis, Otto-von-Guericke University, Magdeburg, Germany, 2011.
- M.S. Mohamed and J.C. Larue. The decay power law in grid generated turbulence. *Journal of Fluid Mechanics*, 219:195–214, 1990.
- S. T. F. C. Mortier, T. D. Beer, K. V. Gernaey, and I. Nopens. Comparison of techniques for reconstruction of a distribution from moments in the context of

-
- a pharmaceutical drying process. *Computers and Chemical Engineering*, 65:1–8, 2014.
- J. W. Mullin. *Crystallization*. Butterworth-Heinemann, Oxford, fourth edition edition, 2001.
- J. W. Mullin, J. Garside, and R. Unahabhokha. Diffusivities of ammonium and potassium alums in aqueous solutions. *Journal of Applied Chemistry*, 15:502–505, 1965.
- A. Nakayama. Characteristics of the flow around conventional and supercritical airfoils. *Journal of Fluid Mechanics*, 160:155–179, 1985.
- V. W. Nee and L. S. G. Kovasznyai. The calculation of the incompressible turbulent boundary layer by a simple theory. *Physics of Fluids*, 12:473–484, 1969.
- A. A. Öncül, G. Janiga, and D. Thévenin. Comparison of various micromixing approaches for Computational Fluid Dynamics simulation of barium sulfate precipitation in tubular reactors. *Industrial & Engineering Chemistry Research*, 48:999–1007, 2009.
- B. Ozdemir and S. Gultekin. Model discrimination in chemical kinetics. *The Open Catalysis Journal*, 2:1–6, 2009.
- T. J. Park, S. Bhargava, and G. G. Chase. Fitting of kinetic parameters of NO reduction by CO in fibrous media using a genetic algorithm. *Computers and Chemical Engineering*, 34:485–490, 2010.
- W. Polifke, W. Geng, and K. Döbbeling. A hybrid genetic algorithm for the estimation of parameters in detailed kinetic models. *Combustion and Flame*, 113:119–135, 1998.
- Stephen B. Pope. *Turbulent Flows*. Cambridge University Press, Cambridge, first edition, 2000.
- S. Qamar, M.P. Elsner, I.A. Angelov, G. Warnecke, and A. Seidel-Morgenstern. A comparative study of high resolution schemes for solving population balances in crystallization. *Computers & Chemical Engineering*, 30:1119–1131, 2006.
- Weiqi Qian and Jinshi Cai. Parameter estimation of engineering turbulence model. *Chinese Journal of Mechanical Engineering*, 17(4):302–309, 2001.
- D. Ramkrishna. *Population Balances*. Academic Press, San Diego (CA), 2000.

-
- Rangaiah and G. Pandu. *Multi-Objective Optimization : Techniques and Applications in Chemical Engineering*. Singapore, World Scientific, 2008.
- G. P. Rangaiah and A. Bonilla-Petriciolet, editors. *Multi-Objective Optimization in Chemical Engineering: Development and Application*. John Wiley and Sons, Chichester, 2013.
- W. E. Ranz and W. R. Marshall. Evaporation from drops part I). *Chemical Engineering Progress*, 48:141–146, 1952.
- C. H. Rapp. Experimentelle Studie der turbulenten Strömung über periodische Hügel. *Technische Universität München, Fachgebiet Hydromechanik, Mitteilung*, 75, 2009.
- W. C. Reynolds. Fundamentals of turbulence for turbulence modeling and simulation. *Lecture Notes of Von Karman Institute, AGARD Report*, 755, 1987.
- B. Ruck and B. Makiola. Flow separation over the step with inclined walls. *Near-wall turbulent flows (R.M.C. So, C.G. Speziale, B.E. Launder, eds.)*, Elsevier, pages 999–1008, 1993.
- T. Sarkar, P. G. Sayer, and S. M. Fraser. Flow simulation past axisymmetric bodies using four different turbulence models. *Applied Mathematical Modelling*, 21 (12): 783–792, 1997.
- L. Schiller and Z. Naumann. A drag coefficient correlation. *Z. Ver. Deutsch. Ing.*, pages 77–318, 1935.
- H.C. Schwarzer, F. Schwertfirm, M. Manhart, H.-J. Schmidt, and W. Peukert. Predictive simulation of nanoparticle precipitation based on the population balance equation. *Chemical Engineering Science*, 61:167–181, 2006.
- M. Von Schwerin, O. Deutschmann, and V. Schulz. Process optimization of reactive systems by partially reduced SQP methods. *Computers & Chemical Engineering*, 24(1):89–97, 2000.
- P. Sean and J.-B. Yang. *Multiple criteria decision support in engineering design*. London, Springer, 1998.
- A. Seidel-Morgenstern. *Membrane Reactors: Distributing Reactants to Improve Selectivity and Yield*. Weinheim: Wiley-VCH, 2010.
- B.H. Shah, D. Ramkrishna, and J.D. Borwanker. Simulation of particulate systems using the concept of the interval of quiescence. *AIChE J.*, 23:897–904, 1977.

-
- T. H. Shih, W. W. Liou, A. Shabbir, Z. Yang, and J. Zhu. A new k-epsilon eddy viscosity model for high reynolds number turbulent flows: Model development and validation. *Computers & Fluids*, 24 (3):227–238, 1995.
- P. Slater. Joint Hilbert-Schmidt determinantal moments of product form for two-rebit and two-qubit and higher-dimensional quantum systems. *Quantum Physics*, arXiv:1104.0217, 2011.
- A. Soltanzadeh and G. Dumont. Estimation of higher moments of a transfer function using input and output data system identification. *16th IFAC Symposium on System Identification*, 16, 2012.
- P. Spalart. Reflections on RANS modelling. In S. Fu, W. Haase, S.-H. Peng, and D. Schwamborn, editors, *Progress in Hybrid RANS-LES Modeling, NNFM 111*. Springer: Berlin, Heidelberg, 2010.
- P. R. Spalart. Strategies for turbulence modelling and simulation. *International Journal of Heat and Fluid Flow*, 21:252–263, 2000.
- P. R. Spalart. RANS modelling into a second century. *International Journal of Computational Fluid Dynamics*, 23(4):291–293, 2009.
- W. E. Stewart, M. Caracotsios, and J. P. Sorensen. Parameter estimation from multiresponse data. *AIChE Journal*, 38(5):641–650, 1992.
- M. Strumendo and H. Arastoopour. Solution of PBE by MOM in finite size domains. *Chemical Engineering Science*, 63:2624–2640, 2008.
- G. Tabor, A. D. Gosman, and R. I. Issa. Numerical simulation of the flow in a mixing vessel stirred by a Rushton turbine. *Institution of Chemical Engineers. ICHEM symposium series*, Fluid Mixing 5:25–34, 1996.
- S. Tavoularis and S. Corrsin. Experiments in nearly turbulent shear flows with a uniform mean temperature gradient. *Journal of Fluid Mechanics*, 104:311–347, 1981.
- E. Temmel, M. Eicke, H. Lorenz, and A. Seidel-Morgenstern. A short-cut-method for the quantification of crystallization kinetics - part 2: Experimental application. *Crystal Growth & Design*, In press, 2016.
- K. Tesch, M. A. Atherton, T. G. Karayiannis, M.W. Collins, and P. Edwards. Determining heat transfer coefficients using evolutionary algorithms. *Engineering Optimization*, 41(9):855–870, 2009.

-
- F. Thein. On the efficiency and condition of the core routine of the quadrature methods of moments (QMOM). *Diploma Thesis*, Otto-von-Guericke University, 2012.
- D. Thévenin and G. Janiga, editors. *Optimization and Computational Fluid Dynamics*. Springer: Berlin, Heidelberg, 2008.
- J. Warnatz, U. Maas, and R. W. Dibble. *Combustion*. Berlin, Heidelberg: Springer-Verlag, 2006.
- H. Wei, W. Zhou, and J. Garside. Computational fluid dynamics modeling of the precipitation process in a semibatch crystallizer. *Industrial and Engineering Chemistry Research*, 40:5255–5261, 2001.
- J. C. Wheeler. Modified moments and gaussian quadratures. *Rocky Mountain Journal of Mathematics*, 4:287–296, 1974.
- J. Xu, T. Rickert, and U. Hoffmann. Model discrimination and parameter estimation in the kinetic study of methanol synthesis. *Chemical Engineering & Technology*, 11:375–383, 1988.
- H. Yeomans and I. E. Grossmann. A systematic modeling framework of superstructure optimization in process synthesis. *Computers and Chemical Engineering*, 23(6):709–731, 1999.

Luís Guilherme Medeiros de Souza, M.Sc.

Personal Information

Date of Birth: 10/11/1982
Place of Birth: Joaçaba, Brazil
Nationality: Brazilian

Education

11/2008-currently Ph.D. candidate at University of Magdeburg (OvGU)/International Max Planck Research School (IMPRS), Magdeburg, Germany

2006-2008 Master of Science in Chemical and Process Engineering at University of Magdeburg (OvGU), Magdeburg, Germany

2000-2005 Degree in Chemical Engineering at Federal University of Santa Catarina (UFSC), Florianópolis, Brazil

Research/Work Experience

01/2014-currently Associate researcher at the DFG-project SFB/TR63 "Integrated Chemical Processes in Liquid Multiphase Systems" (InPROMPT)
WG: Prof. Dr.-Ing. Dominique Thévenin
Project: B8 - Dispersion and coalescence in stirred micellar three-phase systems

07/2013-currently Associate researcher at the DFG-project "Dynamic simulation of cross-linked solid process" (SPP 1679)
WG: Priv.-Doz. Dr.-Ing. Gábor Janiga
Project: C3 - Model-based analysis and synthesis of a novel process network for continuous separation of enantiomers

11/2008-currently Research fellow at the Laboratory of Fluid Dynamics and Technical Flow, University of Magdeburg, Germany
Supervisors: Priv.-Doz. Dr.-Ing. Gábor Janiga and Prof. Dr.-Ing. Dominique Thévenin
Topic: Model optimization and techniques for the simulation of multiphase chemical reactors

03/2008-09/2008 Master Thesis at the Laboratory of Fluid Dynamics and Technical Flow, University of Magdeburg, Germany
Supervisors: Priv.-Doz. Dr.-Ing. Gábor Janiga and Prof. Dr.-Ing. Dominique Thévenin
Topic: Reconstruction of a distribution from a finite number of its moments

10/2006-06/2007 Research assistant at the Group of Physical and Chemical Foundations of Process Engineering, Max Planck Institute for Dynamics of Complex Technical Systems, Germany
Supervisor: Dr.-Ing. Felix Czaplá
Topic: Parameter estimation in crystallization

01/2005-07/2005 Internship student at the pulp and paper mill Celulose Irani, Vargem Bonita, Santa Catarina, Brazil.
Supervisor: Leandro A. Farina and Prof. Dr. Antônio A. U. de Souza
Topic: Environmental control of pollutants in a pulp and paper mill

05/2003-12/2003 Undergraduate research at the Department of Chemistry, Federal University of Santa Catarina, Brazil
Supervisor: Dr. Julieta Barbosa Monteiro
Topic: Kinetic of immobilized enzymes

Teaching Experience

2009-2013 Assistant in the lecture "Numerische Strömungsmechanik (CFD)", Institute of Fluid Dynamics and Thermodynamics, OVGU, Magdeburg, Germany

Languages

Portuguese (Native), English (Fluent), German (Advanced), Spanish (Advanced)

Conferences/Workshops participation

09/2013 3rd summer school of the IMPRS Magdeburg, Multiscale Modelling and Simulation, Magdeburg, Germany
06/2012 9th International ERCOFTAC Symposium on Engineering Turbulence Modeling and Measurements (ETMM9), Thessaloniki, Greece. (Poster)
11/2011 Max Planck Institute for Dynamics of Complex Technical Systems, Magdeburg, Germany. (Talk)
09/2011 2nd summer school of the IMPRS Magdeburg, Large Scale Networks in Engineering and Life Science, Magdeburg, Germany
06/2011 CFD for Dispersed Multi-Phase Flows, Stockholm, Sweden
10/2010 EnginSoft International Conference, Brescia, Italy. (Talk)
11/2009 ERCOFTAC Introductory Course to Design Optimization, Berlin, Germany

Scholarships/Honors

11/2008-10/2012 International Max Planck Research School (IMPR) Scholarship
03/2006 Second place in the national contest of the oil company Petrobras Transporte S.A. (Transpetro), Brazil

List of Publications

L. Medeiros de Souza, G. Janiga and D. Thévenin. Multi-objective optimisation of the model parameters for the realizable k- ϵ turbulence model. *Progress in Computational Fluid Dynamics*, in press, 2015.

K. Kerst, L. Medeiros de Souza, A. Bartz, A. Seidel-Morgenstern and G. Janiga. *CFD-DEM simulation of a fluidized bed crystallization reactor*. In: *Computer Aided Chemical Engineering*, (K.V. Gernaey, J.K. Huusom and R. Gani, Eds.), Elsevier, 263 - 268, 2015.

K. Kerst, L. Medeiros de Souza, A. Seidel-Morgenstern and G. Janiga. CFD-DEM simulation of a fluidized bed crystallization reactor. In: *12th PSE and 25th ESCAPE Joint Event 40*, Copenhagen, Denmark, 2015.

L.G.M. de Souza, H. Haida, G. Janiga, A. Seidel-Morgenstern and D. Thévenin. Model Optimization and Parameter Estimation for Chemical Reactions using Global Model Structure. *Computers and Chemical Engineering* 58, 269 - 277, 2013.

L.G.M. de Souza, G. Janiga and D. Thévenin. Multi-objective Parameter Optimization of the k- ϵ Turbulence Model. In: *Proceedings of the 9th International ERCOFTAC Symposium on Engineering Turbulence Modeling and Measurements (ETMM9)*, Thessaloniki, Greece, June 6th - 8th, 2012.

L.G.M. de Souza, G. Janiga, V. John and D. Thévenin. Reconstruction of a distribution from a finite number of moments with an adaptive spline-based algorithm. *Chemical Engineering Science* 65, 2741 - 2750, 2010.